ADHESION EVALUATION AND ASSEMBLY PROCESS DEVELOPMENT FOR PRINTED SILVER INK ON FLEXIBLE SUBSTRATES

A Dissertation
Presented to
The Academic Faculty

by

Christine Louise Taylor

In Partial Fulfillment
of the Requirements for the Degree
Doctor of Philosophy in the
George W. Woodruff School of Mechanical Engineering

Georgia Institute of Technology
December of 2019

ADHESION EVALUATION AND ASSEMBLY PROCESS DEVELOPMENT FOR PRINTED SILVER INK ON FLEXIBLE SUBSTRATES

Approved by:

Dr. Suresh K. Sitaraman, Advisor
School of Mechanical Engineering
Georgia Institute of Technology

Dr. Chuck Zhang
School of Industrial and Systems Engineering
Georgia Institute of Technology

Dr. Tequila A. L. Harris
School of Mechanical Engineering
Georgia Institute of Technology

Dr. Pulugurtha Markondeya Raj
School of Electrical Engineering
Georgia Institute of Technology

Dr. Yan Wang
School of Mechanical Engineering
Georgia Institute of Technology

Date Approved: [11 08, 2019]

To my family

To my friends

To those who love to learn

ACKNOWLEDGEMENTS

Though out my time at Georgia Tech, my deepest appreciation goes to the support from family (Reiko Taylor, Ed Taylor, Andrew Taylor, Shila Gilbert, Joe Gilbert, Seph Gilbert, Naoko Kinoshita, Russel Peak, Huki Peak, Joy Peak-Haskell, Jonathan Peak, Joe Peak, Shinichi Kinoshita, Michiko Kinoshita, Masao Kinoshita, Lihong Kinoshita, Sharlene Kinoshita).

To Professor Suresh K. Sitaraman, thank you for all your patience and support as an advisor throughout the years. Your mentorship is deeply appreciated. To Dr. Harris, thank you for your frank discussions about the Ph.D. process and health through the FACES program and for always checking to see that I finished the Ph.D.. To Dr. Raj thank you for your help in the lab and always having an encouraging outlook. To Dr. Chuck Zhang, thank you for initial introduction to electronic printing and to your group for support, which is knowledgeable and kind. To Dr. Yan Wang, thank you for stepping in at the last moment on my committee and all your feedback for the final presentation. To Dr. Charles Ume, he'll be remembered for the change he brought to Gatech's campus, but his heart for the students and follow-up always shined through for our conversations in the hallway between the lab and his office. To all my committee members: Dr. Tequila A. L. Harris, Dr. Yan Wang, Dr. Chuck Zhang, Dr. Pulugurtha Markondeya Raj, and Dr. Charles Ume, thank you for serving on my committee.

To all the members of CASPaR lab (Sathya Raghavan, Raphael Okereke, Wei Chen, Xi Liu, Scott McCann, Justin Chow, David Samet, Isaac Bower, Paula Xian, Guru Raveendran, Yaqin Song, Ye Tian, Abhishek Kwatra, Nick Ginga, Greg Ostrowici, Ju Xu,

Trilochan Rambhatla, Casey Woodrum, Chong, Rui Chen, Yi Zhou, Ben Stewart, Jamie Ahmad) thank you for the encouragement, daily laughs and interesting discussions. To Dr. Venessa Smet, thank you for your kind heart and making time for helping in the assembly lab as well as the conversations from teaching ideas to brainstorming packaging to harrowing tales of rabbit rescues.

To the Packaging Research Center (PRC), assembly lab, thank you for the support in the work (Chris White, Kayshap Mohen, Jason Bishop, Lila and Karen May). To the IEN staff (Eric Woods, Todd Walters, Walter Henderson, Hang Chen, Gary Spinner, Charlie Suh, Mikel Thomas, Devin Brown, John Pham, Jason Hennington, Braxton, Kristin Turgeon, & Amy Bonecutter), you all are so knowledgeable and serve the Gatech community so much every day. To Athena Group (Tony He, Aline Eid, Ryan Bahr & Bijan Tehrani), thank you for tips and help with printing the flexible electronics.

To Dr. Sitaraman's administrators (Melisa Raines, Kyana Giddens, and Ann Lamb), thank you for your support for the logistics of getting research accomplished and making sure all to dot the *i's* and cross the *t's*. To the ME Staff (Kyle French, Glenda Johnson, Marlena Frank, Danny Hardawar, Anthony McCoy, Steven Sheffield, Dr. Donnell), thank you for all the help from making sure there is internet connection to getting test rigs working to the paperwork for submitting the documents.

This material is based on research sponsored, in part, by Air Force Research Laboratory under agreement number FA8650-15-2-5401 as conducted through the flexible hybrid electronics manufacturing innovation institute, NextFlex. Also thank you to all the previous

support over the years including NDSEG fellowship, FACES fellowship program, SRC and IBM.

Also, MANY thanks to the many friends who have supported me throughout the years. friends (Xiajia (XJ) Wang, Victor Huang, Tim Hsu, Jaime Zahorian, Matt (Mathias) Henry, Aishia Henry, George Mathai, Toby Xu, Rebecca Xu, Sophie Parks, Lisa Oakes, Jeff Oakes, Heather (Humpherys) Paxinos, Sneha Narayanan, Anada Barua, Mark McCurry, Sanzida Sultana, Yiming Kong, Amey Vidvans, Yizheng Chen, Therese Ngaya, Heidi Ho, Richard Zhang, Tommy Lambert, the Coles, Michael Kirka, Jenna Fu Chan, the Coopers, Bhaskar Baht, Ashley Bernal, Eva, Wily Alas, Linda Al-Hmoud, Chi-Chi Esimai, Pedro Soza, Rebecca Dickey, Judith Sherrill, Erin McPillian, Charles McPillan, Meredith Casey, Timothy Kassis, Gregory Phillips, David Murphy, Brian and Stephanie Beck, Stephanie Doan, Pum Kim, Matt Habbib, Sukwon Choi, the Enes, Brain Post, Xiaohong Jia, Longke Wang, Yaser Bastani, Sima Didari, Ali Tabei, Parag Thadesar, Sameer Vadhavkar, Ara Parsekian, Thomas Herrmann, George Woo, Hao Wu, Dennis Zhou). Without support, this document would not be possible.

To all those who read this paragraph, Georgia Tech is known for its high-quality research and one of the top ME graduate programs in the country, but really, it’s the heart and the passion of the community in and around Georgia Tech/Atlanta. Please have eyes open to see and ears ready to hear deep wisdom, and a heart ready to make lasting memories and unbreakable bonds.

TABLE OF CONTENTS

LIST OF TABLES

LIST OF FIGURES

LIST OF SYMBOLS AND ABBREVIATIONS

ACF	Anisotropic Conductive Film
AFM	Atomic Force Microscopy
APDL	Ansys™ Parametric Design Language
C4	Controlled Collapse Chip Connection
CTOD	Crack-Tip-Opening Displacement
CZM	Cohesive-zone modeling
dpi	head feed rate
DSC	Differential Scanning Calorimeter
dxf	Drawing eXchange Format
EDS	Energy-Dispersive x-ray Spectroscopy
EMC	Epoxy Mold Compound
ENIG	electroless nickel immersion gold
FEA	Finite-Element Analysis
ICA	Isotropic Conductive Adhesive
IPA	Isopropyl Alcohol
LCP	Liquid Crystalline Polymer
PET	Polyethylene terephthalate
QFN	Quad flat No-leads package
SDT	Tool combination of DSC and TGA
SEM	Scanning Electron Microscope
SERR	Strain Energy Release Rate
SIF	Stress Intensity Factor
SMD	Surface Mount Device
TCP	Tape-Carrier Package
TGA	Thermogravimetric analyzer
UV	Ultraviolet
VCCT	Virtual Crack Closure Technique
wt%	Weight percentage
(α,β)	Dundurs parameters
a	Crack
dU_e	Incremental elastic work
dU_f	Incremental work for fracture surface
dU_p	Incremental plastic work
dW	Incremental external work
E	Young's Modulus
G	Strain energy release rate (subscripts: I, II, and III designate mode & C critical)
K	Fracture toughness

l	Length
P	Load
r	Radius
U_e	Elastic strain energy
U_p	Plastic stain energy
v	Poisson's ratio
v	Displacement
Γ	J-integral's path
Δa	Incremental crack distance
ΔA	Incremental crack area
ε_e	Oscillatory exponent
μ	Shear modulus
π	Pi
σ	Stress
ϕ	Mode-mixity

SUMMARY

Flexible substrates with printed electronics are being increasingly sought for the widespread and cost-effective use of flexible electronics. With printed ink on flexible substrates, several items need to be examined: synthesis of ink, deposition of ink, curing of ink, line and spacing of ink, adhesion of ink, fracture strength of ink, electrical characteristics of ink, etc. Among these items, adhesion of ink to the substrate plays an important role in the overall reliability of printed ink on flexible substrate. When ink is printed on flexible substrates, assembly of surface mount devices on such printed pads is a challenge, especially if one desires to use a fully additive process. For such assembly techniques, various process parameters need to be identified and the strength of the joints needs to be assessed.

The research has determined modified experimental techniques to determine the adhesion and interfacial characteristics of printed conductors, and the research has shown that the developed techniques can be used on different substrate and ink materials. The developed techniques have addressed delamination both under shear and peel modes, and the dependence of adhesion characteristics on process parameters has also been studied. A sequential crack extension numerical technique has been implemented to determine the critical energy release rate for the delamination of printed conductors from a polymer substrate, and it is seen that the critical energy release rate is in the order of 100 J/m^2. This work has also developed and assessed a fully-additive printing process for assembling surface mount devices on flexible substrates. Using different process parameters, this work has examined the joint integrity of such fully-additive printing process for component

assembly. Overall, this work has added important insight into both printed material adhesion as well as the integrity of additive-printed interconnect joints.

.

INTRODUCTION

Printed flexible electronics offer not just flexibility, but have other advantages in terms of manufacturing, and sustainability. Since flexible substrates are foldable, twistable and stretchable, they are used in broad range of applications including internet of things (IoT), to medical devices, to connections in hardware. Flexible electronics have been around for decades with the base of polyimide substrate and cu foil. Recently with newer application IoT space, flexible electronics need to be space-efficient and unobtrusive sensors that are sustainable, but low-cost to manufacture. In 2018, the smart phone market started a new phase of foldable phones, with Samsung and Huawai revealing products that allow users to carry a phone with a tablet size screen [1]. Stretchable electronics are integrated into clothes and tattoo patches for health monitoring [2, 3]. Manufacturing price reductions are possible with larger working area flexible substrates with lower weight, which are easier to transport. Sustainability is a newer driver in the flexible electronics field as recyclability, biodegradable and biocompatibility are becoming more of a concern. This push is leading industries to explore new material sets to use in flexible electronics.

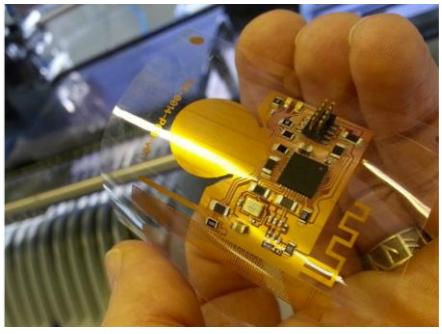

Figure 1: Flexible electronics source [3]

With the new stage of materials, printed electronics are moving to flexible electronics due to easier production integration for both substrates and films (ink, laminated films or pastes) by printing tools. Since printing can be performed outside of a cleanroom environment, there is a benefit of lower overhead production costs as well as reducing the need to store spare parts. Also, printing is valuable for its adaptability in initial prototyping stages, where on the fly design changes can be more easily accommodated. However, printed electronics technology needs to address the concerns with qualification to be production-level ready. These qualifications are based on the industry test standards like IPC 9204, ASTM D813 and ASTM E1877-15 for quantifying the reliability and material properties important for determining a sound product.

Reliability testing of flexible electronics includes mechanical loading such as bending, folding, twisting, and stretching of the substrates as well as thermo-mechanical loading due to thermal cycling or thermal storage. With these loadings, debonding or cracking of the layered films or assembled devices from the substrate can cause overall product failure. Adhesion quality is one of the important indicators for the reliability of the flexible electronics [4].

1.1 Adhesion experimental techniques

The basis of the printed film adhesion techniques follows from five thin-film adhesion techniques: peel test, tape peel test, blister test, indention tests and beam bending tests [4-8]. Before determining the appropriate test technique to use, it is important to consider how easy it is to prepare the sample, the sample limitations, what type of data is collected, the control factors, and the equipment availability. It is also important to understand that the

printed ink film is harder to peel at the intended interface of the substrate and film compared to thin films. For porous-ink sintered films, the sintered nanoparticle structure creates many crack initiation points within the film at each nanoparticle connection. For printed films with fillers and a polymer matrix ink, the polymer matrix may have weaker adhesion to the filler than the polymer to the substrate.

For a peel test, the thin film is peeled away from the substrate while the peel force and distance of the peel are monitored. Commercial equipment is available, but it requires that it must be easy to pull the peeling film. As the film is peeled at constant rate perpendicular to the surface, the force will become constant at steady-state once the initial slack is taken out from the peel arm. The steady-state information is semi-quantitative since the experiment assumes the film did not have a large plastic deformation throughout the film, nor does it consider the energy needed for the film to transform.

A common adhesion test is the tape peel test with commercially available kits. For the tape peel test, a grid pattern is scratched into the film and then a piece of tape is affixed to the film. After about 60 seconds, the tape is peeled away. Afterwards, the grid pattern is examined to see if any of the film squares are removed by the tape. Depending on how many film squares remain, it is graded into a category to determine if the adhesion is good or bad. Categorization depends on how much of the grid structure remained; it was qualified by the amount left with a rating ranging from B0 (over 65% delamination) to B5 (no delamination) [9] If the adhesion strength of the film is greater than the tape, then all the films will have a good grade. So, the test does not qualify the films beyond B5.

The blister test is a fully-quantitative test technique, that can measure the adhesion strength. In this test, underneath the film there is an access port to apply pressure. A blister is created with the pressured air. With the pressure, there is a point where the blister will grow in diameter. However, this is a complex sample preparation since a structure with a sacrificial layer needs to be fabricated. Also, the film needs to withstand the pressure needed, and a custom fixture must be designed to apply the pressure and monitor the film's blister diameter.

Commercially available indentation tools are easily used to create a scratch in the surface of a brittle coating. However, the force and displacement results are difficult to quantify and may not be at the intended interface. The ink material is not brittle, and so this test is not applicable.

Beam bending techniques, like double cantilever beam (DCB)) or four-point bend (4PB), require a stiffer sample to undergo bending load. The bending techniques are direct and give quantitative data but have limitations with flexible substrate geometries. These tests are typically conducted on commercially available universal test stands, but the fixtures to the samples maybe custom made. Different fixtures can apply different loading directions, from the pure tensile, to mixing different shear modes also in a control manner, e.g. Brazil nut.

Table 1: Test method comparison for adhesion[7]

	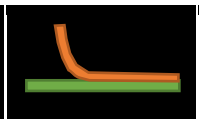	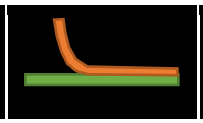			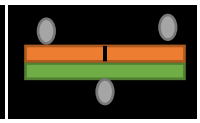
Technique	Peel Test	Tape Peel Test	Blister Test	Indentation Test/Scratch Test	Beam Bending Tests
Ease of Prep.	Straight Forward	Straight Forward	Complex	Straight Forward	Straight Forward
Sample limits	Peeling film must be able to be pulled	Adhesion strength weaker than tape	Films need to be able to withstand pressure as well as sacrificial layer fabrication	Hard Brittle Coating (scratch-only) Substrate influence (Indention)	Limited Sample Geometries
Data Type	Semi-Quantitative	Qualitative, no-go test	Fully Quantitative	Difficult quantitative	Quantitative
Loading	Control delamination rate Apply different angles	Limited	Limited	Limited	Different loading conditions based on fixtures
Commercially Available Equipment	Yes	Yes	No	Yes	Partly

Table 1 shows the thin-film adhesion techniques by comparing the preparation ease, sample limitations, data-type, loading capabilities and commercial equipment availability. Studies for the adhesion of printed inks on flexible substrates are limited compared to thin-film studies [10]. 90° peel test has been used to quantify the adhesion of ink on flexible substrates [11-13]. In one of the studies, an additional layer is electroplated to the printed film to thicken it so that the tool will be able to hold and peel the film as well as decrease the effect of energy lost due to plasticity. Such additional electroplating could affect the

interface of interest. Many ink on flexible substrate evaluations use the qualitative ASTM D3359-17 peel test [8]. As mentioned previously this only gives information for materials for poorer adhesion compared to tape, and it does not quantify the peel strength. An ink's strain energy release rate was calculated with beam bending techniques - double cantilever beam and four point bend - by curing it between stiffer composite material [14]. A stiffener is needed for the flexible substrate if beam bending techniques are pursued.

Joo suggested a modified button adhesion test, where a blank Si die is attached to the ink surface with an adhesive and then a die shear test is performed to remove the Si die with the ink film [10]. In a die shear test, a paddle pushes the die at a controlled displacement rate until the die becomes detached from the substrate. This test is more applicable for the assembled devices, but it is limited to the shear loading.

For the current work, the peel test will be the main technique explored. The peel test allows for easier preparation of the sample without any sacrificial layer. The peel test is easily adaptable for different mode tests by changing the angle. Also, the test lets the samples be aged before testing for the adhesion. However, there needs to be an additional consideration of the experimental set-up with these thin films since plasticity is not fully accounted for. FEA simulation needs to also be pursued to examine how the plastic strain energy can be accounted for in the peel test [15].

1.2 Flexible substrate assembly

Academic researchers, as well as those in industry, are currently pursuing assembly of components on substrates with printed conductors. Printed electronics assembly techniques with traditional tooling mainly focus on Ag paste and epoxy [16, 17]. For surface-mount

device (SMD) attachments onto flexible substrates, techniques available include wire-bonding, Controlled Collapse Chip Connection (C4) reflow, anisotropic conductive films (ACF), isotropic conductive adhesives (ICA) or pastes, and fully additive techniques [18, 19]. Depending on the technique, the direction of the active side of the chip, whether face up or face down, can affect the electrical performance as well as the footprint size needed to accommodate the chip. The technique may also the limit the type of chip layout, pitch between the bump interconnect, bump materials, and additional steps may need to be taken, like surface finish on top of the trace before assembly or underfill after assembly.

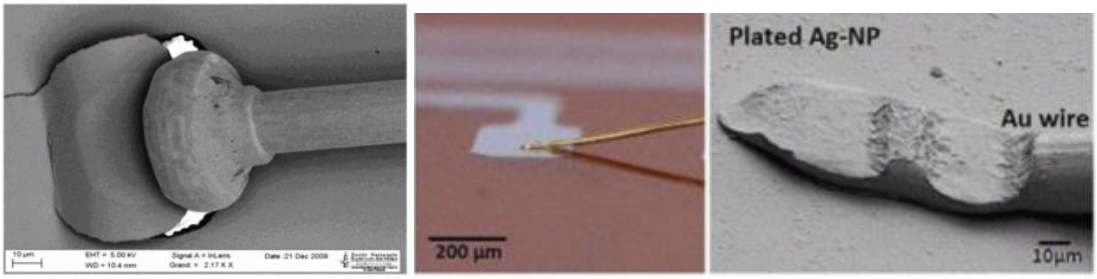

Figure 2: Wire bond demonstrated first without nickel coating and with nickel coating [19]

In wire-bonding as shown in Figure 2, Au wires are bonded to the die pad, swept, and then attached to the printed pads on the substrate. The active side is up with limitation of the pitch to a peripheral pattern, and this will decrease the electrical performance as well as require a larger footprint. Also, the printed pads need to be reinforced with electroless nickel immersion gold (ENIG) for attaching the wirebonds, but there is no bump to be modified, nor any need for underfill.

Traditional solder reflow (C4: Controlled Collapse Chip Connection) is a key technology for assembly on rigid substrates with copper pads because it allows for mass

production attachment of components. The active side is down, which allows for higher I/O count in the area array and better electrical performance in the smaller footprint. However, the solder reflow does not work with most printed Ag conductors and the soldered components will need the ENIG finish to act as a barrier layer to keep the solder from consuming all the silver in the pads. Solder reflow would also require high-temperature processing which may not be amenable to several low-temperature polymer substrates typically used in flexible electronics. Additionally, an underfill step is needed after assembly.

Isotropic conductive bumps are formed by dispensing or stencil printing conductive adhesive or paste onto die pads. These spherical bumps can be brittle. For a better connection like as seen in Figure 3, Au bumps can be dipped into an adhesive and assembled onto the substrate. This technique lets the active side be down and allows for higher I/O with area array for the pitch. However, it does require underfill, but no ENIG.

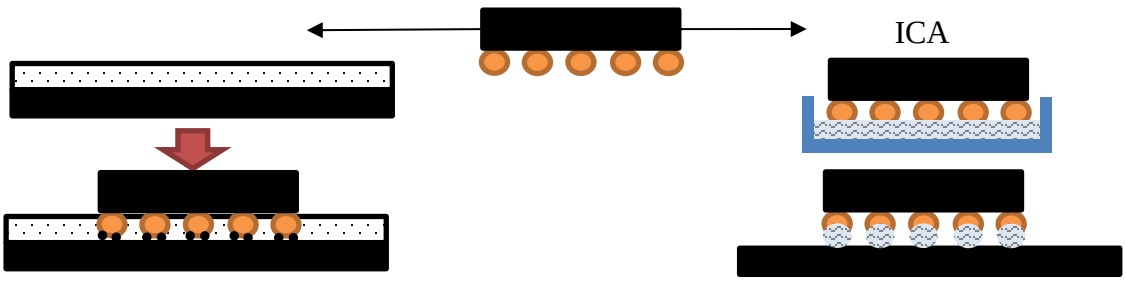

Figure 3: Schematics illustrating assembly using ACF and ICA for a flip chip

Anisotropic conductive films (ACF) are often used for tape-carrier packages (TCPs). Using them is often considered a thermo-compression bonding technique because of the pressure and temperature needed to apply during bonding the package to the film. Depending on the particle size and spacing of particles of the ACF, limits must be

considered for the pitch of the device, so that there are no shorts formed. Also, higher pressures are needed to deform the particles and the stiffer Au bumps are able to apply the pressure better than soft solder bumps. The ACF film acts as underfill, so there is no need for underfill step nor the need to look at ENIG finish on the ink traces.

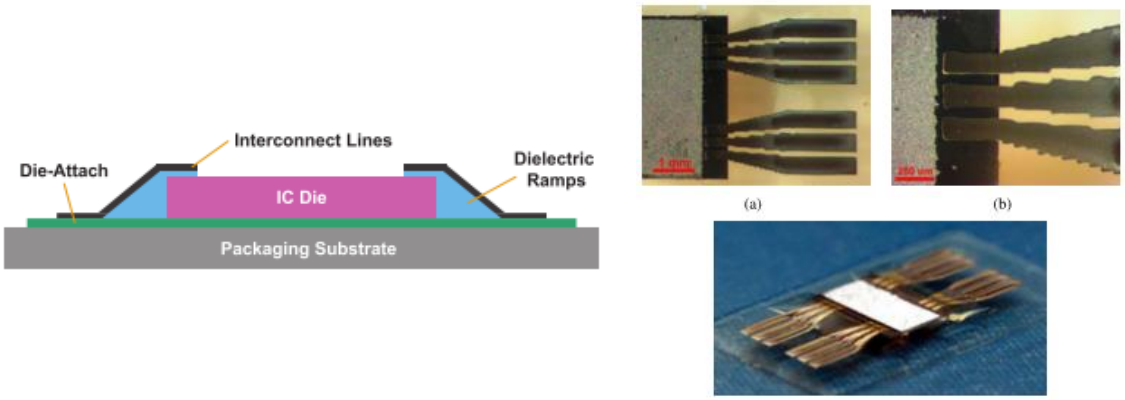

Figure 4: Dielectric ramps [20]

In terms of fully additive techniques, there are two main types identified in literature: dielectric ramp and sintering technologies. The dielectric ramp utilizes a printed dielectric ramp around the edges of a die to be able to print conductive traces from the die pads to the substrates. The printer builds both wiring and interconnections in a single step as shown in Figure 4. In this process, the die is first attached to the substrate with its active side up before printing the dielectric ramp [20, 21]. However, this technique limits the assembly mostly to peripheral pad layouts, requires a large footprint, and has higher electrical parasitics due to longer trace lengths.

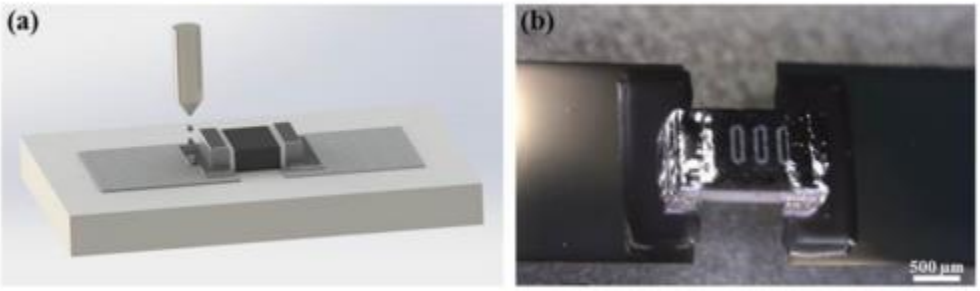

Figure 5: Fully ink assembly process which is limited to peripheral [17]

For better pitch scalability and electrical performance, sintering technologies offer the best solution [22]. This method uses sintering of Ag ink as a way of assembling components on flexible substrates, since Ag ink can be directly sintered onto the trace without the metallic coating to protect the traces. By working with this method, the assembly is done after ink printing. This is the opposite of the work shown in Figure 5, where they placed the resistor first and then print the ink for the joint. This will have the same limitation of only peripheral pad layouts as the dielectric ramps. Also, Ag ink is conductive after oxidizing and has sintering temperatures below 250 ºC [13].

Table 2: Assembly onto ink traces comparison

			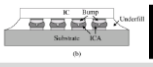	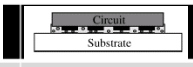		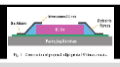
Technique	Wire-bonding	C4 Reflow	Isotropic conductive bumps (ICA)	Anisotropic Conductive Film (ACF)	Sinter Bump	Dielectric Ramps
Active Side	Up	Down	Down	Down	Down	Up
Electrical Performance	Low	Good but EM concerns	Ok	Ok	Great (Low parasitics, good EM perf.)	Low
Pitch limitations	Peripheral Pref.	Area Array Pref.	Area Array Pref.	Area Array Pref.	Flexible	Peripheral Pref.
Footprint	Large	Chip scale	Chip scale	Chip Scale (Pressure)	Chip scale	Large
Alignment	Yes	Yes	Yes	Yes	Yes	No
Underfill	No	Yes	Yes	ACF acts as Underfill	Yes	No
Bumping	No	Solder bumps	Au Bumps	Au Bumps	Au Bumps	No
Surface finish	Required (ENIG)	Required (ENIG)	No	No	No	No

Table 2 compares all the techniques of assembly by the restrictions on different aspects of the build. The cheaper option with less upfront work may be to do the additional ENIG surface treatment, so that the traditional assembly techniques of wire bonding and C4 reflow may be used. However, to pursue the best electrical performance this work will focus on the sintering technique for a fully additive assembly process. The pitch performance is flexible, with the ability to do the dip process for the array bumped chips and the ability to do the printing technique on the printed traces.

1.3 Gaps in existing literature

For printed inks on flexible substrates, adhesion strength has been identified as an important indicator for reliability. In general for the printed film adhesion experiments, there is a gap between the experimental data from the adhesion tests and determining quantifiable adhesion data such as the critical energy release rate. It would be a step forward to find better ways to measure results for different load types or thermal aging affects on the interfacial adhesion strength. In literature, there are many applications of thin film adhesion techniques which could potentially be used to determine the critical load to debond the printed ink from the flexible substrate. This critical load information can then be used in numerical simulations to extract the critical energy release rate (Gc).

With regards to assembling onto flexible substrates that have printed traces, various methods have been discussed, but the focus of this work is on sintered bump techniques due to the emphasis on electrical performance. For these fully additive sintered techniques, there is a gap in the literature for assembly technique for large production scale and thermal aging.

An all-silver-ink process for substrate creation in the surface mount device (SMD) assembly should allow for quicker production cycle, cheaper manufacturing, and custom and low-quantity production [23]. To optimize the process, several items need to be examined for printed ink on flexible substrates: synthesis of ink, deposition of ink, curing of ink, line and spacing of ink, adhesion of ink, fracture strength of ink, electrical characteristics of ink, etc. Among these adhesion of ink to the substrate plays an important role in the overall reliability of printed ink on flexible substrates [4].

When ink is printed on flexible substrates, assembly of surface mount devices on such printed pads is a challenge, especially if one desires to use a fully additive process. For such assembly techniques various process parameters need to be identified and the strength of the interconnect needs to be assessed.

OBJECTIVES AND SCOPE OF THE RESEARCH

Adhesion of printed inks on flexible substrates under thermal and mechanical loading continues to be a concern for flexible, bendable, and stretchable electronics. Although qualitative evaluation tests for adhesion are available, quantitative tests are still evolving for printed inks. With printed films from solvent inks, the thin films may not be continuous due to the printing settings. Also, the ink films are designed to be highly porous which inhibits the pulling/shearing of the film directly. Thus, adhesion tests should be developed as well as appropriate numerical models need to be explored for obtaining interfacial fracture parameters.

In addition to adhesion characterization, assembly of components onto Ag-ink traces printed on flexible substrates through all-ink process needs to be developed. Such a process must consider the temperature limit of the flexible substrate as well as the metallurgical bonding capability of the intended joint and the SMD's electrode stack-up. To form a good Ag joint, often pressure is applied during the applied temperature profile. An oven reflow process is ideal, since a long temperature time is associated with Ag ink sintering.

1.4 Objectives and scope of research

Based on the above considerations, there are three areas of focus in this research. First, adhesion characteristics of the ink to flexible substrate needs to be determined experimentally with innovative tests. Second, a numerical modeling scheme needs to be developed to extract interfacial parameters from adhesion tests. Third, a fully-additive printing process for assembling surface mount devices onto flexible substrates needs to be developed. An overview of the objectives and scope of the research is presented in Figure

6. The overall goal of this work is to demonstrate a fully-additive assembly process and to characterize the adhesion strength of the printed ink on flexible substrate.

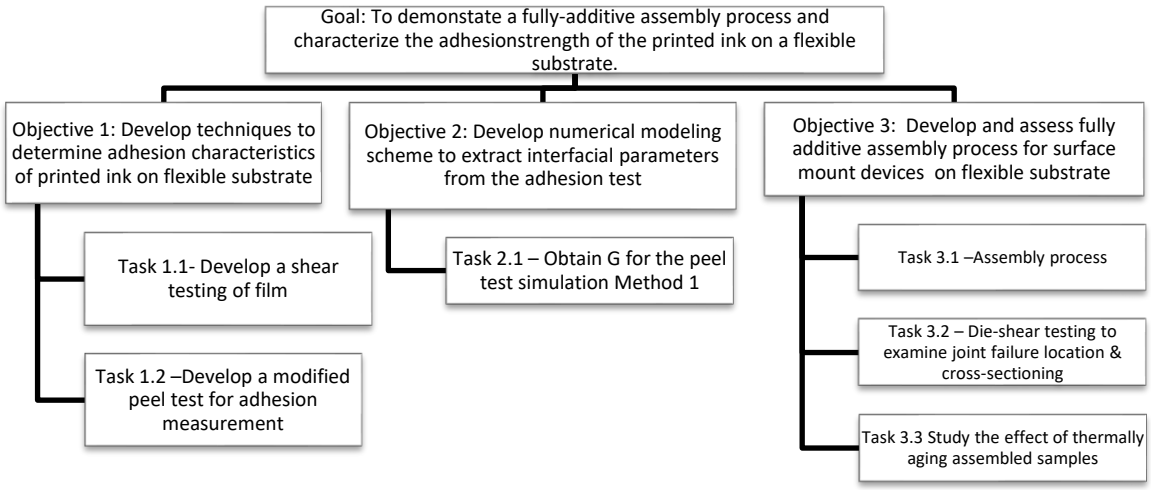

Figure 6: Overall goal and objectives for this work

1.4.1 Development and demonstration of innovative adhesion tests

The first objective of this work is to develop and demonstrate techniques to determine adhesion characteristics of printed ink on flexible substrate. Two types of tests were examined for printed inks: shear and peel. The shear test developed is analogous to the button shear test found in testing of epoxy mold compounds to Cu lead frames. This test was used for as-printed as well as for thermally treated inks. When developing the modified peel test, two different peel configurations were considered to characterize the interfacial adhesion of printed inks.

1.4.2 Finite-element analysis of peel test

The second objective of this work is to develop numerical modeling scheme to extract interfacial parameters from the peel test. Finite-element modeling was done through commercially available ANSYS^{TM} software to extract the interfacial parameter.

1.4.3 Fully-additive assembly process

The third objective of this work is to develop and demonstrate a fully additive assembly process for surface mount devices. Parameters to consider for the assembly process included: temperature profile, applied pressure, and duration of pressure. For this process, the SMD was placed with initial pressure, but did not have any pressure applied while in the oven. Upon assembly, some of the devices were electrically examined. Cross-sectioning was also done for examining joint formation. Die-shear testing afterwards was done to evaluate the joint strength, and SEM and optical microscopy were done to understand the areas of failure. In addition to as-assembled samples, some of the samples were thermally aged, and the electrical resistance measured.

1.5 Dissertation structure

This dissertation is organized into 8 chapters. Chapter 1 gives a brief introduction into current literature and identifies the gaps in the existing literature. Chapter 2 gives the objective and outlines the methodology used for each of the three objectives identified to accomplish the goal of a fully-additive assembly process. Chapter 3 focuses on the ink characterization. Chapter 4 focuses on the button shear experiments for ink adhesion and the results from experiments. Chapter 5 focuses on the two different peel methods for ink adhesion and the results from experiments. Chapter 6 examines finite-element analysis (FEA) to extract interfacial fracture parameters. Chapter 7 develops the ink assembly

process and provides results from the process. Chapter 8 concludes this work highlighting future applications as well as the research contributions. In addition, there are appendix sections to help understand the background: Appendix A provides sample preparation considerations for imaging with detailed instructions about scanning electron microscope (SEM) set up, Appendix B discusses ENIG processing, and Appendix C discusses stress and strain detection tools.

PRINTING OF CONDUCTIVE INK TEST COUPONS

For flexible printed electronics, various printing techniques are often employed. These include screen printing, aerosol jet printing, inkjet printing, gravure printing, flexographic printing, and several others. This dissertation deals with inkjet printing, and thus, most of this chapter focuses on inkjet printing. However, to provide a comparative background, aerosol printing is also discussed in a limited sense, and certain cleanroom techniques such as photolithography are also presented for cost comparison purposes. Screen printing uses polymer matrix with conductive filler particles, and screen printing is not the focus of this work.

Typically, silver (Ag) inks are used for creating the conductive lines/traces, and are not commonly used for joint formation [16, 24-27]. Understanding the ink characteristics of the specific printed ink is necessary for both the trace adhesion development and a fully-additive assembly process. Ag ink is similar to Ag paste and both have the same impacting factors – (a) ink composition: Ag particle size, geometry and distribution/concentration (b) processing parameters: deposition technique, sintering profile, and drying time and (c) design: layout and deposition path [28].

When discussing Ag ink for the sintered/particle films, ink composition has several parts including but not limited to particle characteristics, surfactants, suspension polymer, and particle concentration [28]. Often the silver ink particles have a coating to prevent agglomeration, since Ag clumps will interfere with the deposition by clogging the system. This coating layer needs to be removed either by chemical reaction or additional energy

provided by heat. With inks, often the solvents that act as suspension may evaporate at room temperature over extensive time periods.

While printing test coupons, various process and material parameters need to be considered. Even with the same type of viscosity and surface tension for the ink, the printed trace could be different depending on the printing technique as demonstrated in Figure 7. As seen, the aerosol-jet-printed trace is narrow and has good spatial resolution compared to the inkjet-printed trace. However, the aerosol-jet-printed trace is more porous resulting in higher resistance compared to inkjet-printed trace.

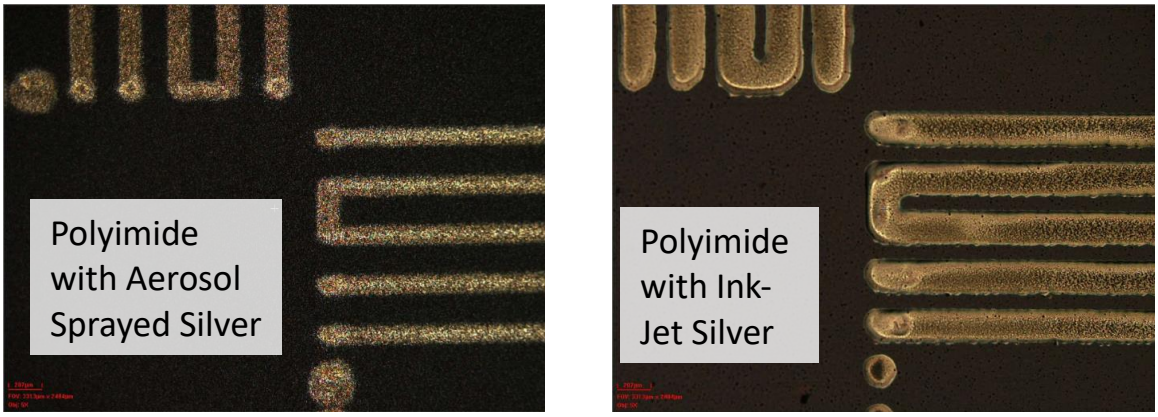

Figure 7: Same polyimide flexible substrate design with traces for measuring a flip-chip daisy-chain test vehicle printed by (a) aerosol jet printing and (b) inkjet printing

The aerosol printing is similar to the concept of spray painting, and so a fine mist of the particles were sprayed onto the surface, while the ink-jet drops ink droplets onto the surface. Ink-jet printed test coupons behave differently from aerosol jet-printed tested coupons due to changes in printing process, ink composition, curing profile, resolution limits, etc. [29]. For deposition, ink-jet printing is a good candidate due to its low cost with high efficacy and resolution compared to other techniques listed in Figure 8 [23] [30]. For

ink-jet printing, the main pattern parameters included: head feed rate (dpi), nozzle size, viscosity the nozzle can handle for ink, and the resolution of head movement.

	Photolithography	Shadow mask	Micro-contact printing	Inkjet printing
Cost	Extremely high	Low	Medium	Low
Area	Extremely small	Large	Medium	Large
Efficiency	Low	High	High	High
Temperature	High	Low	Medium	Low and High
Mask	Needed	Needed	Needless	Needless
Resolution	Extremely high	Low	High	High
Compatibility with polymer	Bad	Good	Bad	Excellent
Flexibility	Bad	Bad	Bad	Good, digital lithography
Compatibility with R2R	Bad	Medium	Good	Good
Material consume	Large	Medium	Low	Low
Requirement of environment	Clean rooms, vibration isolation	Low	Medium	Low
Process	Multi-step	Multi-step	Multi-step	All in one
Mode of action	Noncontact	Contact	Contact	Noncontact

Figure 8 Comparison of selected printing and patterning techniques [23]

For the layout and deposition, the applications design drives the thickness as well as line/space size needed to obtain the desired electrical, thermal and/or mechanical performance. For printers where multiple passes are needed to reach the desired thickness of the printed ink, the time of the print between the layers could range from a few minutes for a small design to 30 mins for larger footprint designs depending on the printer's nozzle configuration. During this wait time between two subsequent layers, the ink could dry due to solvent evaporation, and therefore, the characteristics of the printed ink will be dependent on the size of the sample printed. This in turn, could potentially change the adhesion strength of the printed sample.

For this chapter, the ink film processing is discussed in terms of materials, processing parameters, and design. Also, a quick evaluation of the adhesion of the printed ink through tape peel testing is discussed.

1.6 Inkjet printing

For this work, two main material sets were studied: Suntronic™ EMD 5730 printed on Rogers Corporation ULTRALAM® 3850HT Liquid Crystal Polymer (LCP) substrate and NovaCentrix® Metalon® JS-B25P Ag ink printed on Novele™ IJ-220 Polyethylene Terephthalate (PET) substrate. Various details of the two ink chemistries and processing parameters are discussed in the subsequent sections. These include: (a) ink composition: Ag particle size, geometry and distribution/concentration, (b) processing parameters: deposition technique, sintering profile, and drying time and (c) design: layout and deposition path [28].

1.6.1 Material set 1: Suntronic™ EMD 5730 ink on Rogers Corporation ULTRALAM® 3850HT LCP

In the first set shown in Figure 9, Suntronic™ EMD 5730 ink was deposited onto Rogers Corporation ULTRALAM® 3850HT LCP substrate that was particularly formulated to be stable at higher temperatures. Suntronic™ EMD 5730 ink is a solvent-based binder with a 40 wt% concentration of 50 nm Ag spherical particles.

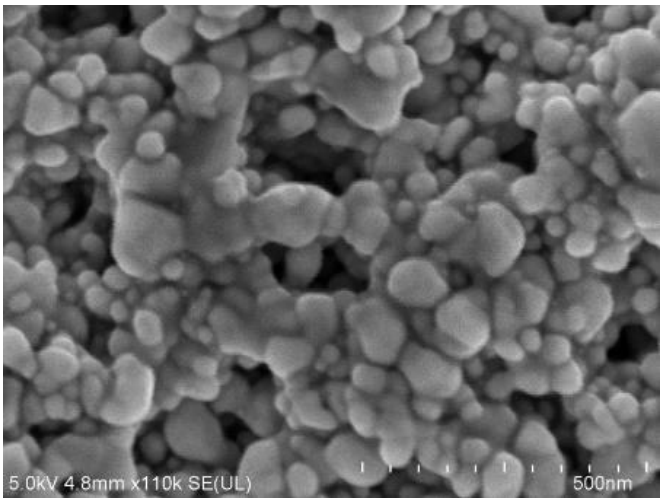

Figure 9: Scanning electron microscope (SEM) images Suntronic™ EMD 5730 Ag ink on Rogers Corporation ULTRALAM® 3850HT LCP Substrate

For processing, a commercial Fujifilm Dimatrix™ DMP 2831 inkjet printer, as shown in Figure 10, was used to deposit the first material set: SunChemical® SunTronic™ EMD 5730 ink onto the LCP substrate. The LCP substrate was attached to a heated stage held at to 60 °C. Since the vacuum on the stage did not hold the flexible substrate well, an additional Kapton tape was used to secure the flexible substrate. The printer head moved in the *x* and *y* directions with a fiducial camera for alignment. The replaceable cartridge had the ink for the print, and the print quality was primarily controlled by the cartridge calibration.

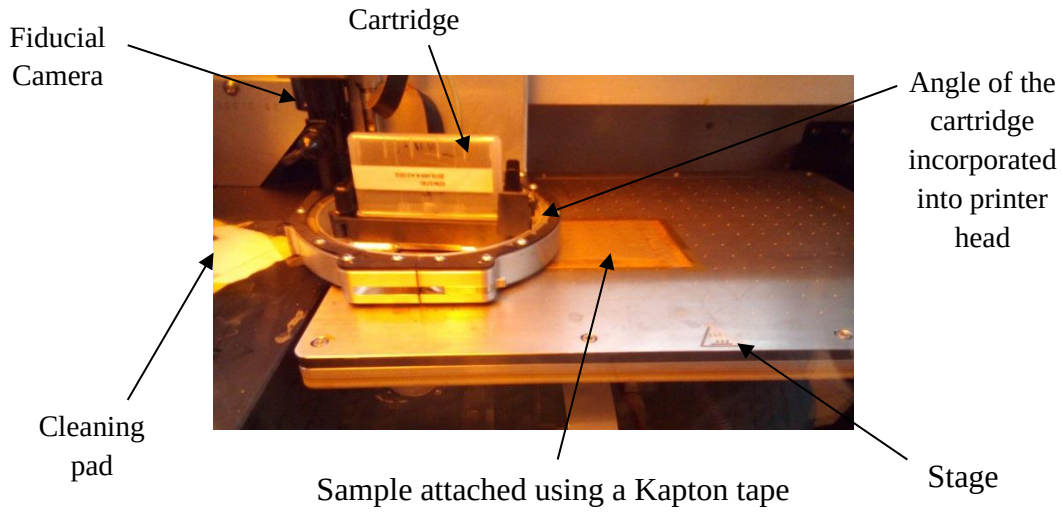

Figure 10: Stage and cartridge of the Fujifilm Dimatrix DMP

Cartridge calibration consisted of watching the droplets from the nozzle jets. In drop watching view as shown in Figure 11, view of the nozzles on the cartridge helped with ensuring the neighboring jets had the same length and timing. A blocked nozzle would pool ink instead of jetting and that would indicate that the jet needed cleaning. For a given print, a series of nozzles should jet together. The active number of jets impacted the print time.

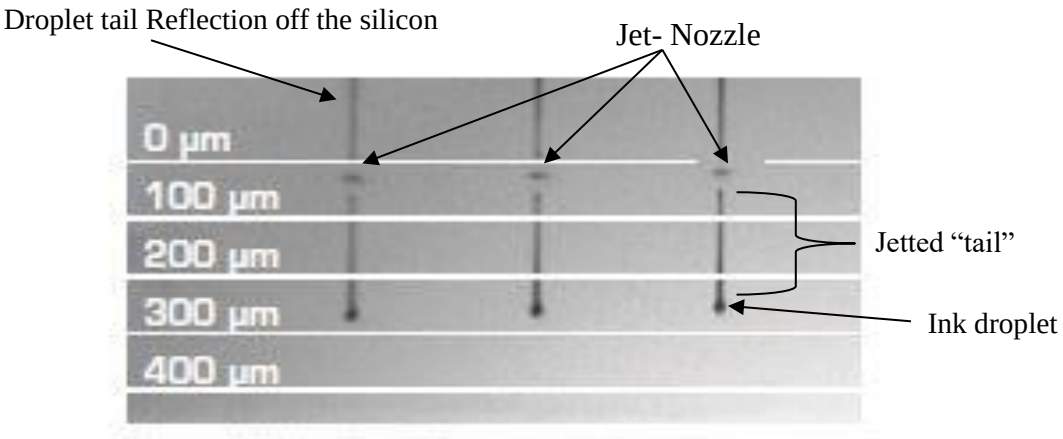

Figure 11: Drop watcher view of the ink jetting from the nozzles

Once the pattern was designed, the design was then uploaded in a Drawing eXchange Format (.dxf) to be converted into a bitmap image where the pixels indicated the drop locations. When the conversion from .dxf to bitmap is not done correctly, print errors and gaps as shown in Figure 12 could occur. Thus, careful examination of conversion is necessary.

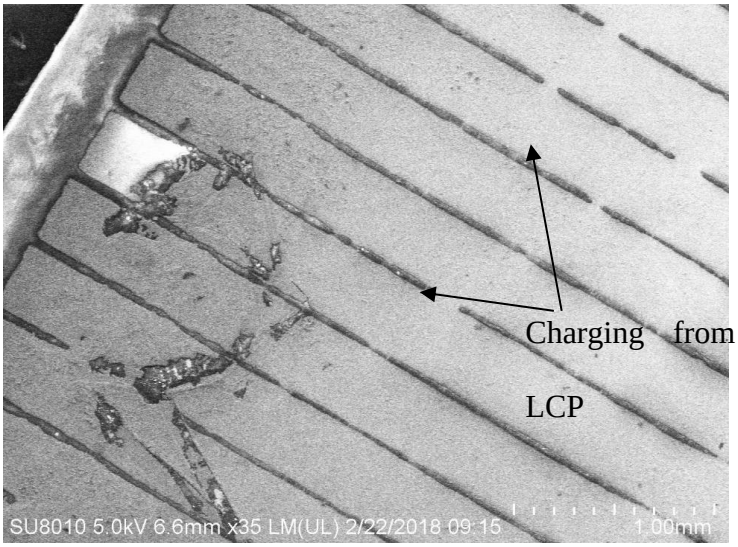

Figure 12: Inkjet printing may have conversion errors

For the SunChemical® SunTronic™ EMD 5730 ink, the sintering range suggested by vendor was 150 °C to 250 °C, and as a first step, an isothermal sintering temperature was determined through sintering characterization. Thus, a TA Instrument™ SDT 600 analyzer was used to determine when the solvent in the ink fully evaporated by monitoring the weight loss in the printed ink, by temperature sweeping from room temperature to 500 °C at a 10 °C/min ramping rate.

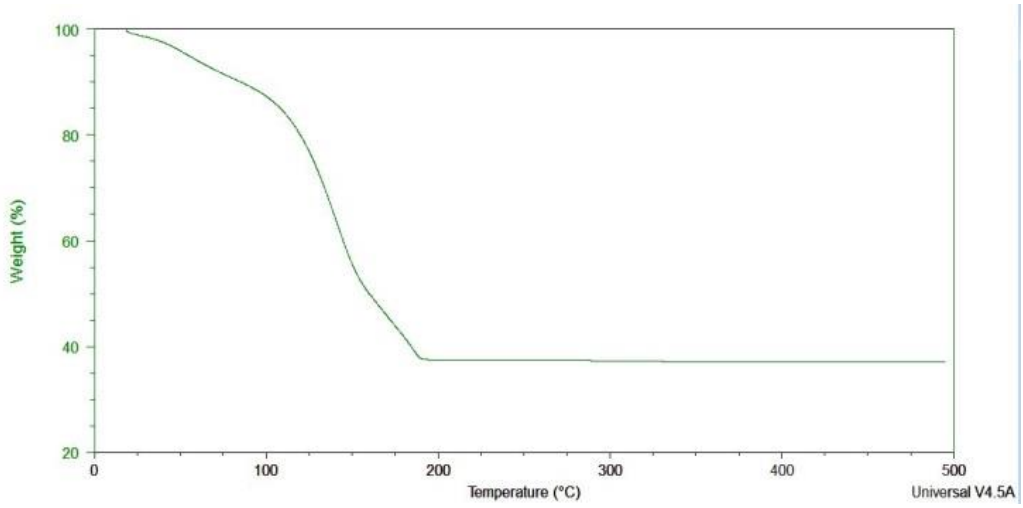

Figure 13: Residual weight of Suntronic Ink @ ramp rate of 10 °C/min with temperature run from room temperature to 500 °C

Accordingly, it was seen in

Figure 13 that the net weight of the ink after reaching a temperature of 200 °C stabilized and was about 40% of the initial weight indicating that almost all of the solvent had evaporated by 200 °C. As this temperature falls in the middle of sintering temperature range recommended by the vendor, and as this temperature is appropriate for sintering silver nanoparticles silver (e.g. [31]), it was chosen for sintering the ink in subsequent studies. After printing the samples, they were immediately placed in the oven for sintering without any air drying.

Although the samples were not intentionally air dried, the print time would affect the natural drying of the ink, and therefore, the print footprint and direction of printing should be appropriately selected to reduce the print time.

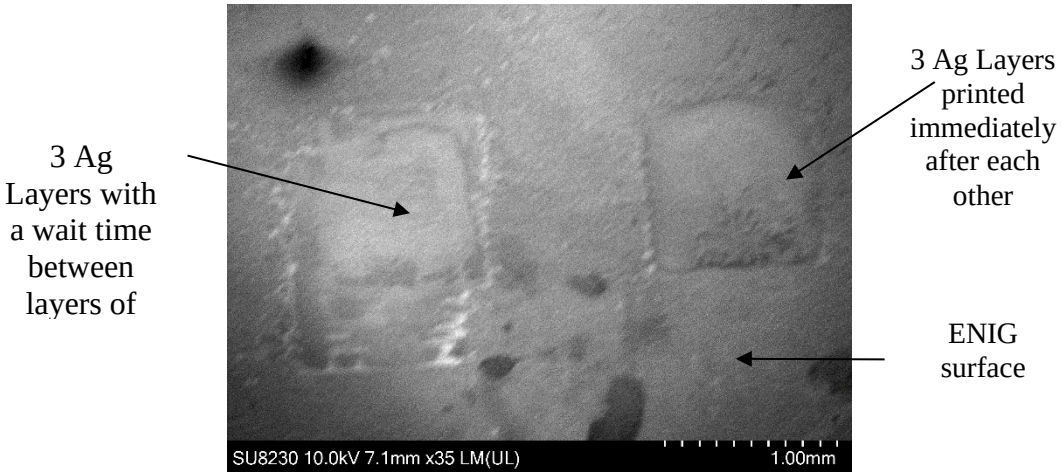

Figure 14: 1x1 mm squares on an ENIG surface with comparing if there is a wait time between layer prints or no wait time

Figure 14 shows 1x1 mm ink squares printed on an ENIG surface with and without wait times between layers. In Figure 14, the left square was printed with a 1st layer followed by a wait time of 40 mins before printing the 2nd layer; another wait time of 40 mins was added before printing the 3rd layer. The right square was then printed with 3 consecutive layers with no wait time. After the second square was printed, the sample was placed into an oven to sinter at 200 °C for 30 mins.

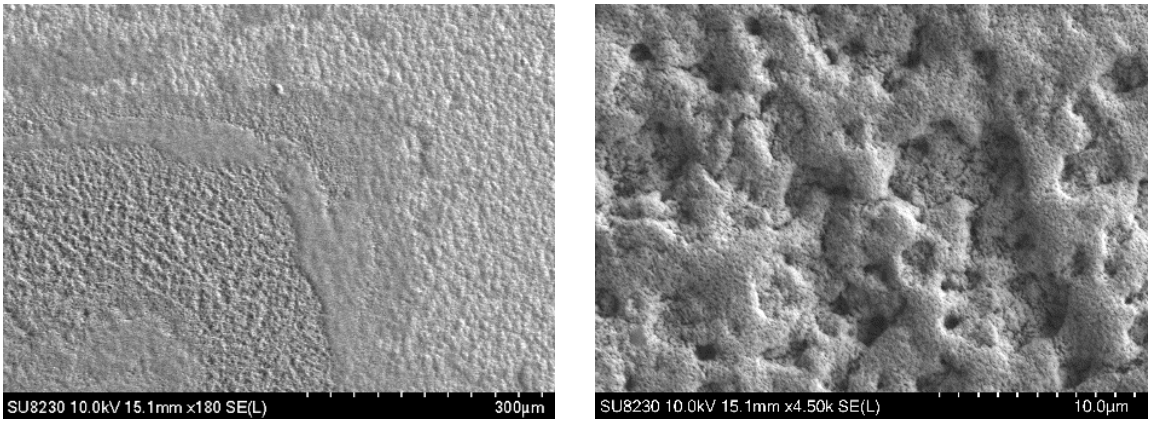

Figure 15: SEM Imaging of the 3 layer structure with wait time between printings of the layers with increasing zoom

SEM images of the square with wait time between layers (Figure 15) show a rougher surface compared to the images of the no wait between printing different layers (Figure 16). The images in Figure 16 show a more uniform structure overall, but the film did not have uniform thickness.

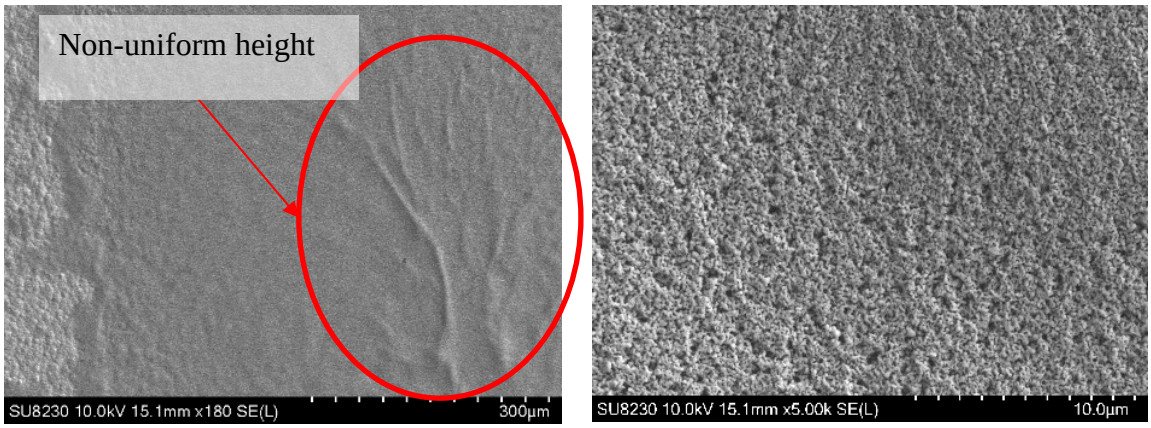

Figure 16: SEM images of 3 layers consecutively printed with porous structure

1.6.2 Material set 2: NovaCentrix® Metalon® JS-B25P Ag ink and Novele™ IJ-220 Polyethylene Terephthalate (PET) substrate

The second sample set consisted of NovaCentrix® Metalon ® JS-B25P Ag ink on Novele ™ IJ-220 Polyethylene Terephthalate (PET) substrate. Novele ™ IJ-220 PET is manufactured for NovaCentrix® by Mitsubishi Imaging (MPM), Inc. [32]. The transparent PET film has a special mesoporous film that allows for the ink to be conductive with a room-temperature dry. This mesoporous film wicks away the coating around the silver particle which prevents the nanoparticles from agglomerating in the Melaton® Ag ink

solution while in storage. The Melaton JS-B25P consists of an aqueous solution with 25 wt% nano Ag spherical particles (average 60-80 nm diameter).

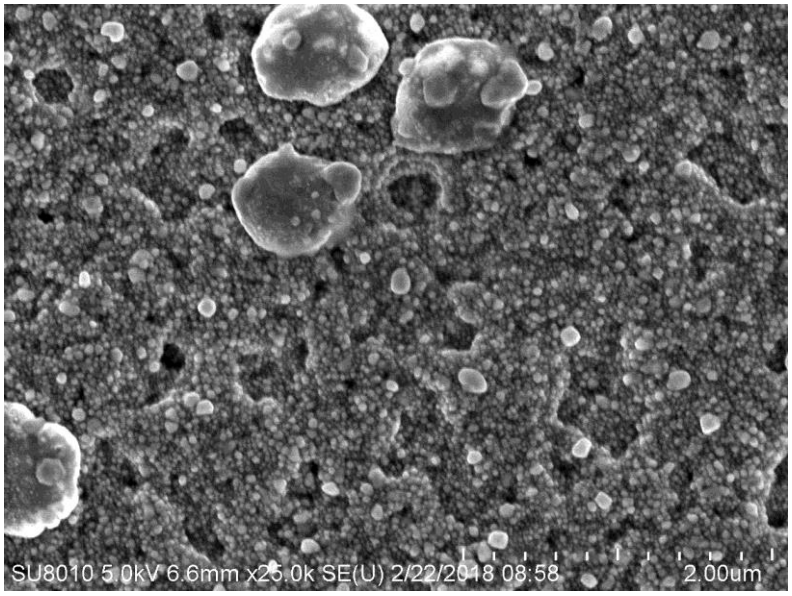

Figure 17: Scanning Electron Microscope image of NovaCentric® Metalon® JS-B25P Ag Ink on Novele ™ IJ-220 Polyethylene Terephthalate (PET) substrate

An Epson® Stylus® C88+ desktop ink-jet printer was used for this study. PET sheets were taken directly out of the package and used for printing. With this printer, only the printer head moved on one axis, and so the substrate was feed through. As this printer was inexpensive with a low print resolution, the printed samples were not of high quality (Figure 18). However, these print samples were still used in this study to demonstrate that the developed adhesion measurement techniques could be used with more than one material set and with more than one printer. However, the print process was much faster with the new printer.

The NovaCentrix Melaton® Ag ink printed on Novele PET substrate was dried in the air and did not undergo any thermal or light-pulse treatment. For this set of materials, only

one layer was printed due to alignment issues, since the PETsubstrate must be feed through the Epson® Stylus® C88+ printer. The time for print was quick and lasted only a few seconds.

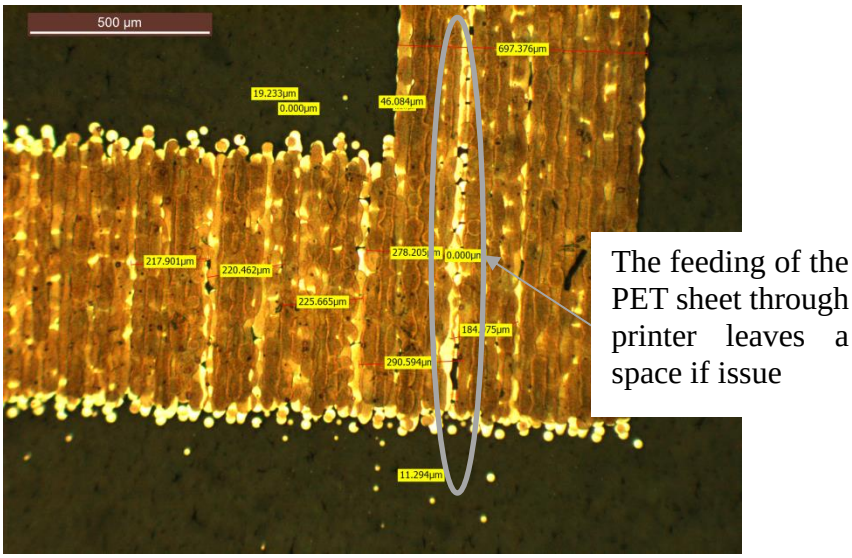

Figure 18: NovaCentrix Melaton® Ag ink printed on Novella PET substrate with special coating

1.7 ASTM D3359-17 Tape Peel Test

Although quantitative tests were discussed in the next two chapters, a qualitative adhesion test was first done for adhesion assessment. ASTM D3359-17 is a visual inspection adhesion test qualification test. In this test, a grid pattern was first scratched onto the printed ink to create a matrix of small ink squares, and a piece of tape was then adhered on top covering the entire grid pattern and held for 30-60 seconds. Then the piece of tape was peeled, and the number of small ink squares remaining on the substrate were used as an indicator of the adhesion strength. If 65% or more of the ink squares were removed from the substrate by the tape peel, then it was B0 (poor adhesion), and if none of the squares were removed, then it was B5 (excellent adhesion with no delamination) [9].

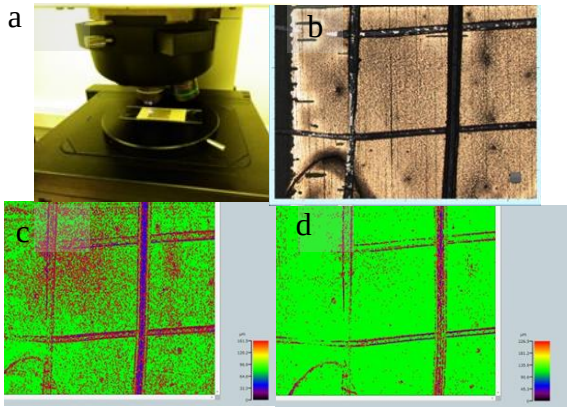

Figure 19: ASTM D3359-17 Visual inspection (a) Olympus LEXT 3D laser measuring microscope (b) optical view of sample and scratched grid (c) profilometer view before tape peel test and (d) profilometer view after tape peel test

In this test, the grid consisted of approximately 10 x 10 squares, and upon peeling using the tape test, practically all of the squares remained on the substrate indicating that the adhesion quality was of B5 standard. Figure 19b shows an example 2 x 2 square, as seen through the confocal microscope, out of the total of 10 x 10 squares. Figure 19c shows the laser profilometer view before the tape peel test, and Figure 19d shows the view after the test indicating that none of the ink squares peeled off. The green areas indicate the silver ink adhered to LCP.

The technical datasheet for the Novele PET substrate reports 5B adhesion for the Melaton® Ag ink [32]. Separate tests were performed on this material set, and the same class, “5B” was obtained for this material set as well.

1.8 Ink Printing Summary

Two different material sets were discussed in terms of the ink composition, processing techniques and the design of the blanket film to be used for adhesion testing. Even though

the concept was the same, using inkjet printing to deposit ink into a blanket film onto a substrate, the two material sets had different processing concerns and time involved to produce the film. Both printed materials demonstrated 5B adhesion according to ASTM D3359-17.

ADHESION CHARACTERIZATION-SHEAR TESTING

For the adhesion testing, the button shear test was explored to examine the printed ink in shear. Modification to the test was needed for handling the ink-jet printed films due to manufacturing considerations. (1) These films often are designed to be porous so that the films are more flexible by lower the stiffness. (2) Ink-jetted films often are composed of thin layers that are stacked-up to reach the desired thickness. (3) Depending on the tool and the file conversion to bitmap (or designated file extension) for the printer, the film may show indications of the path taken by the tool head with slight spaces between passes. A backing structure (epoxy mold compound button) was attached to the film to help with handling and applying the load. This backing structure made the technique adaptable across material sets and created a quantifiable way to make decisions between the sets.

Figure 20: XYZTEC™ paddle shear configuration

The XYZTEC™ adhesion test tool is a commercially available platform, which is capable of a wide range of adhesion tests including shear tests. For this study, the paddle shear (Figure 20) was used to shear the button. For the test, the head remained stationary while the stage moved at a designated rate.

1.9 Background on shear adhesion test of ink

To perform the shear test, a minimum height of the printed ink is required. In traditional "rigid" electronic packaging structures, components such as epoxy mold compound can be easily sheared from a Cu leadframe or a die can be easily sheared from a substrate. However, as the printed ink is not thick enough to perform shear testing and as it would take significant amount of time to print up a thick enough structure capable of shear testing, a button was attached to the top of the ink to be able to perform shearing experiments. In this experiment, an epoxy mold compound (EMC) with the dimensions as shown in Figure 21 was used as the button for shearing purposes. As the substrate is flexible, the substrate needed to be adhered to a carrier, rigid Cu-clad FR4 board, that was held flat and tight on the vice before shearing of the ink could be completed.

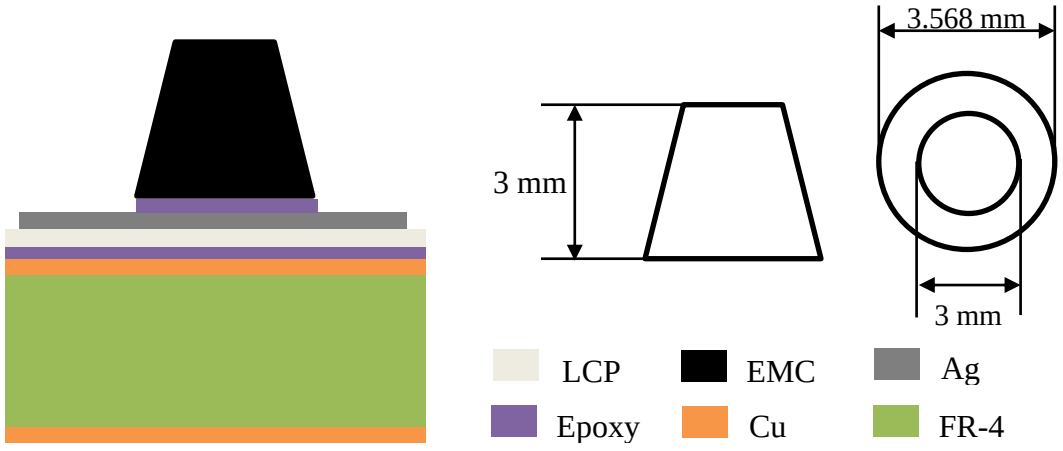

Figure 21: Schematic with the epoxy mold compound button and the cross-section of the stack up for the final structure need to be placed in the vice for the XYZTEC™ tool

1.9.1 Sample preparation and fixturing

Figure 22 shows the process for the button shear test. First, the flexible LCP was adhered to a carrier Cu-clad FR-4 board which was sized to fit into the vice of the shear tester. Next, preformed epoxy mold compound buttons were adhered to the ink's surface using a commercially available epoxy that was set at room temperature and fully cured in an hour. The room-temperature cure alleviates any concerns of microstructure change in the conductive ink. Due to the print droplet spacing and the print head path, directionality was observed in the film along the direction of the print, and the samples were prepared to examine the interfacial shear strength perpendicular to the direction of the print.

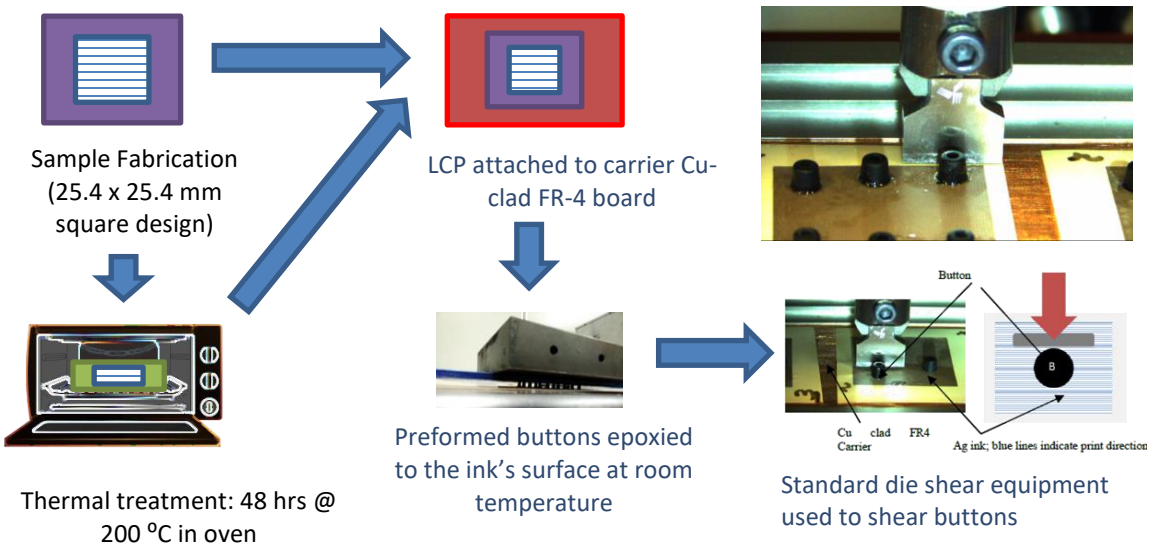

Figure 22: Schematic shows how the button shear test samples are prepared

1.9.2 Details of experiments and images

Four studies were pursued with the button shear test:

1) Control study without any thermal treatment or surface treatment
2) Study with thermal treatment of ink and without any surface treatment
3) Study with surface treatment of the substrate without any thermal treatment
4) Control study without any thermal treatment on a second set of materials

For comparison, the first two studies are discussed together to understand the effect of thermal treatment on shear strength. The third study is discussed in terms of the effect of ozone treatment on shear strength

1.10 Effect of thermal treatment on shear strength

For the first two studies, Table 3 lists various test cases studied for the button shear test. As seen, two to three layers of ink with and without thermal treatment were examined through the EMC button shear test. Figure 23 shows the SEM images of printed Ag that was thermally treated for an additional 48 hours at 200 °C, and as seen, the Ag particles had fused well, seemingly on the top surface.

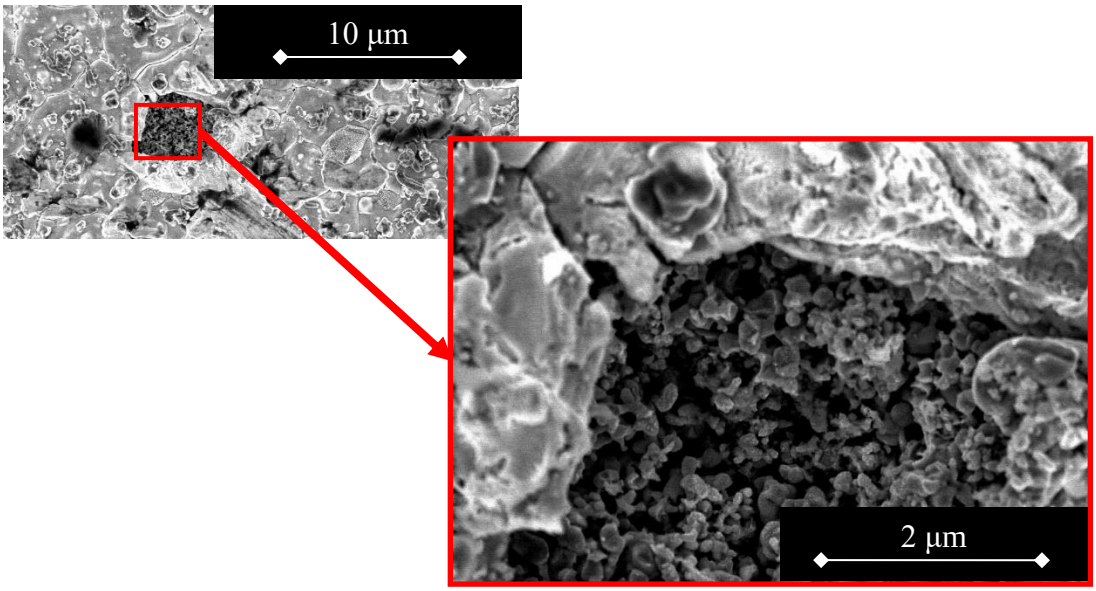

Figure 23: SEM image of a thermally-treated ink showing two distinct layers in Ag

1.10.1 Data from the experiments and failure analysis

For the first study, the XYZtec™ Condor Sigma was configured for the zone shear paddle attachment, and the shear testing was done at two different rates: 1000 µm/s and 16.7 µm/s rates. Multiple samples were done for each test as described in Table 3, and the results are shown in Figure 24. The load at which the button was sheared off was divided by the area of the button to obtain the average shear strength. The error bars represent the maximum and minimum of the test results for the sample type listed.

Table 3: Test samples

ID	Variables	
	# layers	Thermal Treatment
1	3	N
2	2	N
3	3	Y
4	2	Y

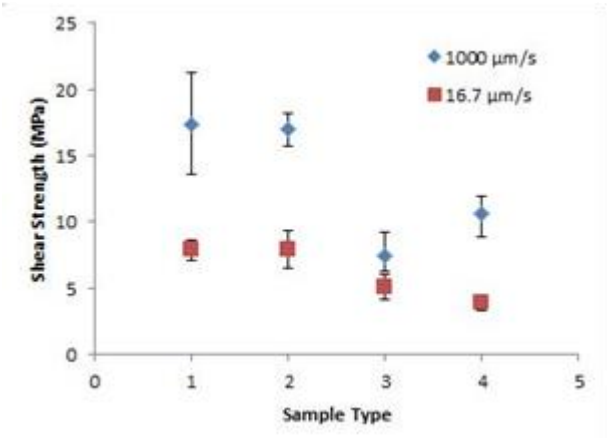

Figure 24: Shear testing results

In Figure 24, the number of layers did not influence the results. However, the thermal treatment seemed to have reduced the average shear strength by about 30% for 16.7 µm/s test and by about 50% for the 1000 µm/s test.

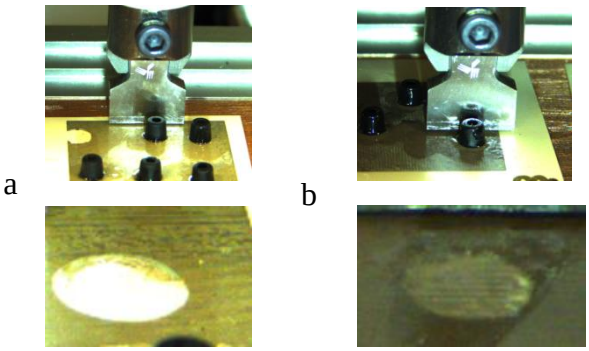

Figure 25: Shear testing (a) delamination between Ag and LCP after initial print and oven sintering (b) residual Ag on LCP indicating cohesive Ag failure after thermal treatment of ink

Upon examining the sheared surfaces, it is seen that thermally-untreated specimens had a clear delamination of the ink from the substrate, as shown in Figure 25a. However, the thermally-treated specimens had more of a cohesive fracture of the ink between layers with

different levels of fusion as shown in Figure 25b, and thus cohesive fracture demonstrated a lower strength. The images in Figure 25 were taken from the 1000 μm/s rate experiments. For shear tests conducted with a head velocity rate of 16.7 μm/s, the results were a mix between interfacial and cohesive failure, and the shear strength values appeared to be between the interfacial and cohesive fracture values.

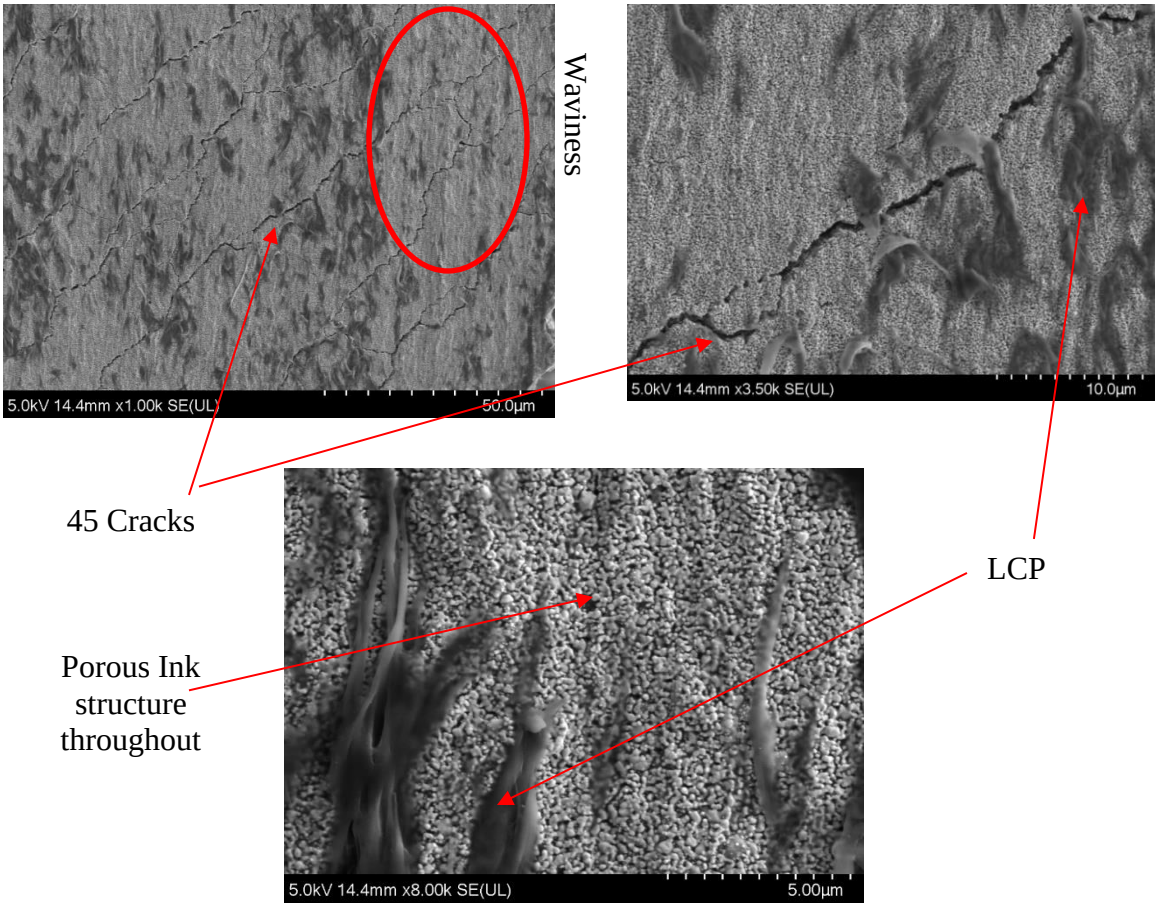

Figure 26: SEM image of the bottom side of ink still attached to the button - no thermal treatment. Images show different levels of increasing levels of zoom.

SEM imaging was performed on the bottom side of thermally-untreated ink layer after the shear test (Figure 26). The ink shows the porous quality that is desirable for lowering the stiffness across the whole surface. In the 50 μm image, a waviness was seen in the ink

corresponding to the LCP “grain” direction. For the thermally-untreated ink, cracks throughout the button bottom area are roughly 45° from the LCP “grain” direction and the break is between particles. LCP strands are attached to the ink from the test. However, most of the failure is delamination at the ink and LCP interface.

SEM imaging was also done on the bottom side of the thermally-treated ink after being sheared off (Figure 27). Two different levels of Ag ink are seen in the image: a dense lower section and a porous upper section, and the failure is mostly cohesive fracture in the ink. The two layers of Ag ink may explain the lower shear strength instead of increasing shear strength with thermal treatment as expected in literature [33].

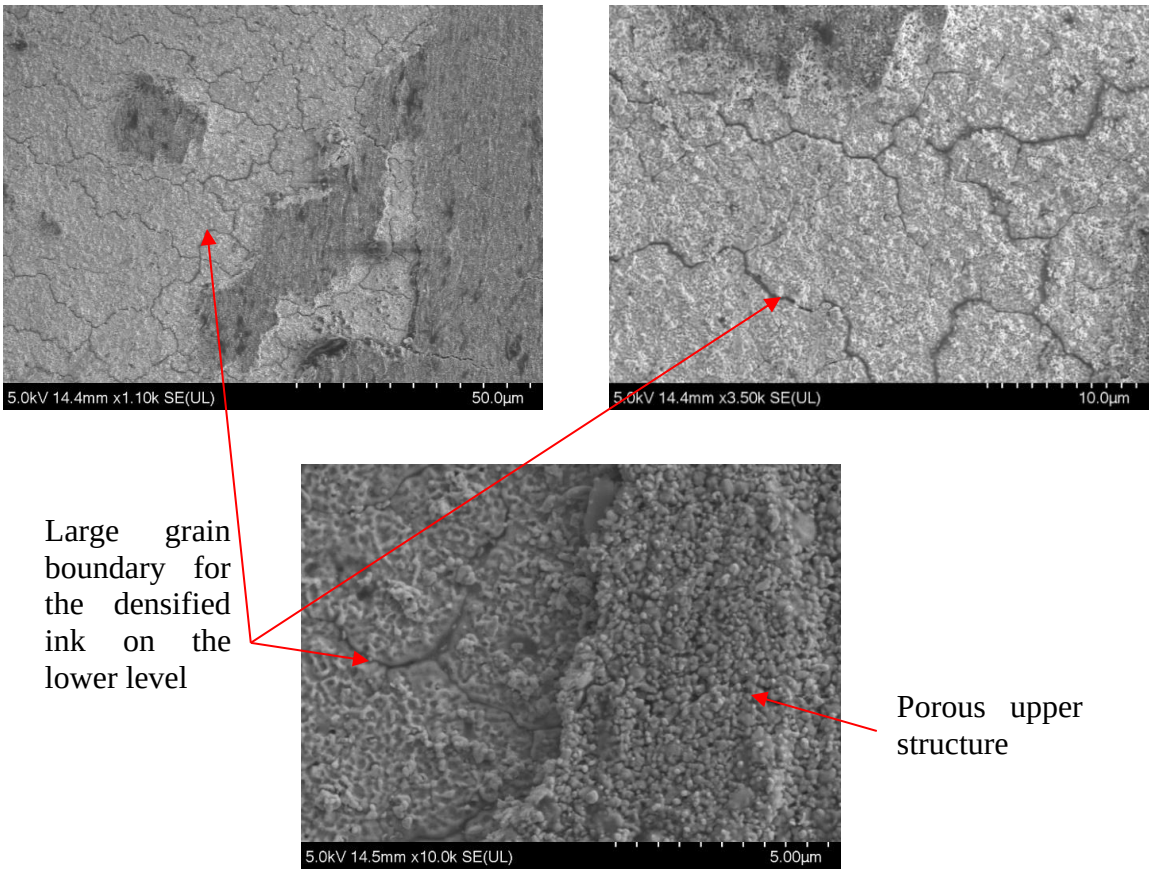

Figure 27: Button side SEM for the thermally treated sample. Images show different levels of increasing levels of zoom.

1.11 Contact-angle measurement

Adhesion strength of an ink to the substrate can be understood by looking at how the ink wets the surface of the substrate. If the ink wets the surface well, it will spread-out to cover as much surface as possible, and better adhesion. Poor wetting, on the other hand, will cause the ink to bead away from the surface as shown in Figure 28, and will result in poorer adhesion strength.

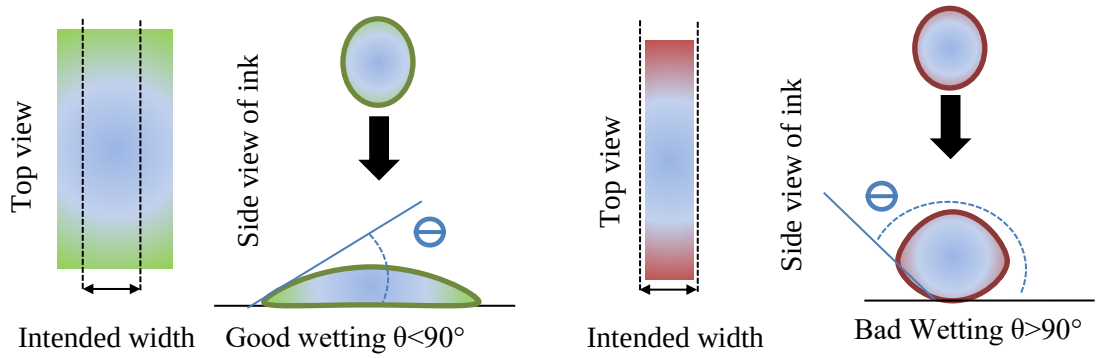

Figure 28: Role of surface wetting angle on printed ink geometry

As shown in Figure 28, the contact angle (θ) measurement characterizes the type of wetting. A Biolin Scientific Optical Tensiometer tool was used to measure the contact angle. The Attension® software automatically calculated the contact angle for both edges of the droplet. For the configuration in Figure 29, the droplet was manually created by pushing the ink through the needle with a syringe. Due to the low viscosity and manual implementation, the measurement image did not include the needle nor was the droplet formation rate controllable. Investigation of the contact angle with respect to UV clean ozone clean is discussed in the development of the shear test.

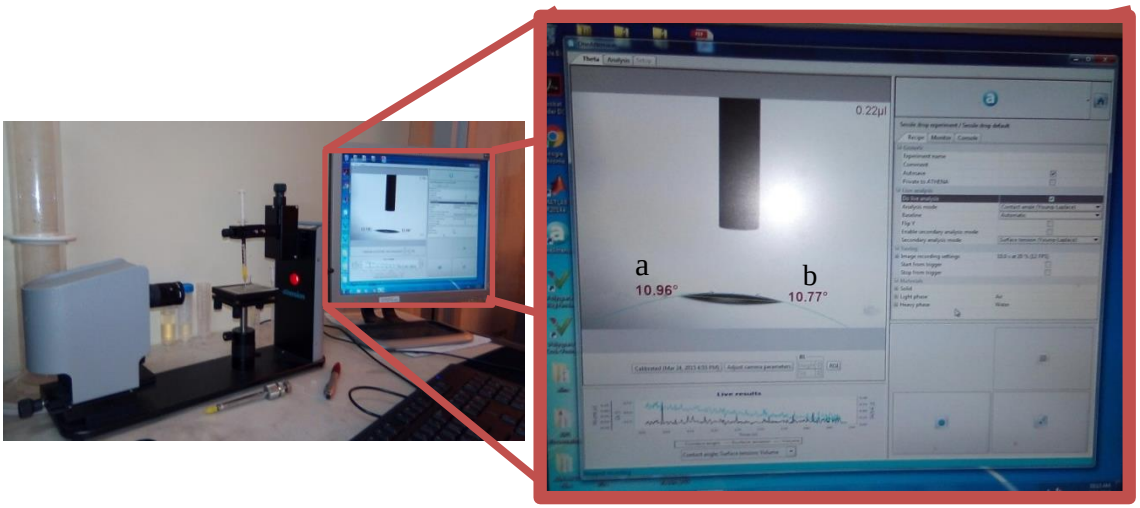

Figure 29: Biolin scientific optical tensiometer tool in ATHENA lab

For the study, the basic pre-clean process was a acetic acid clean, followed by acetone and then isopropyl alcohol (IPA) clean. The pre-clean was to help remove any larger debris on the LCP surface. Next, different UV ozone clean times were applied to various sample substrates as listed in Table 4. For the UV ozone clean experiments, time was the only variable. The sample substrate for the test cases was LCP.

Table 4: Ozone clean time description

Case	UV Ozone Clean (min:sec)	Sample Substrate
1	0:30	LCP
2	1:30	LCP
3	3:00	LCP
4	5:00	LCP

As shown in Table 4, the ozone clean time ranged from 30 seconds to 5 minutes. For each sample substrate a contact angle measurement was taken as is, after the pre-clean of

vinegar and solvent, and the last measurement was taken after the ozone clean as indicated in Table 5. A separate smaller piece of the sample substrate was cut from the main sample substrate due to platform size limitation of the tensiometer. The smaller piece was in the ozone chamber at the same time as the substrate that the smaller piece was cut from for the designated cleaning time of the substrate for creating the ink coupon. The smaller LCP substrate piece was first adhered to a glass slide using a tape. After the ink was deposited through the needle on to the LCP substrate piece, two angles were measured. These angles corresponded to the left and right angles captured on the camera monitor as shown in Figure 29. All the measurements indicated good wetting with contact angles below 90°. It was seen that the ozone clean reduced the contact angle. The 30 seconds and 5 minute preclean surface have higher angles than without treatment, and after the ozone clean angles reduced below the substrate without any surface treatment. adhesion strength.

Table 5: Contact angles from the ozone clean study

Substrate:		LCP	LCP	LCP	LCP
Ozone Clean time:		30 sec	1.5 min	3 min	5 min
Substrate without any surface treatment	a	49 °	49°	46°	23°
	b	46°	48°	45°	20°
Substrate after Preclean	a	54°	-	33°	53°
	b	48°	-	34°	50°
Substrate after Ozone Clean	a	33°	11°	15°	11°
	b	34°	12°	13°	11°

1.12 Effect of ozone treatment on adhesion strength

The EMC buttons were attached to the LCP substrates in the method described in Figure 22. The XYZTEC^{TM} Condor Sigma was also configured for the zone shear paddle

attachment, and the shear testing was done at a rate of 1000 μm/s. Multiple samples were done for each test as described in Table 5. In most test instances, the button was recovered and kept for further imaging and analyzing of the test data. For this study unlike the first control study, a few of the buttons were chipped during the shear testing and the remaining button chip was found still attached to the substrate as indicated in Table 6. "Button not recovered" means that as the sample was sheared, the button flew off and could not be located. It is seen that the shearing forces were between 100-200 N.

Table 6: Maximum shear force (N) for the button shear test

	30 sec	1.5 min	3 min	5 min
1	152.66	190.15	227.05	153.43
2	181.11	255.86	135.12	178.32
3	171.21	153.99	136.75	244.99
4	233.80	210.24	191.77	184.75
5	229.59	210.28	199.83	158.33
6	152.34	249.88	180.60	191.33
7	77.36	106.71	193.99	246.18
8	164.82	139.49	201.84	184.06

Button not recovered

Chipped EMC button

Using the shearing force values shown in Table 7 and dividing the force by cross-section area of the button, the average shear strength can be obtained, and such shear strength values are presented in Figure 30. The error bars represent the maximum and minimum of the test results for the sample type listed.

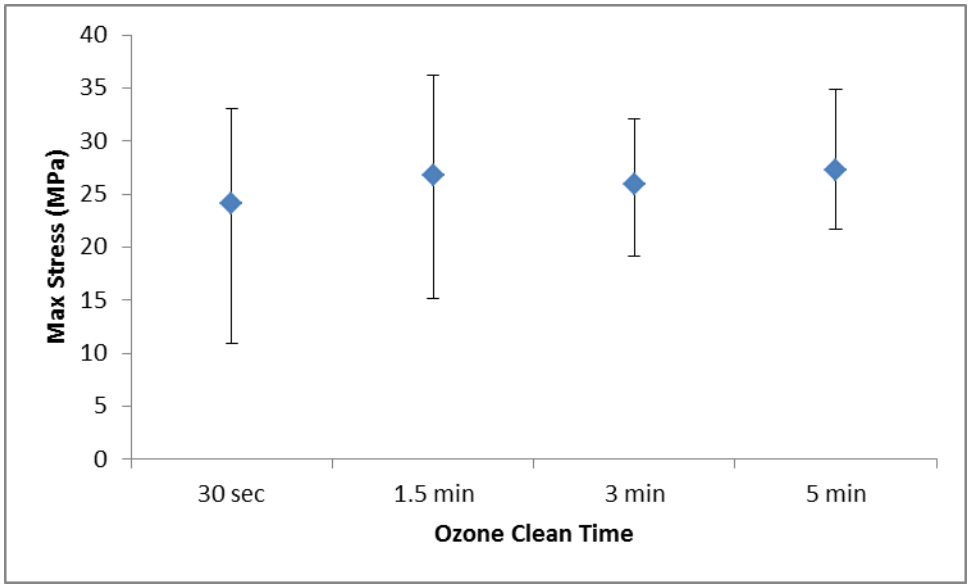

Figure 30: Ozone clean shear results

The ozone clean was beneficial for adhesion strength. Compared to the results presented in Figure 30, the ozone clean treatment improves the shear strength by 40% in general. However, the contact angle measurements in Table 5 for the ozone clean indicate that the clean did not benefit with clean time beyond 1.5 min. Also, there was a tighter grouping for 3 and 5 min ozone clean, but the maximum force was observed in the 1.5 min clean samples. Visually the interface was the primary failure location as it was for the non-thermally treated samples in the first study. There were a few areas with remaining silver as shown in Figure 31.

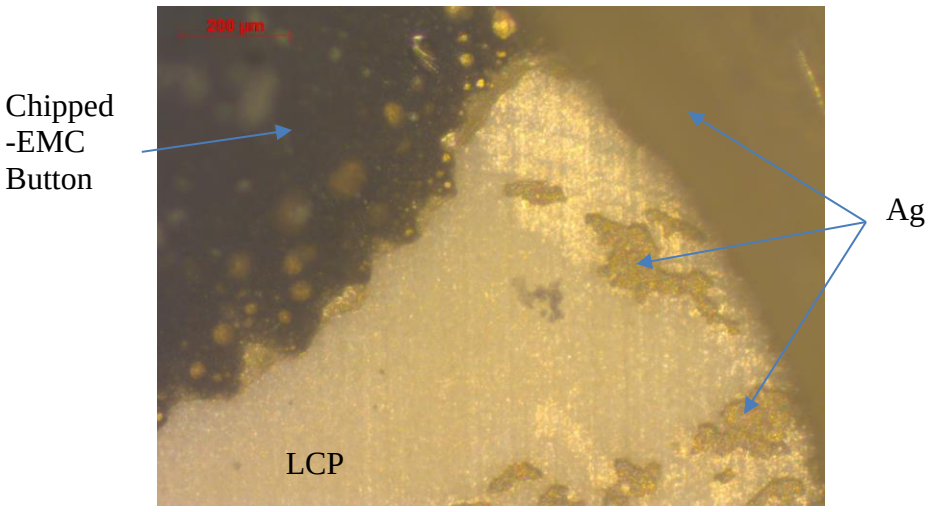

Figure 31: Chipped EMC Button on the Ag/LCP sample after shear testing

1.13 Control study with material set 2: NovaCentrix® Metalon® JS-B25P Ag ink and Novele™ IJ-220 Polyethylene terephthalate (PET) substrate

For this study, the button shear test was examined for a different material set, the novacentrix ink and PET substrate. The XYZtec™ Condor Sigma was configured for the zone shear paddle attachment, and the shear testing is done at three different rates: 1000 µm/s, 100 µm/s and 16.7 µm/s rates. As before, the load at which the button was sheared off was divided by the area of the button to obtain the average shear strength. The error bars in Figure 32 represent the maximum and minimum of the test results for the sample type listed.

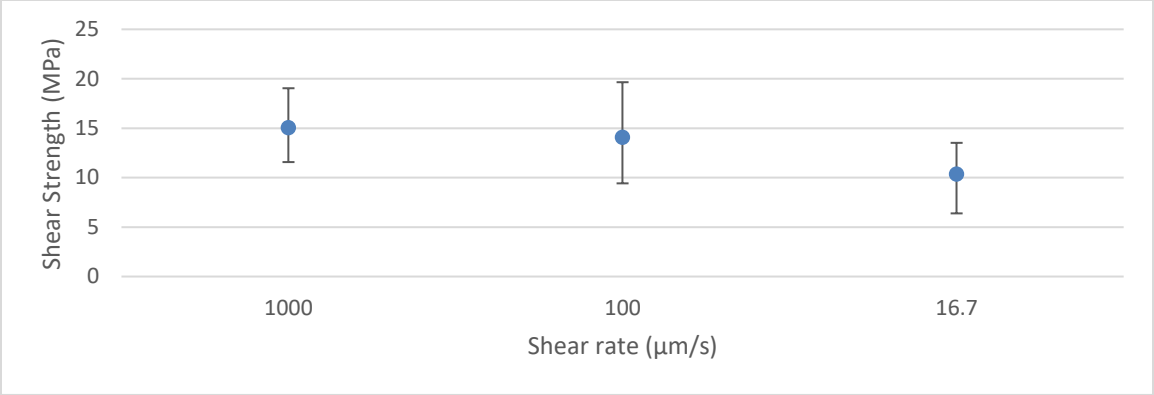

Figure 32 Shear strength for the material set 2 at different shear rates

In Figure 32 the higher shear rates, 1000 and 100 µm/s, gave a higher shear strength compared to the 16.7 µm/s. This trend was similar to the trend seen in material set 1 under control conditions (Figure 24). Literature [34] also indicated that faster shear rates would give clearer understanding for the fracture.

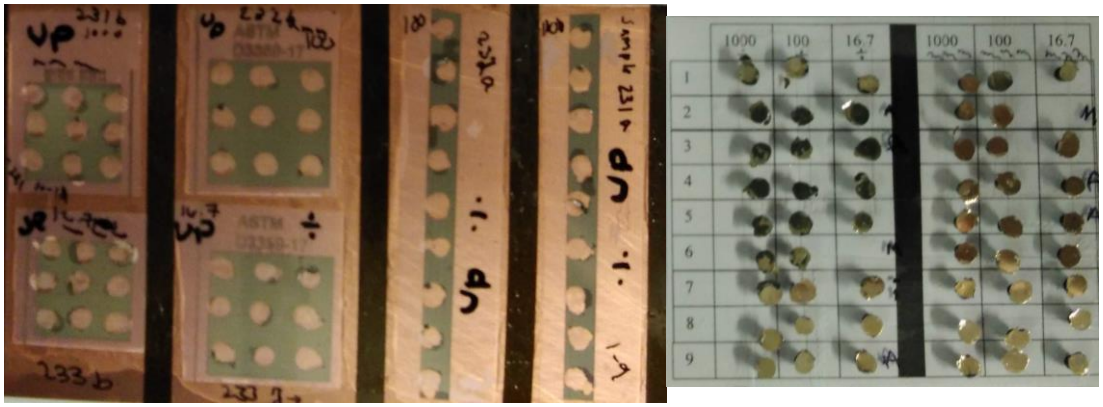

Figure 33: Button shear sample (a) substrate side on Cu FR4 carrier and (b) the bottom of the button for the tests

When examining the surface, a clear distinction of the Ag where the button was is shown on the substrate in Figure 33. On closer examination of the interface with a microscope in Figure 34, residue silver remained on the slowest rate, 16.7 um/s, samples.

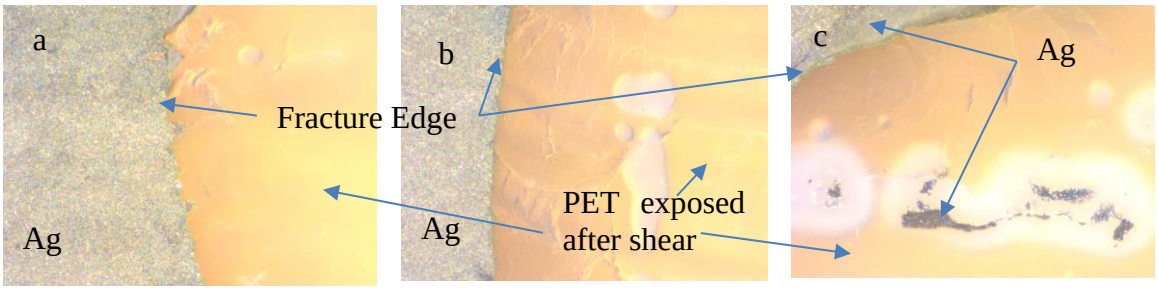

Figure 34: Microscope image of the board side (a) 1000 um/s (b) 100 um/s and (c) 16.7 um/s at the same magnification

1.13.1 Shear test discussion and implications

Based on the experiments, it is seen that ozone treatment is helpful to enhance the adhesion of the printed ink to the LCP substrate. However, treatment beyond 1.5 minutes may not be helpful to further increase the adhesion strength. Thermal annealing of the ink does not appear to help. It appears that the thermal annealing makes the ink layers cohesively break, rather than delaminate from the substrate, and at a lower force compared to no-thermal-treatment samples. Material set one (18 MPa) is only slightly stronger in shear compared to material set two (15 MPa) when no pre-treatment is performed on the substrate.

DEVELOPMENT OF PEEL TEST

For the adhesion testing, the peel test was explored for a different mode of fracture. Peel tests have been applied on various thin-film structures including copper in electronic packaging. These plated copper and foil copper films are easier to peel due to (1) being a thicker film and (2) continuous. The printed ink is a challenge due to the porous structure of the silver particles sintered together in thin printed layers. Thus, it was not easy to peel the ink directly away from the surface of the substrate. Alternatively, the flexible substrate could be peeled from the ink: the flexible substrate with the ink side down is adhered to a stiff carrier structure, and then the flexible substrate is peeled away. This approach provided the basis for the first modified peel test: "Method 1: Flexible Substrate Peel Test" as illustrated in Figure 35. As the polymer flexible substrates are viscoelastic and/or hyperelastic, the substrate could significantly deform under applied force. Thus, the total energy measured includes both elastic and inelastic energy as well as the energy to delaminate the substrate from the ink. In view of this, a second method was developed so a substitute material was used to peel the ink from the flexible substrate, as illustrated in Figure 35. In this "Method 2: Substitute Structure Peel Test," the flexible substrate was first adhered to a carrier structure with the ink on the topside. A substitute structure was then adhered to the ink. If the adhesion of the ink to the substitute structure was stronger, the ink would delaminate from the flexible substrate as the substitute structure is peeled away. By selecting an appropriate substitute structure and adhesive material, less energy is lost to plastic deformation of the peeled structure. Thus, a higher proportion of the measured energy is from peeling the intended ink and flexible substrate interface.

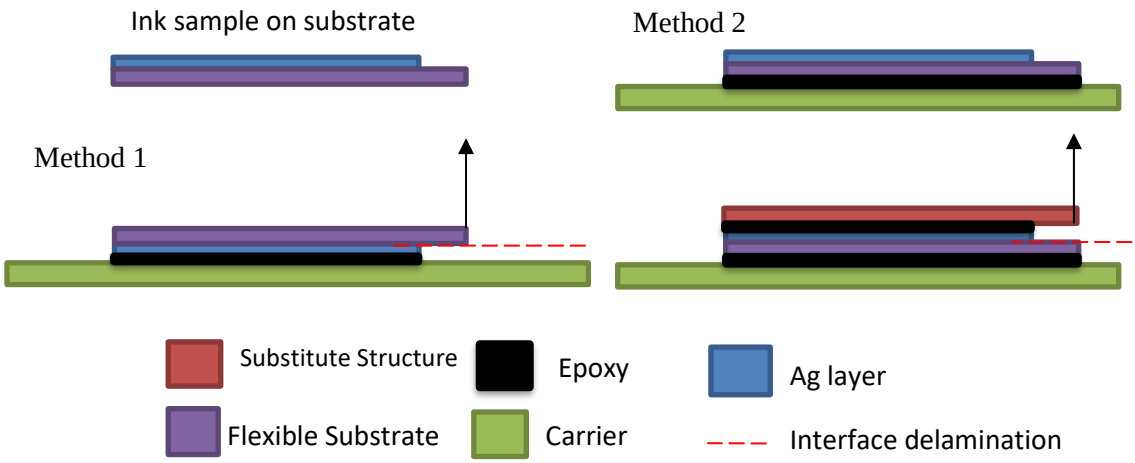

Figure 35: Schematic for the methods used for determining the adhesion strength

The red line in Figure 35 indicates the desired delamination location. . For the first method, the Ag ink was left on the carrier substrate, while the flexible substrate was peeled off. For the second method, the silver ink and the substitute layer were peeled off from the flexible substrate as shown in Figure 36.

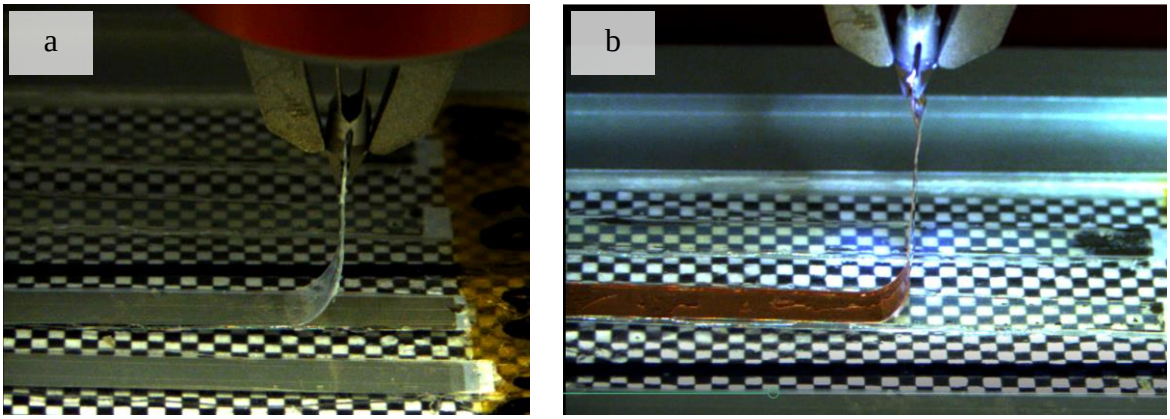

Figure 36: Comparison of the pull off fracture location for the two different methodologies (a) Method 1: flexible substrate peel test (b) Method 2: substitute structure peel test

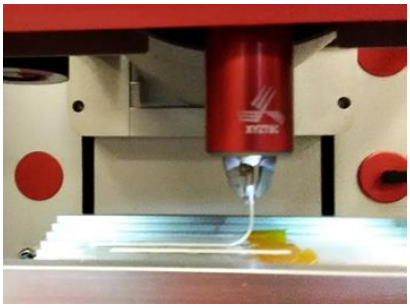

Figure 37: XYZTEC™ tweezer peeling sample in vice

For the peel test, the XYZTEC™ adhesion test tool was utilized with the tweezer head as shown in Figure 37. The head and the stage were programed to move at the same rate. The intention for these experiments on the XYZTEC™ adhesion test tool was to investigate the interface adhesion between the two material sets. This chapter will look at the sample preparation, and then will discuss the experiments and results.

1.14 Method 1: flexible substrate peel test

The peel test with the Method 1 configuration gives a simple test set up that is similar to the current electronic packaging adhesion test (IPC-TM-650 Method 2.4.8.1). necessarily being continuous and not easily peel-able by itself, the flexible substrate was peeled off instead.

1.14.1 Sample preparation and fixturing

The material sample sets were taken as-is for the processed ink film on the flexible substrate, and the sets underwent the sample preparation in Figure 38. First, the samples were cut into strips. Next the strips were adhered to the carrier structure with the ink facedown using a commercially available epoxy. This epoxy sets at room temperature and

fully cures in an hour. The room-temperature cure alleviates any concerns of microstructure change in the conductive ink compared to epoxy cured at higher temperatures in an oven. After the epoxy was cured, a blade was used to scribe along the sides of the strip to ensure detachment of the epoxy on the sides. If there was any epoxy along the side, it would influence the adhesion data. The carrier was needed to hold the flexible substrate in the XYZTEC^{TM} vice grip.

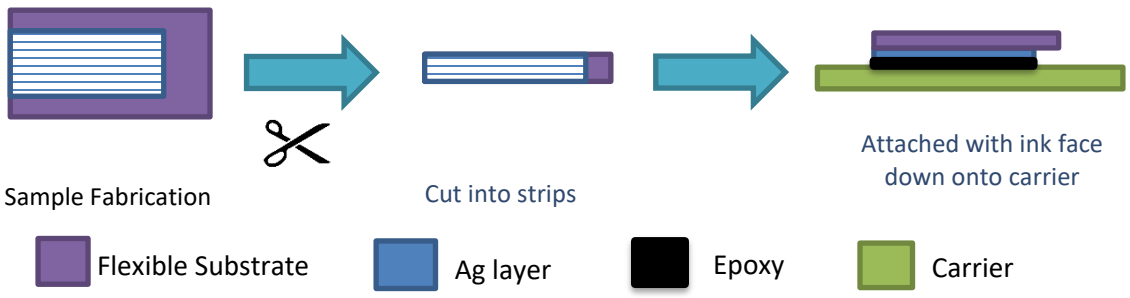

Figure 38: Method 1 sample preparation

Once fixtured, the tweezer head was set to pull the flexible substrate away from the ink and the carrier. The entire peel test was recorded, and the video clip was useful to provide additional insight into the measured displacement and load data.

1.14.2 Details of experiments and images

For Method 1 as shown in Figure 39, two different carrier materials are used: (1) a 2 mm-thick clear polycarbonate sheet and (2) Cu-clad FR4 board. The ink printed on a flexible substrate was adhered to the polycarbonate carrier with an epoxy, as illustrated in Figure 39. Additionally, a checker pattern was adhered to the underside of the clear polycarbonate carrier. The checker pattern provided a measurable reference for the crack front location in the video recording, since each square's side was 1 mm in length.

Although the polycarbonate substrate served as a good carrier for weaker ink films, the epoxy did not adhere well enough to polycarbonate when the ink's adhesion to the flexible substrate was improved. Therefore, a different carrier substrate, Cu-clad FR4, was used. Adhesion to Cu-clad FR4 was strong enough to ensure that delamination occurred at the interface of ink and flexible substrate. As the opaque Cu-clad FR4 did not provide an opportunity to use the checkered board, the delamination location was determined through the video alone. Both carrier materials were roughened by sandpaper (120 grit) to help the epoxy adhere to it.

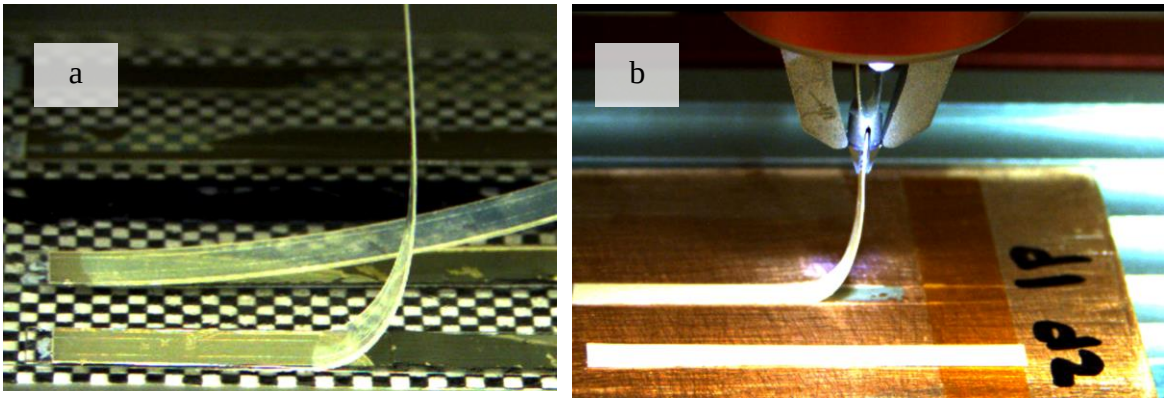

Figure 39: Carrier images (a) clear polycarbonate with attached grid and (b) Cu clad FR4 board

A starter crack was initiated by pulling back the strip. If needed, a razor was used to aid with delamination at the desired interface. Next, the sample was placed in the vice, and a handheld pair of tweezers placed the flexible substrate strip into the system's tweezer system.

1.14.3 Peel test experimental data

The experiments were conducted for two material sets. . The first material set was the Suntronic™ EMD 5730 and Rogers Corporation ULTRALAM® 3850HT substrate. The second set was NovaCentrix® Metalon ® JS-B25P Ag ink and Novele ™ IJ-220 PET substrate.

1.14.3.1 Method 1 on material set 1: Suntronic™ EMD 5730 ink on Rogers Corporation ULTRALAM® 3850HT LCP

Different rates, strip widths and carriers were used to demonstrate the applicability of the peel test and determine the peel force. Table 8 provides the peel tests that were conducted using Method 1 on the first material set– Suntronic ink on Rogers LCP substrate.

Table 8: Method 1 on material set 1 (Suntronic ink on Rogers LCP substrate) test descriptions

Test Case	Number of samples	Material Set	Carrier	Width (mm)	Rate (mm/s)	Peel distance (mm)	Average measured peel force (N/m)
1	6	1	polycarbonate	4	50.0	25	~100
2a	3	1	polycarbonate	1	1.0	15	~200
2b	3	1	polycarbonate	3	1.0	25	~170
3	1	1	CuClad FR4	3	1.0	25	~200
4a	7	1	CuClad FR4	3	0.1	45	~445
4b	8	1	CuClad FR4	3	1.0	45	~440

Between the first case of 6 samples (Figure 40) and the second case (2a and 2b in Table 8) of 6 samples (Figure 41), there is an increase of peel force by 100 N/m between 2a and 2b. The second case of samples (2a and 2b) were cleaned better and this additional processing resulted in the increase in adhesion peel force. Between the second case and the third case of material sample set 1, there was no change in adhesion peel force. This

indicated the adhesion peel force was governed by the materials of interest and not the underlying carrier substrate. The result is consistent with the expectation, as long the failure occurs at the same interface of interest. Also, it shows that the results are marginally affected by the strip width.

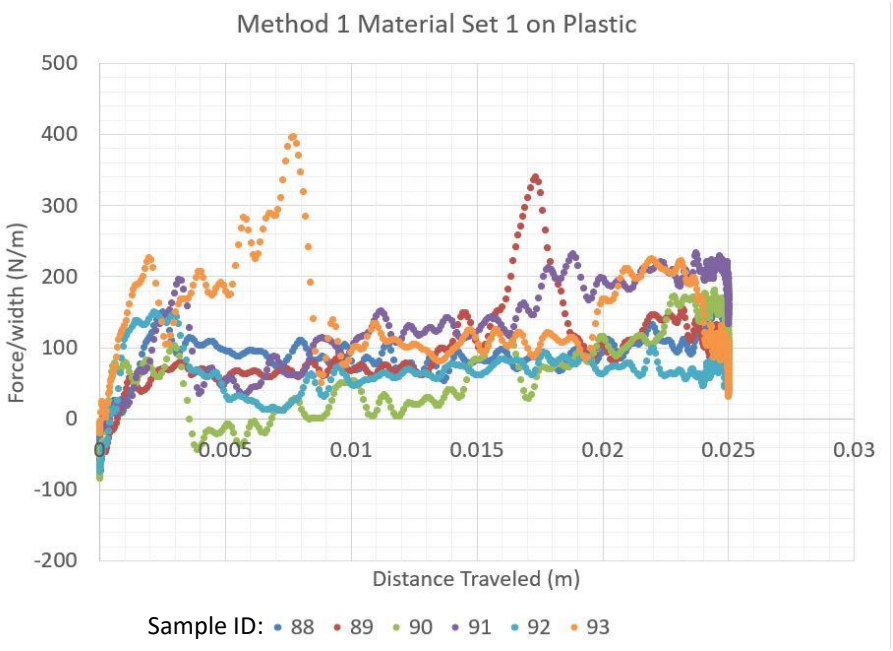

Figure 40: Peel test Method 1 on material set 1 on a plastic carrier – 4 mm wide samples (Case 1)

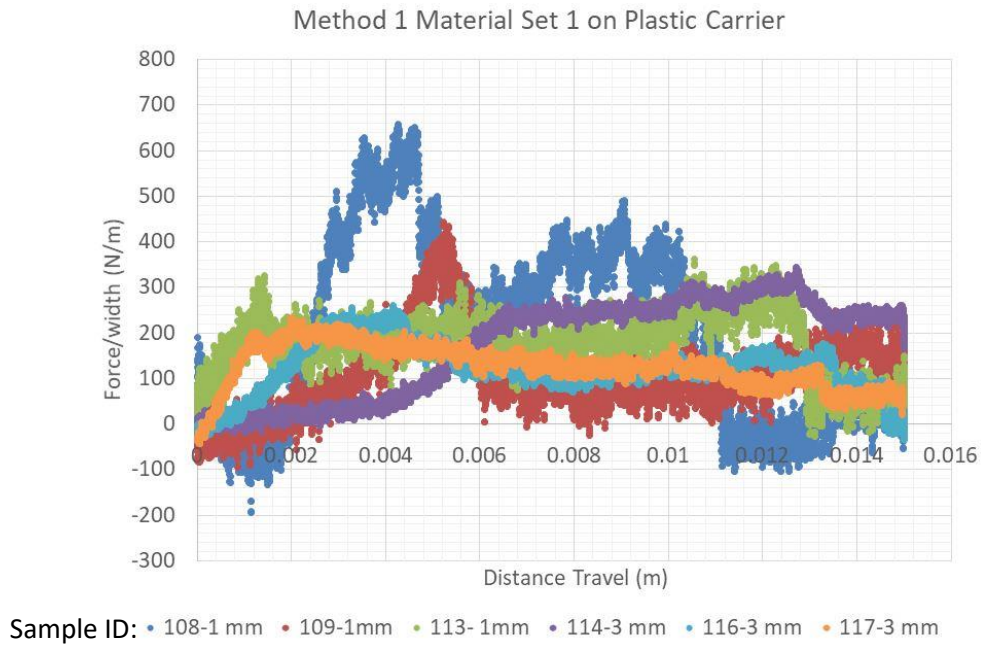

Figure 41: Peel test Method 1 material set 1 on plastic carrier – 1- and 3-mm wide samples (Cases 2a and 2b)

It was expected that the peel force would remain constant along the entire peel length. However, in actual experiments, the peel force would oscillate, although the overall magnitude was roughly 200 N/m for the last set of samples. The up and down change in the peel force can be attributed to the type of failure that occurs. Along the peel length, it was not uncommon that the ink would completely strip off from the LCP substrate, or partially strip off from the LCP substrate, or strip off from the adhesive; and thus, depending on the type of failure, the adhesion force will change along the peel length.

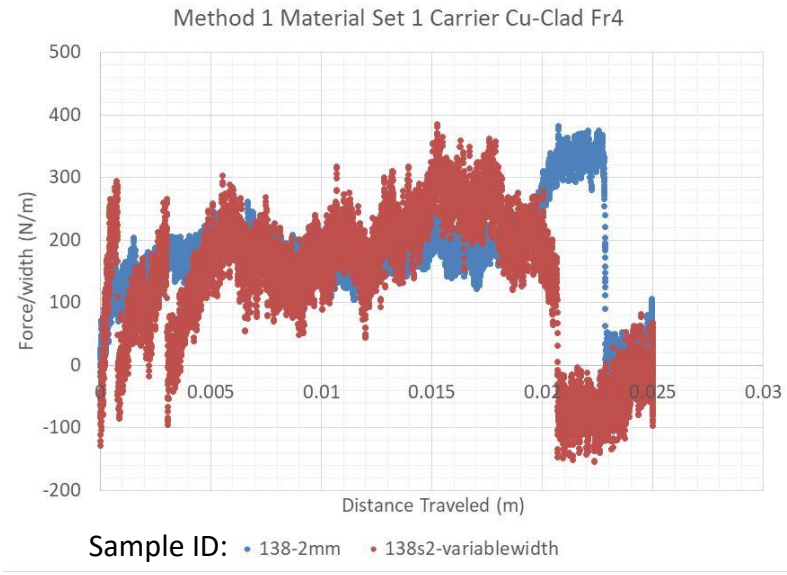

Figure 42: Peel test Method 1 on material set 1 on carrier Cu-clad- FR4 – 3 mm wide sample (Case 3)

For the fourth case, the epoxy was spread more evenly by the addition of tape tracks between samples as seen in Figure 43. The ink samples came as-is from different print batches and were cut into the strip width. Then samples were randomly selected to be glued onto the carrier.

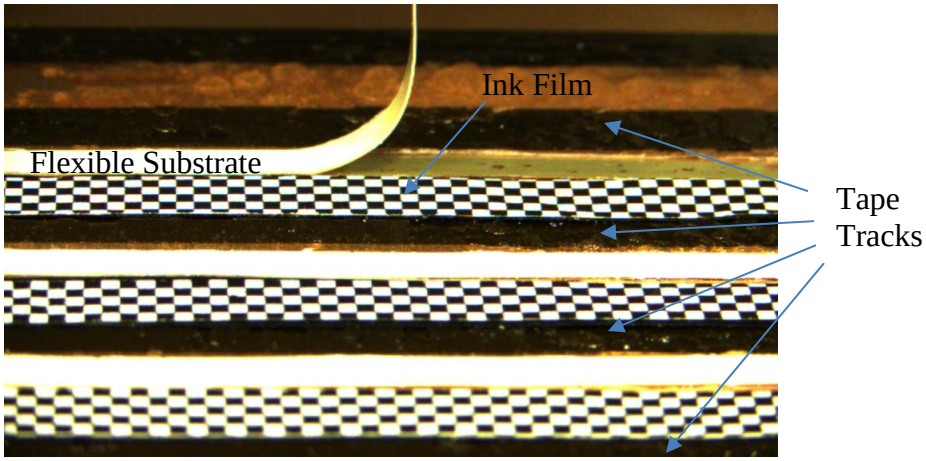

Figure 43: Peel test Method 1 on material set 1 on carrier Cu-clad- FR4 – 3 mm wide sample - additional tape (dark brown) along the sample sides to keep the epoxy deposition uniform.

For a peel test done at 0.1 mm/s (Case 4a), the desired profile was obtained with a constant peel force as demonstrated in Figure 44. Figure 45 contains the data (red) collected from a peel test with a rate of 1.0 mm/s (Case 4b), which was noisy due to the interface jump of the crack. A filter on the data reduced the noise for a better understanding of the data with a Python script. The rolling filter, also known as moving-average filter, only considered the influence of neighboring points for the average, and in turn the (blue) filtered data was still noisy. The cumulative filter considered the average of all the previous data points in the data set. When the cumulative filter was applied to the across the whole data set (green), the initial pulling of the peel arm artificially lowered the average. To get a more accurate estimate, the data was truncated to not include the loading for the cumulative filter (yellow).

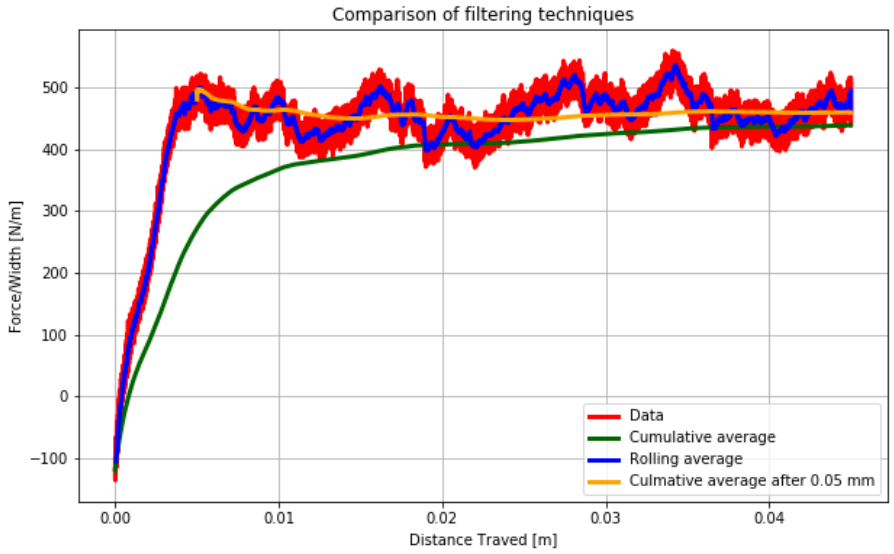

Figure 44: Peel test Method 1 on material set 1 on carrier Cu-clad- FR4 – 3 mm wide sample (Case 4a). Sample ran at 0.1 mm/s with different filters applied to examine the best fit

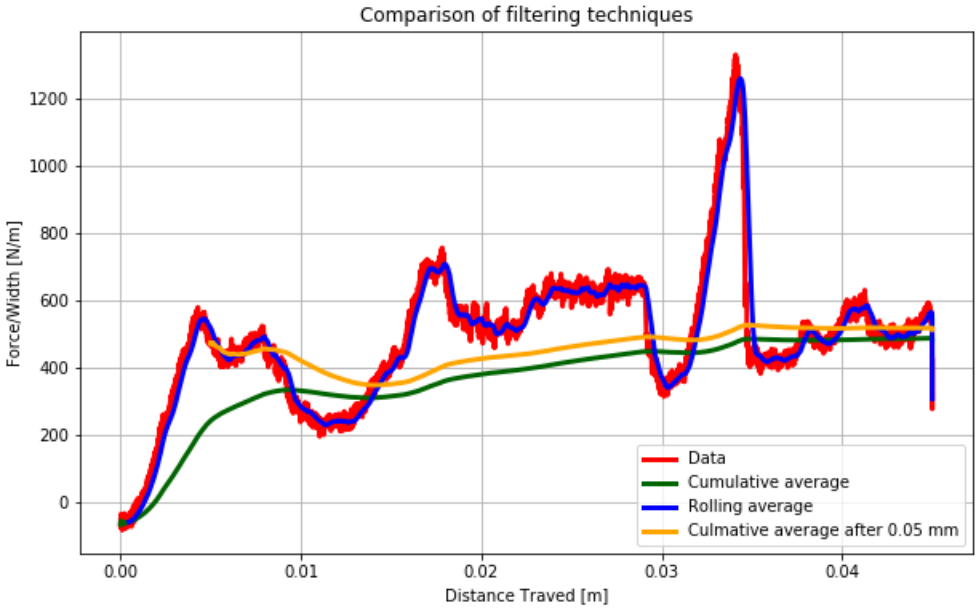

Figure 45: Peel test Method 1 material set 1 on carrier Cu-clad- FR4 – 3 mm wide sample (Case 4b). Sample ran at 1.0 mm/s with different filters applied to examine the best fit

The peel strength was taken from the mean of the cumulative fit for each sample. For the samples peeled at a rate of 0.1 mm/s (Case 4a), Figure 46 details the cumulative fit data's max (orange), min (grey) and mean (blue) with standard deviation error. . Figure 47 is the corresponding information for the samples peeled at a rate of 1.0 mm/s (Case 4b). The later samples (Case 4a: 6 and 7) in Figure 45 did not have the LCP scribed well on the side, and in turn, the LCP ripping caused fluctuations in the data and larger standard deviation. The value reported in Table 8 is the average of all the samples for a given case.

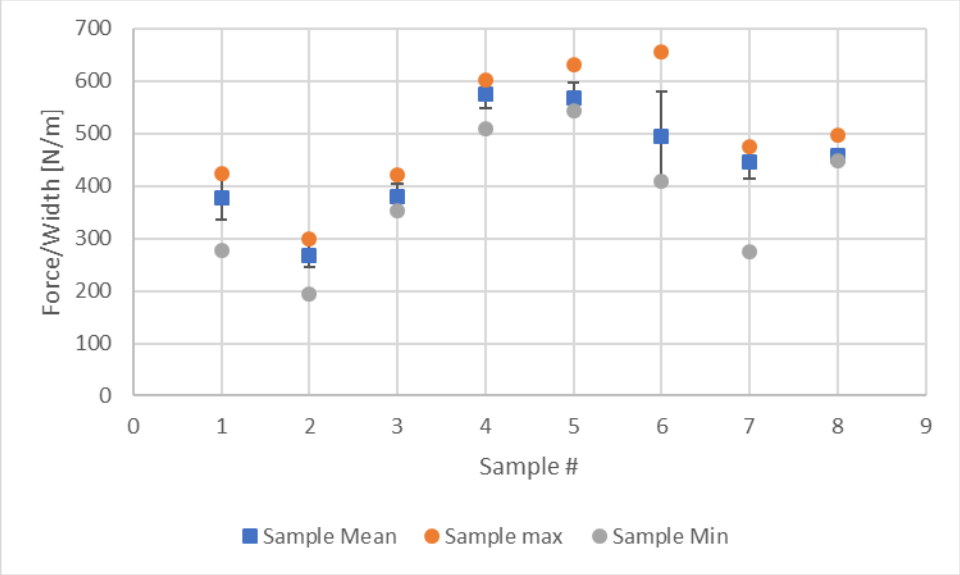

Figure 46: Peel test Method 1 on material set 1 on carrier Cu-clad- FR4 – 3 mm wide sample (Case 4a). Samples with peel rate of 0.1 mm/s cumulative fit descriptions with the sample mean in blue, standard deviation error bars, max data point in orange and min data point in grey

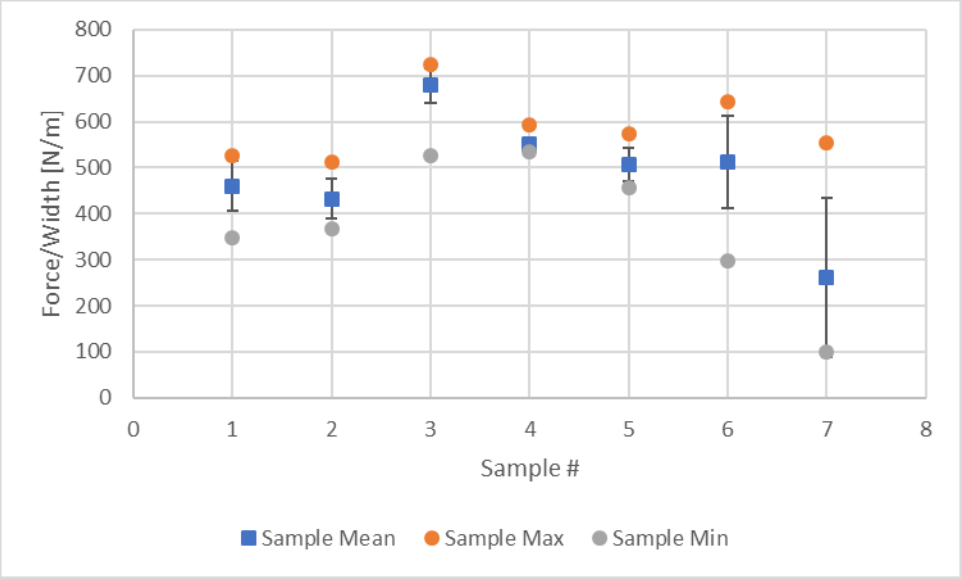

Figure 47: Peel test Method 1 on material set 1 on carrier Cu-clad- FR4 – 3 mm wide sample (Case 4b). Samples with rate at 1.0 mm/s cumulative fit descriptions of the average mean in blue, standard deviation error bars, max data point in orange and min data point in grey

1.14.3.2 Peel test Method 1 on material set 2: NovaCentrix® Metalon® JS-B25P Ag ink and Novele™ IJ-220 Polyethylene Terephthalate (PET) substrate

For material set 2 (NovaCentrix® Metalon ® JS-B25P Ag ink and Novele ™ IJ-220 PET substrate), the carrier material used was plastic. In Figure 48, the results are shown for 3 mm wide strips with the air-dried samples for Method 1. Seven samples were peeled 45 mm, and the average peel force was about 100 N/m. In addition to air-dried ink, the ink was also oven-cured and pulse-forge cured. The thermal oven cure was done at 90 ºC for one hour, while pulse cure was done at max intensity for 30 seconds. The Method 1 peel test experimental data for the cured as well as pulse-forged samples are shown in Figure 49. Two samples for each treatment were tested, and the average peel force was about 150 N/m.

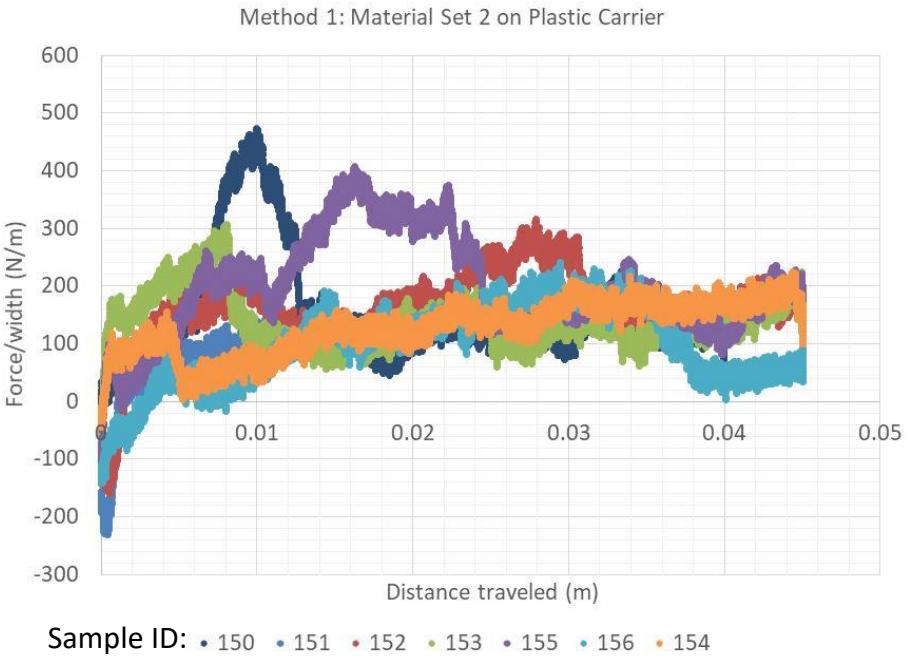

Figure 48: Peel test Method 1 on material set 2 on plastic carrier – 3 mm wide sample air dried

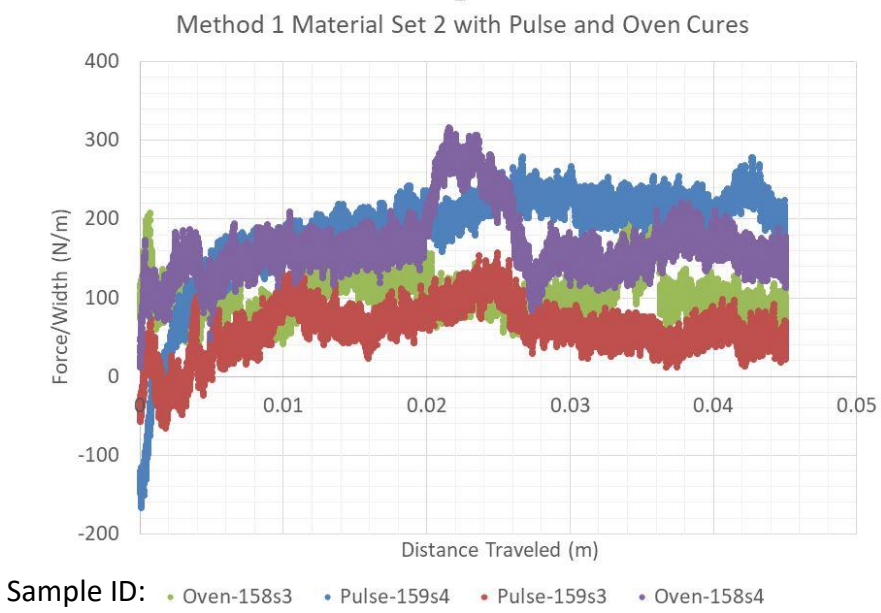

Figure 49: Peel test Method 1 on material set 2 on plastic carrier – 3 mm wide sample oven or pulse cured

For material set 2 in Method 1 configuration, all the strips peeled at the ink and PET interface; however as indicated in Figure 50, there were two distinct surfaces revealed: (1) dull silver and (2) shiny silver. Higher force/width is seen on the graphs for the samples in the distance of the peel which the change of dull to shiny. Dull surface indicates that the silver ink was still adhered to the epoxy, and the PET substrate had completely peeled off from silver ink. This is the desired outcome. Shiny surface indicates that part of the porous film had peeled off with the PET substrate, and thus, the failure had occurred at the silver and epoxy interface. This type of failure would show higher value of peel force/length. In general, as seen in the images, most of the failures were in the interface of silver ink and PET substrate.

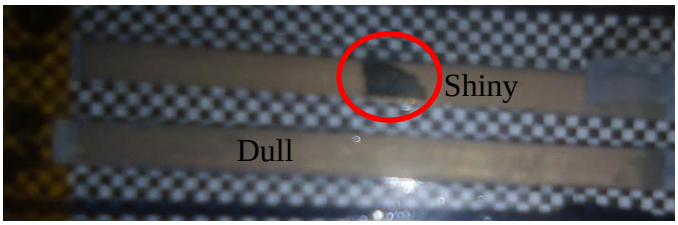

Figure 50: Peel test Method 1 on material set 2 on plastic carrier – 3 mm wide sample after test

1.15 Method 2: substitute structure peel test

The peel test with the Method 2 configuration was meant to be more consistent across material sets. A substitute backing structure was peeled off with the ink layer from the flexible substrate.

1.15.1 Sample preparation and fixturing

For Method 2, the material sample sets were taken as is and underwent the sample preparation in Figure 51. First, the samples were cut into strips. Next the strips were adhered to the carrier with the ink face up using a commercially available epoxy. The epoxy set at room temperature and fully cured in an hour. After the cure, a substitute structure was added to the stack with the same type of epoxy. After the second epoxy was cured, a blade was used to scribe along the sides of the strip to ensure detachment of the epoxy on the sides. If there was epoxy remaining on the side, it would influence the measurement.

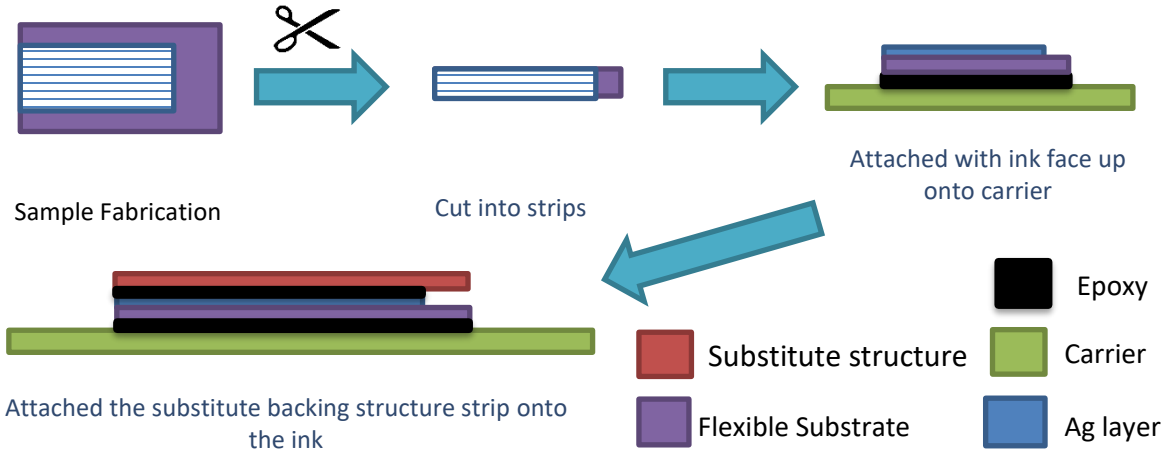

Figure 51: Sample preparation for Method 2

1.15.2 Details of experiments and images

For Method 2 as shown in Figure 52, two substitute backing substitute structure are explored: foil and Cu-cladded fr-4 flexible substrate. Since in Method 2 the ink needed to adhere to the substitute structure, it was the focus. The carrier material is roughened by sandpaper (120 grit) to help the epoxy adhere to it.

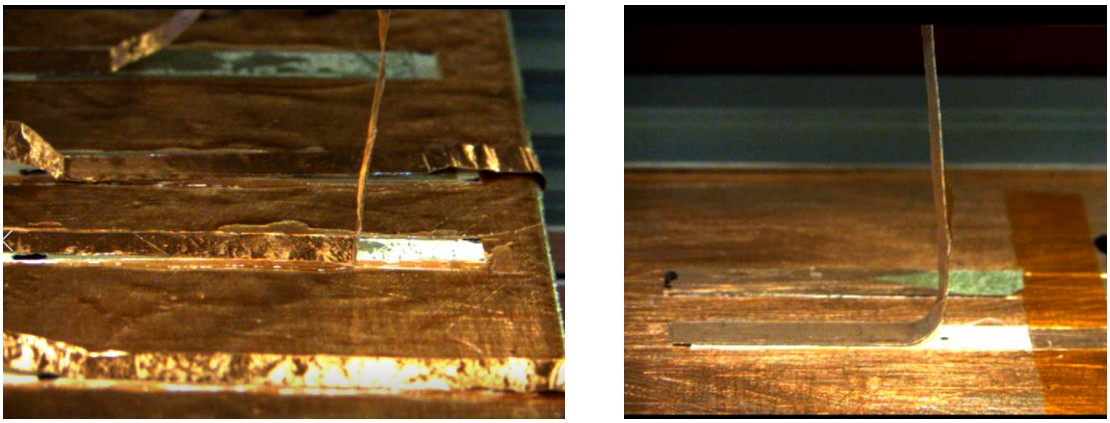

Figure 52: Method 2 with different substitute backing layers (a) Cu foil and (b) Cu-clad Fr-4 flexible substrate

Before the sample was placed in the vice grip for 90° pull, a starter crack was initiated by pulling back the strip to initiate the delamination. If needed, a razor was used to help delamination at the intended layers. Once the sample was placed in the vice, a manual pair of tweezers placed the strip into the system's tweezer. The rate of pull was set to be 1 mm per second on the tool. Then the stage (x-direction) and the tweezer (z-direction) move at the same rate. During the experiments, a video was taken to observe the substitute structure's shaped during the peel test and crack extension distance.

1.15.3 Data from the experiments

The experiments are discussed by material sets. The first material set was the Suntronic™ EMD 5730 and Rogers Corporation ULTRALAM® 3850HT substrate. The second set was NovaCentrix® Metalon ® JS-B25P Ag ink and Novele ™ IJ-220 PET substrate.

1.15.3.1 Method 2 on material set 1: Suntronic™ EMD 5730 ink on Rogers Corporation ULTRALAM® 3850HT LCP

Different process runs were attempted to determine the peel strength and demonstrate the applicability of the developed peel test. The following list provides the peel tests that were conducted using Method 2 and is also summarized in Table 9.

1) Material set 1- Suntronic™ EMD 5730 and Rogers Corporation ULTRALAM® 3850HT substrate with a substitute layer composed of flexible Cu-clad FR-4. The Cu-clad flexible board was composed of a core FR-4 sheet with a 100 μm thickness and Cu foil on both faces which are

25.4 μm thick. The first set is shown in Figure 53. Three different strip results were peeled. The 124v2 triangle was a substitute structure that was cut into a triangle. The width calculation was calculated based on the crack distance using trig. The strips were peeled a distance of 45 mm and the average peel force is 125 N/mm.

2) Material set 1 Suntronic™ EMD 5730 and Rogers Corporation ULTRALAM® 3850HT substrate with a substitute structure composed of flexible Cu-clad FR-4. A second printed set is shown Figure 54, and these strips were only peeled for 25 mm at 1000 mm/s. The average peel force measured for the second print set was 400 N/m.
3) Material set 1- Suntronic™ EMD 5730 and Rogers Corporation ULTRALAM® 3850HT substrate with a substitute structure composed of a Cu foil in 25. 4 μm (1 mil). Seven test results are shown in Figure 55. The results did not give a clear indication of the peel strength. The force/width ranged from 200-800 N/m.

For the first and second cases, there was an increase in the peel force similar to the Method 1 results. This was due to the better cleaning and processing of the second case of samples that resulted in the increase in adhesion peel force. The results were not as constant for the peel test, and this was attributed to the ink not always peeling cleanly away from the LCP substrate.

Table 9: Method 2 on material set 1 (Suntronic ink on Rogers LCP substrate) test descriptions

Test Case	Number of Samples	Material Set	Carrier	Substitute Structure	Width (mm)	Rate (mm/s)	Peel distance (mm)	Average measured peel force (N/m)
1a	2	1	CuClad FR4	CuClad FR4	3	1.0	45	125
1b	1	1	CuClad FR4	CuClad FR4	variable	1.0	45	
2	2	1	CuClad FR4	CuClad FR4	3	1.0	25	~400
3	7	1	CuClad FR4	CuClad FR4	3	1.0	20	200-800

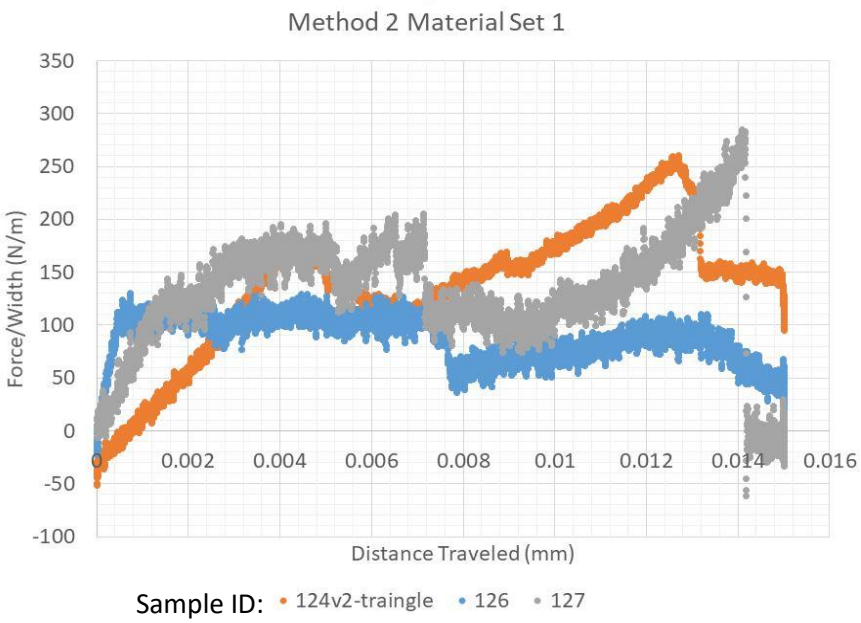

Figure 53: Method 2 on material Set 1 with Cu-clad-FR4 flexible substitute structure (Case 1a & 1b)

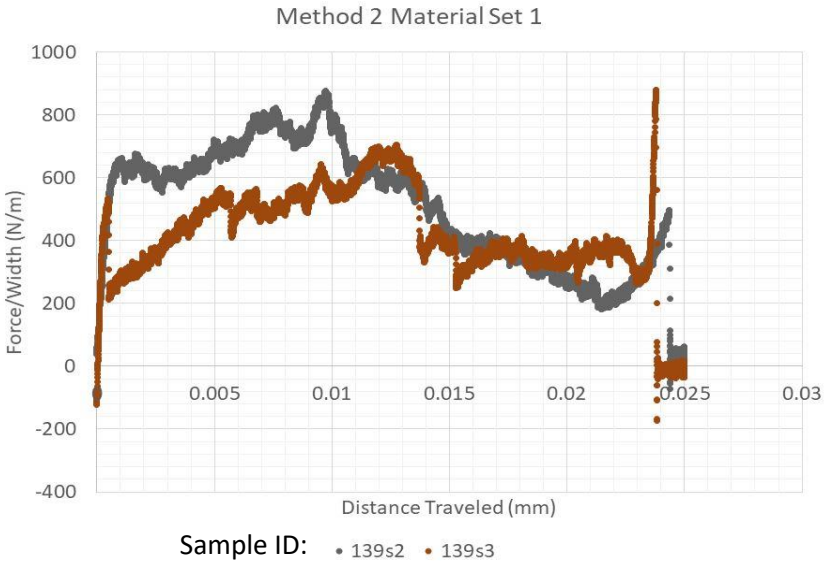

Figure 54: Method 2 on material set 1 with Cu-clad-FR4 flexible substitute structure (Case 2)

.

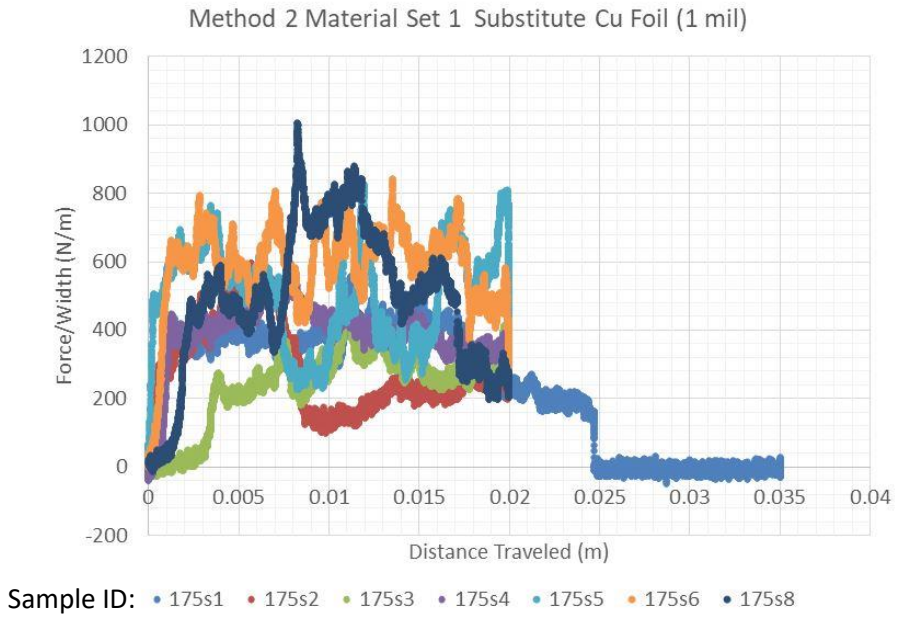

Figure 55: Method 2 on material set 1 with 1 mil Cu foil as the substitute structure (Case 3)

To confirm that the correct interface is delaminating for the Method 2 on the first material set, SEM imaging is done on the Cu substitute structure in Figure 56, and EDS is performed on the LCP side of the peeled off section Figure 57.

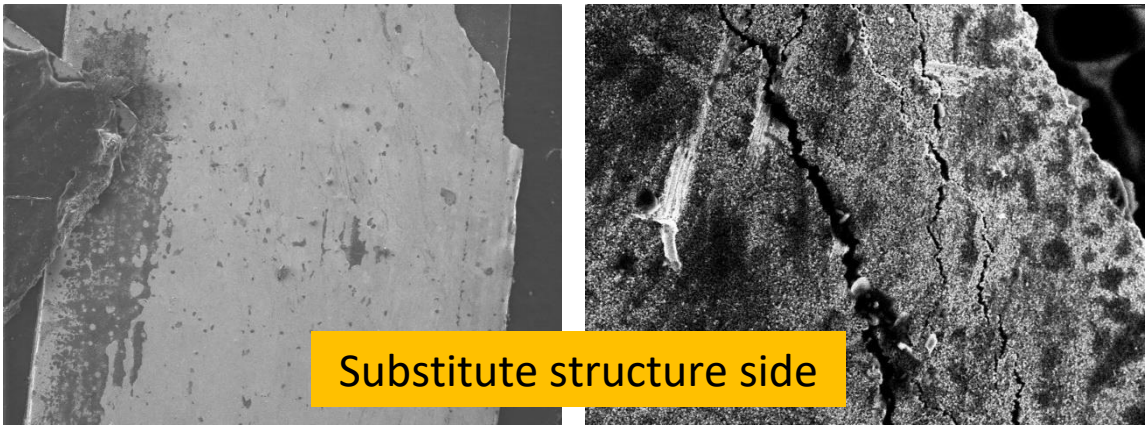

Figure 56: SEM imaging of the substitute structure with the ink side showing

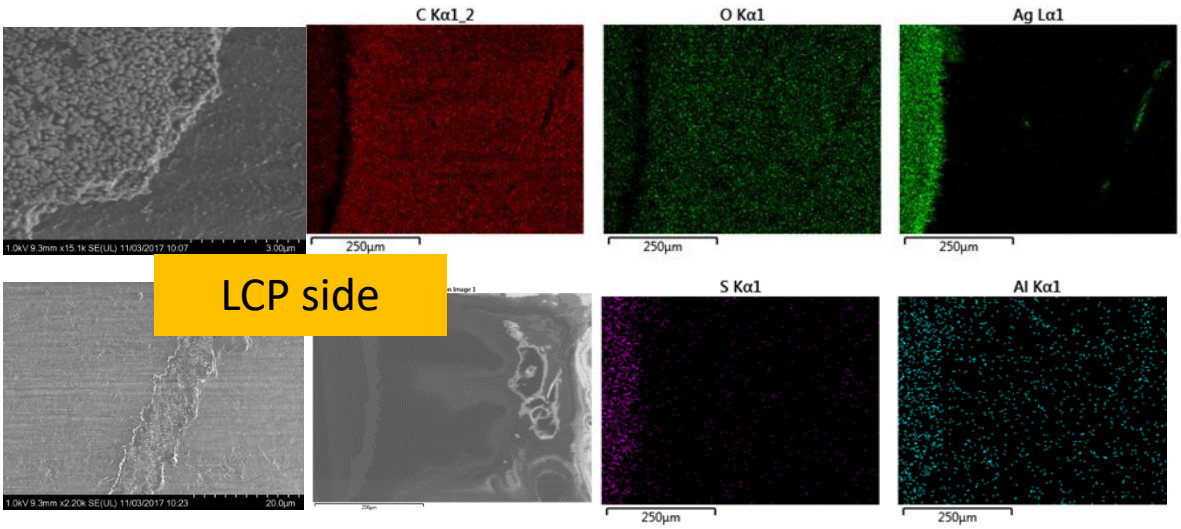

Figure 57: SEM images and EDS performed on the edge of a peeled off section

1.15.3.2 Method 1 on material set 2: NovaCentrix® Metalon® JS-B25P Ag ink and Novele™ IJ-220 Polyethylene Terephthalate (PET) substrate

For material set 2 (NovaCentrix® Metalon ® JS-B25P Ag ink and Novele ™ IJ-220 PET substrate), the substitute structure is a Cu foil that is 76.2 µm (3 mil) thick. In Figure 58, the results are shown for 3 mm wide strips with the air-dried samples for Method 2. Six samples were tested, and the average peel force results were convoluted Peeling was done

through a distance of about 45 mm. In addition to air-dried ink, the ink was also oven-cured as well as pulse-forge cured. The thermal oven cure was done at 90 ^{o}C for one hour, while pulse cure was done at full intensity for 30 seconds. The Method 2 peel test experimental data for the cured as well as pulse-forged samples are shown in Figure 59. Two samples for each treatment were tested, and the average peel force was roughly 200 N/m. The peeling was carried out through a distance of about 45 mm.

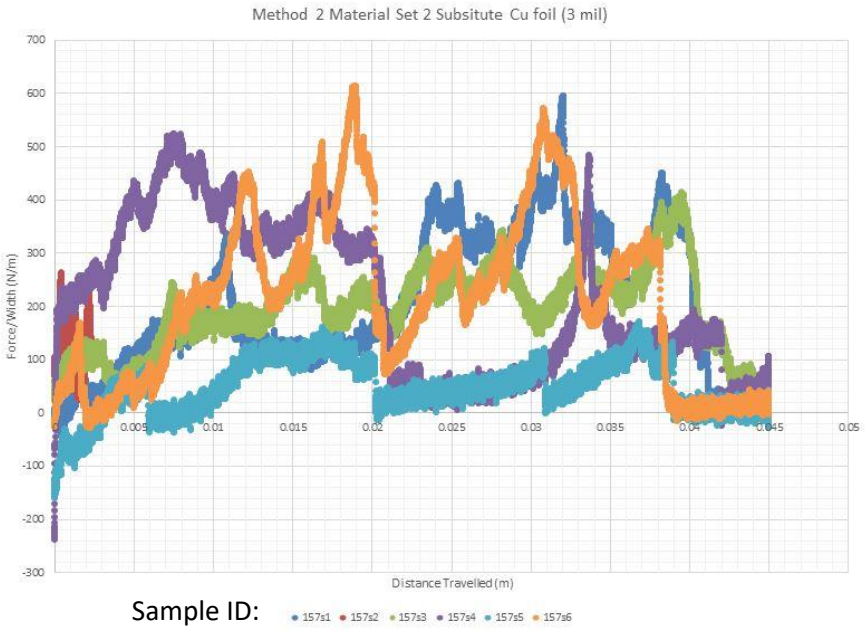

Figure 58: Method 2 material set 2 air dried with Cu foil substitute layer

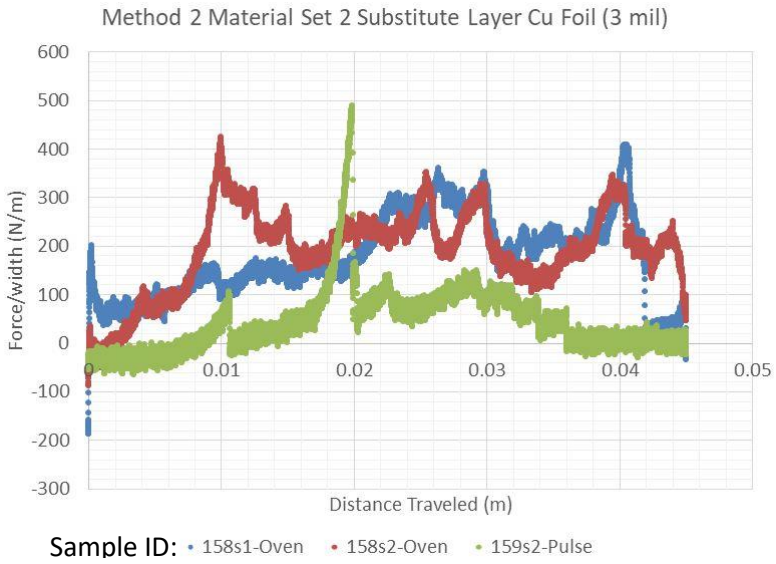

Figure 59: Method 2 material set 2 not air dried with Cu foil substitute layer

For the second set of materials in the 90° peel test, the ink is contained in a porous film, and it is these films' adhesion strength which dominates the results. In the cross-section of Figure 60, there are two thin film layers on top of the PET. These films are assumed to be the mesoporous film mentioned in the NovaCentrix® literature on the Novele ™ IJ-220 PET. It also explains the distinct sections of the peel seen in Figure 50 for the material set 2.

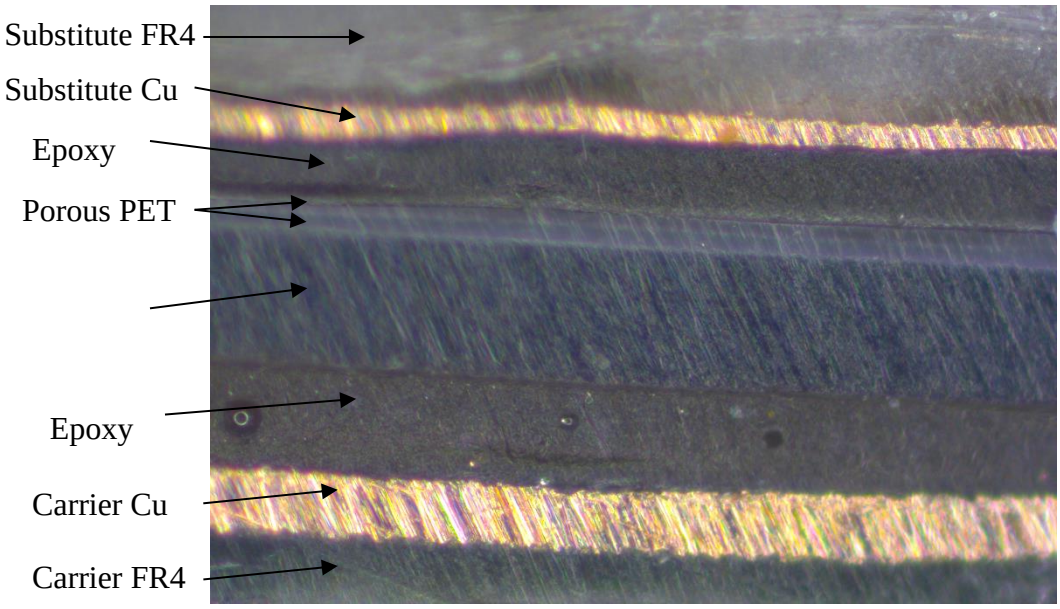

Figure 60: Cross-section of the Method 2 material set 2

1.16 Discussion

In this chapter, two different peel configurations are demonstrated and results examined. Method 1 with the simpler configuration shows more consistence results for both material sets. Method 2 needs further work to make it a more consistent test.

For Method 2, the Cu foil was pursued originally as a better option for the simplicity in the models where only one homogeneous material would be used as the substitute structure. However, the results are not as clear due to the harder handling of the Cu foil and potential plastic deformation of Cu. Between the roughening of the foil surface and cutting the copper to size, the substitute structure was deformed and was not planar during the epoxy adhesion step.

With the substitute structure, there needs to be an account of the load change due to the stiffness of the material. Figure 53 and Figure 54 show the peeling process and the radius of peel that depends on the stiffness of the substitute structure.

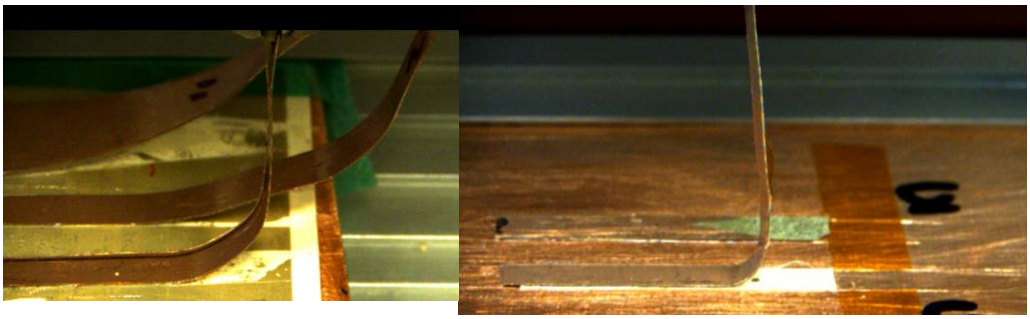

Figure 61 Standardization needed for bending radius of the peel test or monitoring (a) sample 126 (b) sample 139s2

NUMERICAL MODELING

In this chapter, Method 1 peel test was modeled to determine the critical fracture strain energy with relation to the experiment in Chapter 5. Due to the complexity of the material stack up as well as complexity in the constitutive behavior of various materials in the stack, a closed-form analytical solution is not as readily possible, and thus, a finite-element modeling is used in this work to determine the critical fracture strain energy at the interface between the ink and substrate [35].

1.17 Adhesion Modeling Techniques

There are two main approaches to fracture mechanics in determining the fracture energy: stress intensity factor and strain energy release rate [35]. The first approach, stress intensity factor (SIF), has the advantage of calculating what is occurring at the crack front and often characterizes the fracture toughness, K, based on the crack mode [7]. Each of the modes can be described in terms of how loads are applied: Mode I –opening, Mode II – sliding/shearing, and Mode III – tearing. The three modes are illustrated in Figure 62, and Mode I and Mode II are commonly found in many applications.

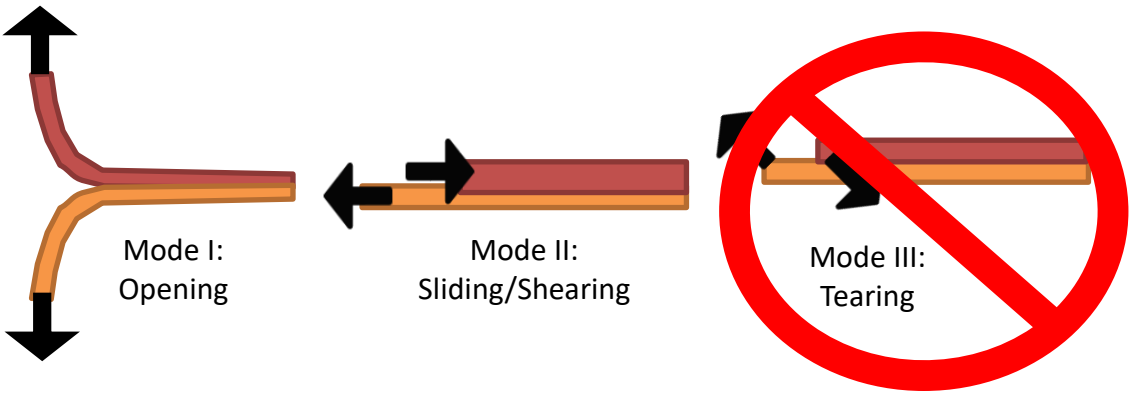

Figure 62: Modes of fracture

For a bi-material set-up, delamination as shown in Figure 63, may occur at the interface (a to b), or kink into the substrate (a to c) or film (a to d). Suo and Hutchinson have observed that the short cracks at the edge would reach a fixed depth and propagate along that depth parallel to the surface [7].

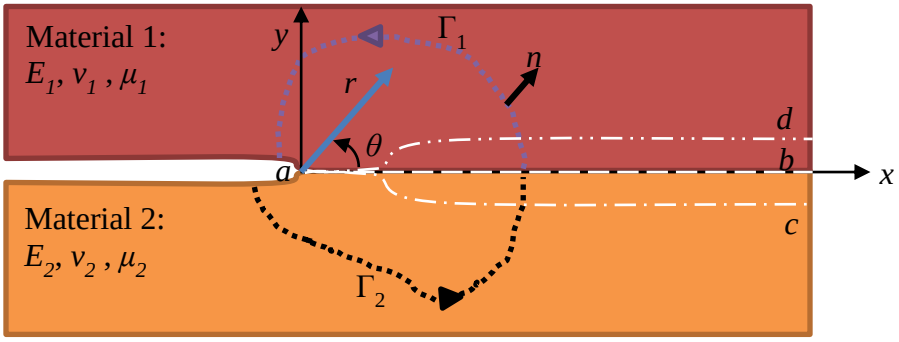

Figure 63: Bi-material schematic at the crack-tip

Stresses at the interface of two elastic materials are oscillatory and the stress intensity is described by the oscillatory exponent (ε_e) and Dundurs parameters (α, β), which are dependent on the Young's Modulus (E), Poisson's ratio (ν), and shear modulus (μ) [36, 37] of the two materials:

$$\varepsilon_e = \frac{1}{2\pi}\ln\frac{\kappa_1\mu_2 + \mu_1}{\kappa_2\mu_1 + \mu_2} = \frac{1}{2\pi}\ln\frac{1-\beta}{1+\beta} \tag{1}$$

Where Dundurs parameters (α, β) are:

$$\alpha = \frac{\overline{E_1} - \overline{E_2}}{\overline{E_1} + \overline{E_2}} \tag{2}$$

and

$$\beta = \frac{\mu_1(\kappa_2 - 1) - \mu_2(\kappa_1 - 1)}{\mu_1(\kappa_2 + 1) + \mu_2(\kappa_1 + 1)} \tag{3}$$

where

$$\frac{1}{\overline{E_k}} = \begin{cases} \dfrac{1 - v_k^2}{E_k} \; plane\ strain \\ \dfrac{1}{E_k} \; plane\ stress \end{cases} \tag{4}$$

and

$$\kappa_k = \begin{cases} 3 - 4v_k \; plane\ strain \\ \dfrac{3 - v_k}{1 + v_k} \; plane\ stress \end{cases} \tag{5}$$

Rice and Shih have shown the complex stress intensity factor in terms of K_1 and K_2:

$$K = K_I + iK_{II} = Kl^{i\varepsilon} = |K|e^{i\varphi} \tag{6}$$

Using SIF, in 2D the stress field

$$\sigma_{yy} + i\sigma_{xy} = \frac{K_I + iK_{II}}{\sqrt{2\pi r}}\left(\frac{r}{l}\right)^{i\varepsilon} \tag{7}$$

and the mode-mixity is:

$$\varphi = \tan^{-1}\left(\frac{\sigma_{xy}}{\sigma_{yy}}\right)_{r=l} \tag{8}$$

It should be noted that the SIF is dependent on the arbitrary length, *l*.

The second approach, strain energy release rate (SERR), quantifies the total amount of strain energy, *G*, that is released per unit area when an existing crack propagates [35, 38].

$$G_T = \lim_{\Delta A \to 0}\left(\frac{\Delta U}{\Delta A}\right) \tag{9}$$

For an interface, the interface energy release rate, *G*, can be related to stress intensity factors for bimaterials and can be shown as [36]*:*

$$G = \frac{1}{H_I}(K_I^2 + K_{II}^2) + \frac{1}{H_{II}}K_{III}^2 \tag{10}$$

where

$$\frac{1}{H_I} = \frac{1}{2\cosh^2 \pi\varepsilon}\left(\frac{1}{\overline{E_1}} + \frac{1}{\overline{E_2}}\right) \tag{11}$$

and

$$\frac{1}{H_{II}} = \frac{1}{4}\left(\frac{1}{\mu_1} + \frac{1}{\mu_2}\right) \tag{12}$$

In terms of computational fracture mechanics which is implemented by finite-element analysis (FEA) as shown in Figure 64, there are various options to determine the interface energy release rate and interfacial crack propagation for the criteria: J-integral, crack extension method, and virtual crack closure technique (VCCT). Cohesive zone modeling (CZM) can also be used for studying interfacial crack initiation and propagation.

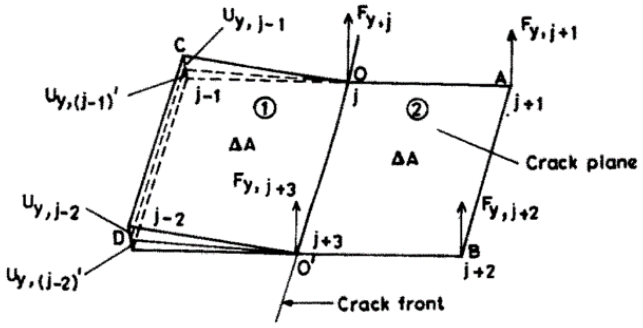

Figure 64 Crack growth with modified crack closure source based on SERR [38]

In J-integral approach, nonlinear energy release rate can be described by a closed line integral in a 2D model. As shown in Figure 63, J-integral's path is evaluated as the sum of integrating about the path in material 2 (Γ_2) and material 1 (Γ_1).

Crack extension approach uses cracks with incrementally increasing lengths in 2D models or cracks with incrementally increasing surface areas in 3D models to determine the energy release rate. VCCT uses the assumption that the energy needed to separate a crack surface is equal to the energy to close the same surface, and so the energy-release rate can be calculated. It is also used for simulations with a known crack path that is defined by interface elements.

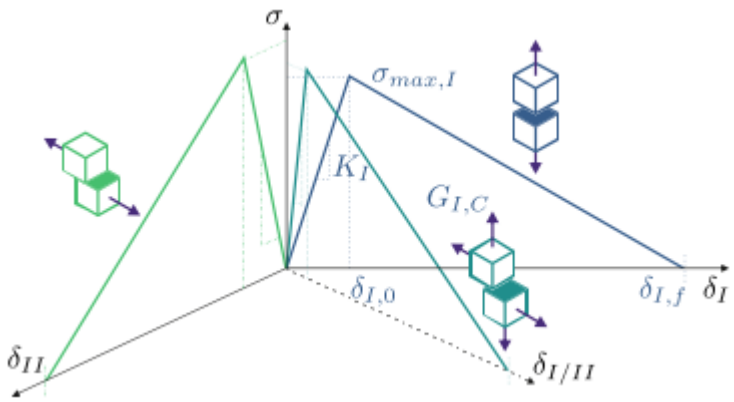

Figure 65 Visualization of bilinear traction separation law for cohesive zone modeling (CZM) [14]

Cohesive Zone Modeling approach is the bridge between the stress-based and energy based methods[39]. It uses a damage tolerance criterion to determine crack nucleation and propagation along a predefined path and has the advantage of ability to predict behavior of un-cracked structures more easily. The damage is based on a traction-separation law, which states an element is reversible up to an initial damage point and the element then has damage which builds up until the crack is extended when the element is "fully damaged." CZM modeling is commonly used for both peel testing and button shear testing, while VCCT is also used in comparison for button shear testing [39-42].

For this work, crack extension technique will be used to determine the critical energy release rate.

1.18 SERR approach to the peel test

For the peel test, Method 1 is simulated with the configuration in Figure 66.

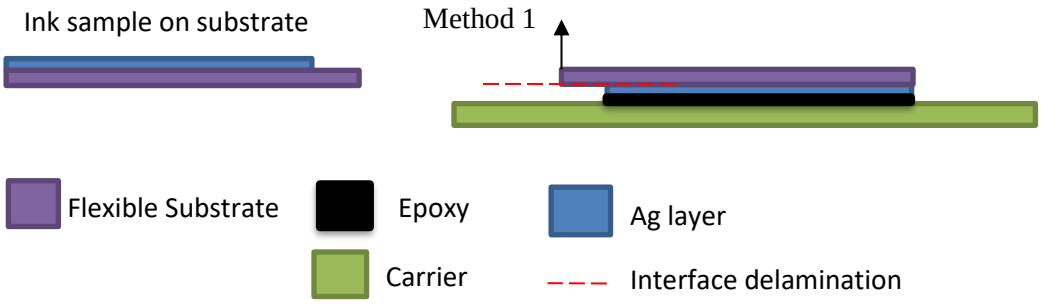

Figure 66: Schematic for the method 1

The two main SERR numerical approaches are integral (J-integral) and Virtual Crack closure techniques [35]. The former is able to account for plasticity which could develop, but there are concerns with thin film when the J-integral hits the boundary of the film [15]. Traditional virtual crack closure is based on the elastic domain, where the energy it assumes the energy to open a crack is equal to the energy to close the crack. An illustration of VCCT is shown in Figure 67 where nodal forces and displacements are used to determine the energy to close a crack. Parks further expanded the VCCT concept to include elastic-plastic materials by considering the integral of strain energy and plastic work for the elements [43]. However, in ANSYS ™, the FEA software utilized for this work, the pre-defined VCCT program does not account for plastic-elastic materials when using the following equations to calculate the energy release rate in terms of mode directions G_I and G_{II} for 2D analysis [44]:

$$G_I = \frac{1}{2\Delta a} R_y \Delta v \tag{13}$$

$$G_{II} = \frac{1}{2\Delta a} R_x \Delta u \tag{14}$$

Where R_x and R_y are the reaction forces at the crack tip, Δa is the crack increment, Δu is the relative displacement of the previous coupled nodes along the *x*, and Δv is the relative displacements of the previous coupled nodes along the *y* axis. McCann et al. developed the sequential crack extension technique (SCE) to keep track of the total work, elastic energy, and plastic work over a series of incremental crack openings for 2D simulations of peel testing of Cu thin films in a bi-material configuration [15]. It is based on the concept that the conservation of energy for propagating a crack where the incremental external work will be equal to the incremental elastic energy, incremental plastic work, and the incremental energy needed to create the crack extension:

$$dW = dU_e + dU_p + dU_f \tag{15}$$

Where dW is the incremental external work, dU_e is the incremental elastic work, dU_p is the incremental plastic work, and dU_f is the incremental energy required used to create the new fracture faces of the crack tip [15]. The last term dU_f when divided by the created crack surface provides the strain energy release rate.

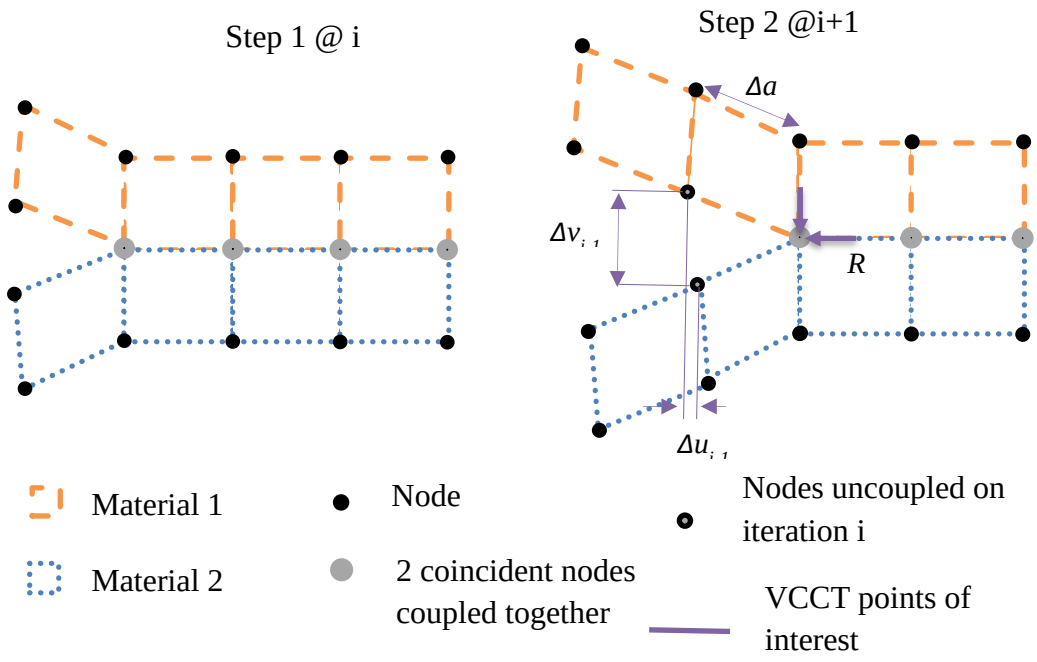

Figure 67: Crack opening comparing the previous close nodes relative displacement for VCCT in 2D [44]

The sequential crack extension technique (SCE) uses the incremental concept of uncoupling nodes at the known interface to determine the strain energy release rate; however, it then keeps track of the change in the strain energy related to each increment.

$$G_c => G_{ss} = \frac{dW_{ss}}{dA} - \frac{dU_{e,ss}}{dA} - \frac{dU_{p,ss}}{dA} \tag{16}$$

In terms of the new surface area created, *A*, is equal to incremental crack length multiplied by unit out-of-plane thickness in a 2D model and is equal to incremental crack area in a 3D model. The work input into the system during peeling can be assumed to be from the steady state force needed to delaminate the flexible substrate arm material, multiplied by the distance the gripper has traveled in the vertical direction with each

incremental crack step. From this the following can be written to determine the incremental external work per unit area in a 2D model:

$$\frac{dW}{dA_{i+1}} = \frac{P(v_{i+1} - v_i)}{b(a_{i+1} - a_i)} \tag{17}$$

Where P is the steady-state load of delamination from the peel experiment, v is the displacement at the load end, b is the width of the sample and a is the crack length [15]. Thus, $(v_{i+1} - v_i)$ represents the upward travel of the delaminating arm, while $(a_{i+1} - a_i)$ represents incremental crack extension. Both the elastic strain energy and plastic work terms are based on the system's energy before and after the crack increment:

$$\frac{dU_e}{dA_{i+1}} = \frac{U_{e,i+1} - U_{e,i}}{b(a_{i+1} - a_i)} \tag{18}$$

$$\frac{dU_p}{dA_{i+1}} = \frac{U_{p,i+1} - U_{p,i}}{b(a_{i+1} - a_i)} \tag{19}$$

Where U_e is the elastic strain energy and U_p the plastic work of the total system [15]. The sequential crack extension technique is useful for models which have elastic-plastic materials under high strain, a known crack path and experimental results to use for inputs into the model. If one of these are missing, there may be better model options or more steps to be taken by the user. For example, the J-integral and VCCT techniques are easily available for implementation and well documented. The general procedure are outlined by McCann et al. as explained below as well as in Figure 68 [15]:

1. Ramp the vertical load steps to reach the $P_{ss.}$ Here P_{ss} stands for the steady-state peeling force.

2. While maintaining the load, decouple the pair of nodes at the crack tip mimiching crack extension.
3. Evaluate dW/dA, dU_e/dA, and dU_p/dA for the entire system.
4. Repeat 2 and 3 until the values in 3 become stable. As the crack extends and as the delaminating arm increases in length, it takes a few crack extension steps for the values to stabilize. Mesh size should be appropriately refined to ensure convergence.
5. Once all values in step #3 have stabilized, the critical energy release rate, $G_{ss,}$ can be obtained using equation (20).

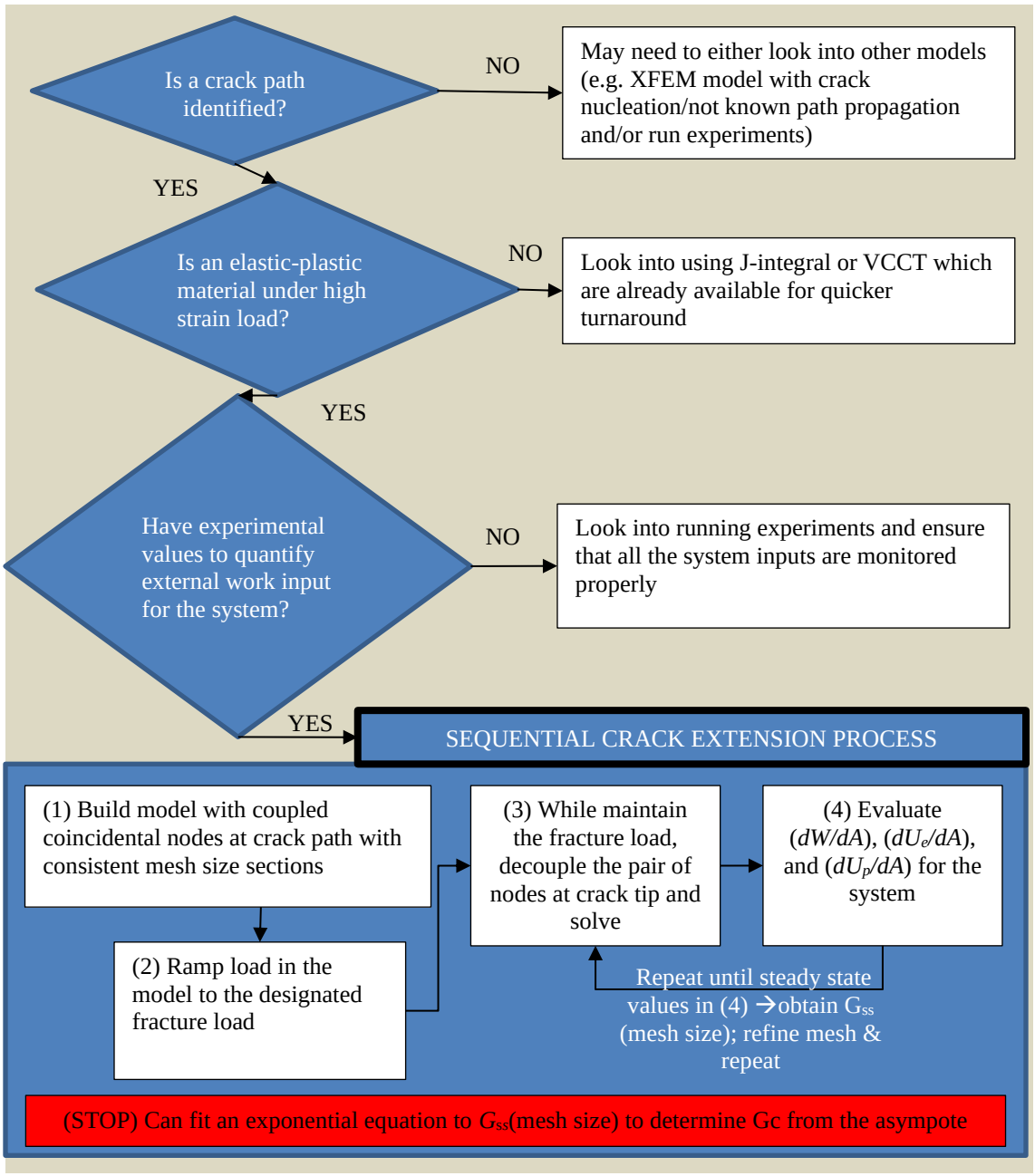

Figure 68: Flow chart for using the sequential crack extension method

1.19 Numerical simulation of peel test Method 1

For Method 1, a parameterized script was written in ANSYS™ Parametric Design Language (APDL) scripting language to create the finite-element model. With the configuration, a 2D plane linear quadrilateral element (ANSYS™ plane182 with option for plane strain assumption) was chosen to decrease the computational time. The element accounts for isotropic elastic-plastic materials as well as orthotropic elastic properties which were identified for the material stack-up.

1.19.1 Geometry

Since there was an assumption of plane-strain and 2D element was utilized, the geometry only needed to mimic the cross-section of the structure as shown in the schematic of Figure 69. The main dimensions of concern were the thickness of layers, listed in

Table 10 provides the thickness values for various materials used in the study. As the thickness of many material layers are in the tens of microns, while the length of the sample was several orders of magnitude larger than the thickness of the material layers. Thus, to reduce the computational time, the total length of the sample that was modelled was a few mm. Also, the simulated length of the peel arm was short to include the curved segment of the peel but not much of the straight portion of the peel arm.

Table 10: Dimensions for geometry

	Material	Thickness (mm)
Flexible Substrate	LCP	0.1100
Ink	Porous Ag ink	0.0100
Epoxy	Quickweld Epoxy	0.0750
Carrier outer	Cu Clading	0.0505
Carrier core	FR-4	1.6850

Since the ink was one of the interfaces of interest and the same magnitude as the thickness of epoxy, the ink and epoxy layers must be included in the geometry as well. The geometry model was built by the bottom-up approach with the geometry parameters defining keypoints in the space→ lines from the keypoints → delamination have coincident points define. Two lines were defined, so that each one was associated with only either the upper or lower areas in between the crack path.

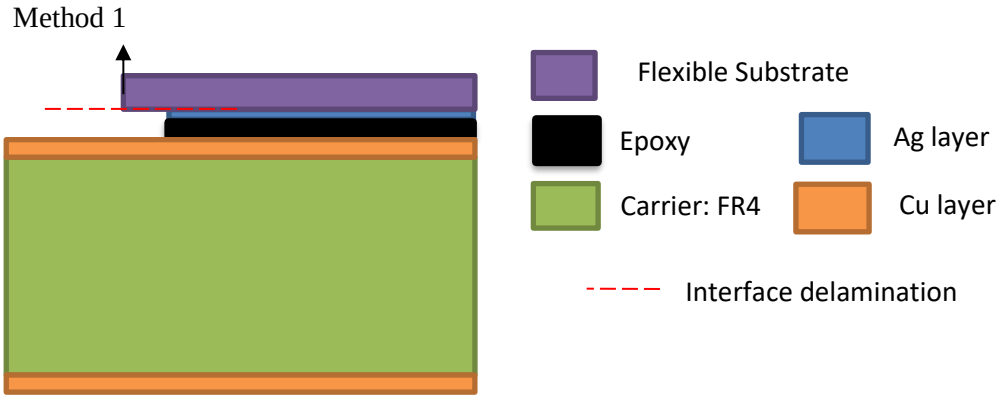

Figure 69: Schematic for dimensional reference

Since the model intended to have four different mesh sizes along the crack, the geometry was built to have designated mesh area sections in the geometry for the materials near the interface delamination/crack path as shown in Figure 70.

Figure 70: 2D Geometry with designated mesh area sections along the crack length, the colors assigned to the area are random

1.19.2 Material properties

Across the adhesion experiments, the material properties needed include the Ag ink, the substrates (LCP or PET), the carrier, and the epoxy to adhere the sample to the carrier.

1.19.3 Sintered porous Ag ink

For the Ag ink, the Young's modulus, 13 GPa, was obtained through a 3x3 nano-indention grid pattern on a Hysistron Triboindentor, which calculated the modulus from on the unloading portion [45]. The measurement was performed on a sample with 8 passes of ink to ensure that the ink's thickness was greater than ten times the deepest indention depth so that there no effects of the underlying LCP substrate on the measurement [45]. For porous sintered Ag ink film, the power electronics application gives many literature references on similar porous Ag structures. In the work of modeling power modules, references indicate porous films act as an elastic perfectly plastic material without creep effect up to 150 ^{0}C [46]. Similarly, they also report the elastic modulus to be 10 GPa, which is close to the 13 GPa measured for the Ag film [45, 46]. The yield strength was estimated to be the density*bulk yield modulus, which for 80% density of Ag was taken to be 43 MPa, and the tangent modulus was 0 for the perfectly plastic. Since only a 3D image could truly capture the volume's porosity, a rough porosity calculation was computed through a file available on the exchange section of Mathwork's Matlab^{TM} website from a 2D SEM image, which are available from the experiments in Chapter 3. This program bases the porosity calculation on k-means clustering to reduce the image into sections of pores verses material [44]. In this program, 4 cluster bins are used to determine the final bi color pictures identifying the voids in black verse the material in white as shown in Figure 71. The figure

shows the porosity close to 20% for the ink sintered at 200 °C for 30 mins, and the range of porosity was found to be as small as 13% in the ink sintered at 500 °C, to 30% in one of the layers of the thermally treated samples.

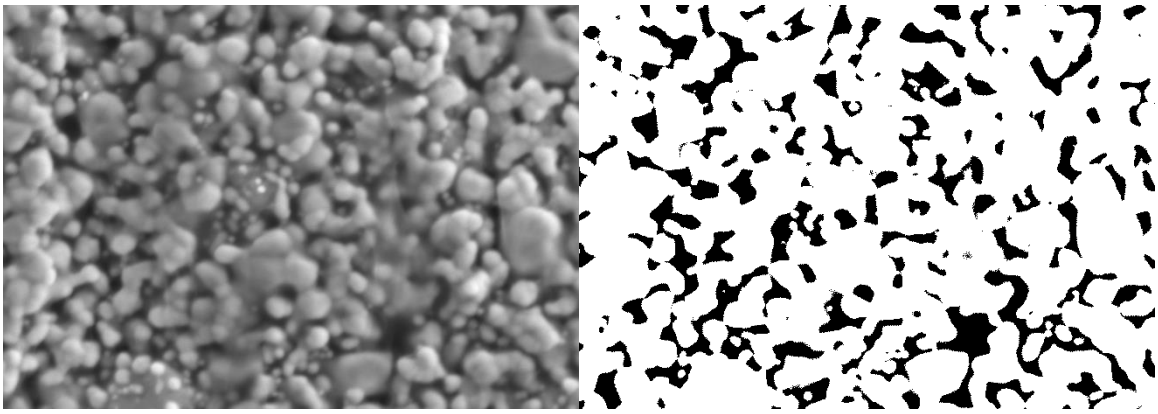

Figure 71: 19.64% porosity calculation by estimation based on K-means clustering

The Ag film was taken to be isotropic elastic perfectly plastic through a bilinear isotropic hardening model where the plastic yield was at 43 MPa. However, it is important to note in the discussion about the interfacial strength that the sample in the simulation does not undergo unloading. Also since the intensions of the FEM was to understand the stresses at the interface in general, and not to predict the exact failure within the ink porous structure, the film was generalized to be isotropic block and did not model the individually connected Ag spheres of the structure. The Poisson's ratio for the film was taken to be the same as for bulk silver, 0.37 [46].

1.19.3.1 Substrate: Liquid Crystalline Polymer (LCP)

The liquid crystalline polymer was chosen for its stable dielectric constant and low loss which is advantageous for high frequency applications like ink-jet printed antenna arrays. Rogers Corporation provided ULTRALAM® 3850HT, which works well for high

temperature, since the Ag sintering range is on the higher end. For the LCP, it was considered to remain in the elastic regime and the numbers obtained in Table 12 were taken from the technical datasheet supplied by Rogers Corporation [47].

1.19.3.2 Substrate: Polyethylene terephthalate (PET)

Novele ™ IJ-220 PET was manufactured for NovaCentrix® by Mitsubishi Imaging (MPM), Inc. [32]. It is a transparent PET film with a special mesoporous coating that allows for the ink to be conductive by wicking away the coating which prevents the nanoparticles from agglomerating in the Melaton® Ag ink solution while sitting at room temperature. General PET properties are taken for the model's Young Modulus: 2.1 GPa and Poisson's ratio: 0.34 [48].

1.19.3.3 Carrier layer: FR-4 / Cu clad

For many of the tests, a carrier substrate was used that consists of a FR-4 core cladded on both sides with Cu. FR-4 is a composite material consisting of woven fiberglass and epoxy resin. Often the core consists of multiple laminate sheets of the woven fiberglass encased in the resin. Due to the woven nature of the material, the material properties are considered orthotropic with differentiations in properties along the *X*, *Y*, and *Z* directions. The material model available was orthotropic as well as temperature dependent as shown in Table 13 [49, 50].

For the Cu material with the random grain directions, Cu was modeled as an isotropic material. The values for the Young's Modulus (109.7 GPa), Poisson's ratio (0.34) were taken from literature [5].

1.19.3.4 Epoxy Material Properties

A two-part ClearWeld ™ epoxy by JB Weld was used due to the wide range of dry surfaces it can bond including metals to fiberglass, plastic and wood. A bulk epoxy sample was used for obtaining the Young's modulus by nano indention with a Hysistron Triboindentor. For the measurement, a conical shape tip with a radius of 1 μm was applied to the ink surface through a range of loads [1000:200:2600 μN] across the nine points, which were arranged in a 3x3 grid pattern. During the test, the load and displacement on the tip were monitored, and the Young's modulus was estimated from the unloading potion of the curves that are shown in Figure 72. Table 11 shows the results for the estimated Young's modulus as well as the measured depth of the indention. The results for 1600 μN load was considered an outlier and was not taken into consideration for the average Young's modulus 2 GPa for the epoxy. For must epoxies, the Poisson's ratio is in the range of 0.3-0.35 with 0.3 being commonly used for modeling [51].

Table 11: Overview of the epoxy indention

Indention Force (μN)	Depth (nm)	E (GPa)
1000	676.02	2.308
1200	791.49	2.201
1400	1039.99	1.909
1600	1206.63	3.428
1800	1236.14	2.338
2000	1295.42	2.221
2200	1419.87	2.804
2400	1515.99	1.547
2600	1965.34	1.432

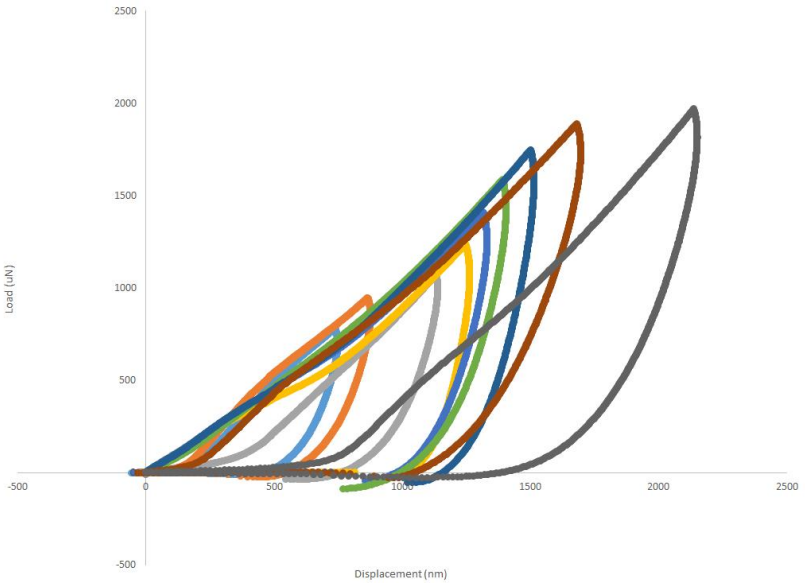

Figure 72: Load-displacement curves from a 3x3 grid indention test on epoxy

1.19.3.5 Material property overview

Table 12 and Table 13 provide the material properties used in the numerical simulation of peel test.

Table 12 Overview of material properties

	Young's Modulus (MPa)	Poisson's ratio (-)	Yield Modulus (MPa)	Tangent Modulus (MPa)
Porous Sintered Ag [45, 46]	13000	0.37	43	0
LCP [47]	3406	0.35	-	-
PET [48]	2100	0.34	-	-
Elastic Cu [5]	109700	0.34	-	-
Epoxy [51]	2000	0.35	-	-

Table 13: FR-4 orthotropic temperature dependent material model for FR-4 [49, 50]

Property	Temperature (^{0}C)					
	30	95	110	125	150	270
E_{xx} (MPa)	22400	20680	19970	19300	17920	16000
E_{yy} (MPa)	1600	1200	1100	1000	600	450
E_{zz} (MPa)	22400	20680	19970	19300	17920	16000
G_{xz} (MPa)	630	600	550	500	450	441
G_{xy} (MPa)	199	189	173	157	142	139.3
G_{yz} (MPa)	199	189	173	157	142	139.3
v_{xz}	0.136	0.136	0.136	0.136	0.136	0.136
v_{xy}	0.142	0.142	0.142	0.142	0.142	0.142
v_{yz}	0.136	0.136	0.136	0.136	0.136	0.136
CTE_{xx}	20e-6	20e-6	20e-6	20e-6	20e-6	20e-6
CTE_{yy}	86.5e-6	86.5e-6	86.5e-6	86.5e-6	86.5e-6	86.5e-6
CTE_{zz}	20e-6	20e-6	20e-6	20e-6	20e-6	20e-6

1.19.4 Finite-element mesh

For the mesh, the main parameters of consideration were the number of elements through the smallest thickness, which in this case was the ink layer. A minimum of 5 elements was designated for the ink thickness. For the four mesh area zones along the crack as shown in Figure 73, the mesh size along the length was as follows: M1- 2 μm, M2- 1 μm, M3-0.5 μm and M4-0.25 μm. Ahead of the crack tip, the elements were pre-defined to be same size as the elements in the ink thickness. For the areas farther away from the crack, the mesh was scaled up from the element size in the ink layer. In the areas of M1-M4, the lines defining the edge of the delamination were sized so that the elements formed will have coincidental nodes for the upcoming boundary conditions. As shown in Figure 73, the material properties correspond to the element's color: FR4- magenta pink, Cu – red, Epoxy – lime green, Ink – periwinkle blue and LCP – light blue.

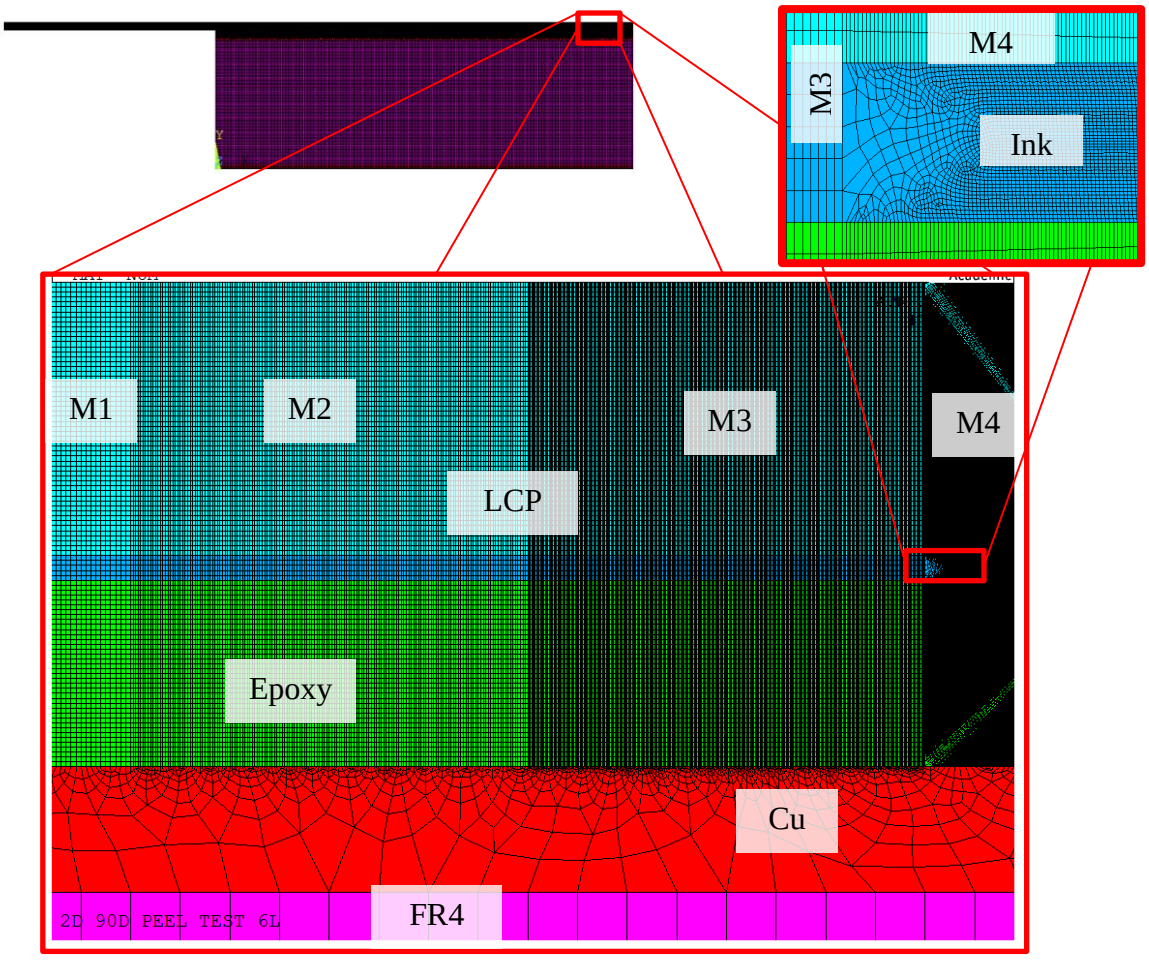

Figure 73: Example of mesh with the designated mesh areas – with mesh sizes M1 (2 µm), M2 (1 µm), M3 (0.5 µm), and M4 (0.25 µm). The colors of the elements maps the material property associated with the element

1.19.5 Boundary Conditions

For the boundary conditions as shown in Figure 74, the following were conditions defined and placed on node(s): a force load to mimic the tweezer pulling up, fixed constraints at the bottom for the carrier, coupled node sets along the crack interface to keep the crack closed, and the cuts done in the carrier to reduce the element count.

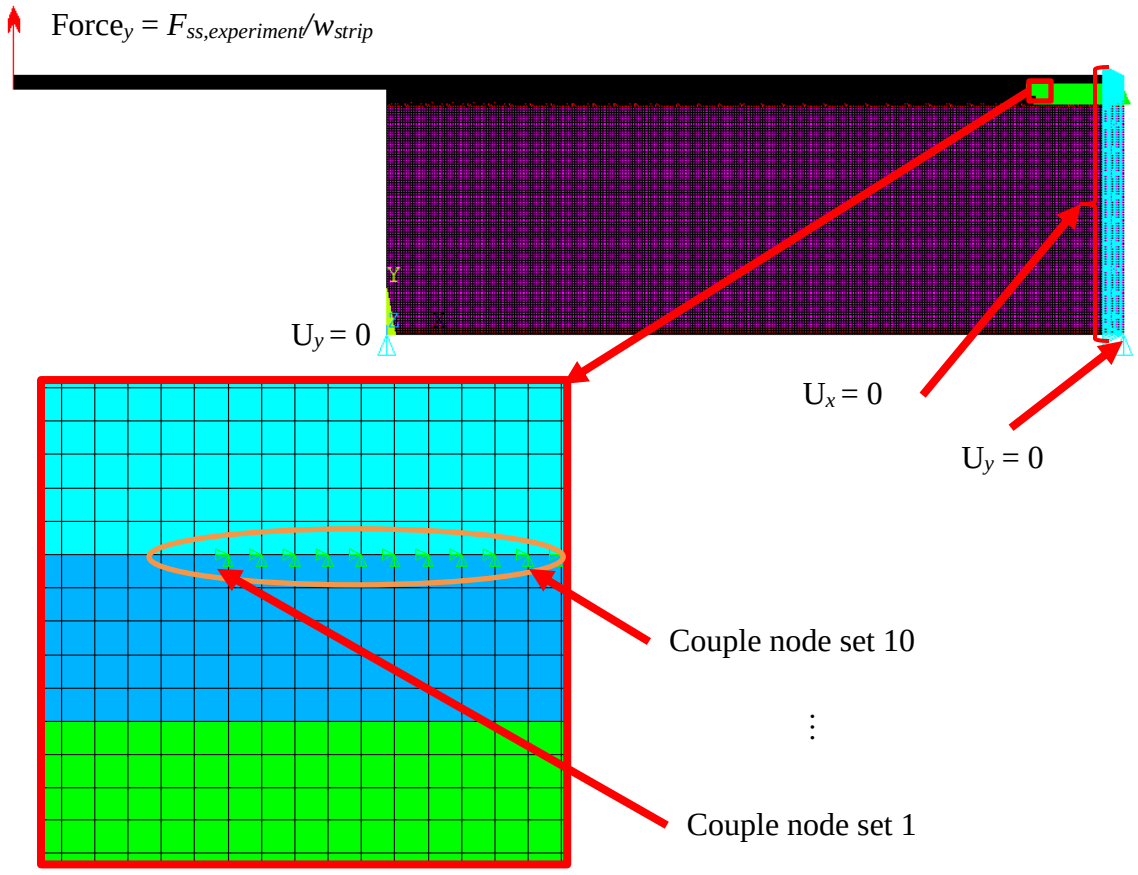

Figure 74: Boundary conditions

For the force load to mimic the tweezer pulling up, the load from the experimental steady state peel measurement was divided by the strip's width to let the load correspond to the 2D geometry with unit thickness in the out-of-plane direction. The nodes at the left edge of the flexible substrate were coupled together and the load applied uniformly across the nodes in the y-direction.

As discussed earlier, with the load applied to the delaminating arm, the coupled nodes at the ink and flexible substrate interface were sequentially decoupled to mimic crack propagation.

1.19.6 Post-processing: Stress/strain contours

Figure 75 shows peel stress (σ_{yy}) distribution, and the peanut-shape distribution around the crack tip could be seen.

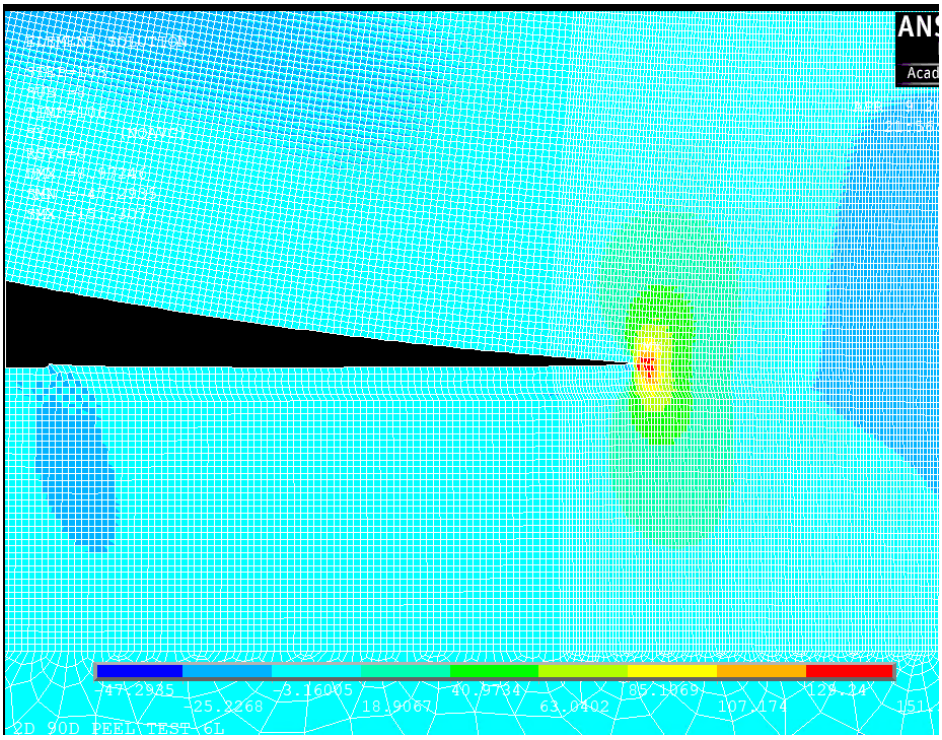

Figure 75: Stress in the *y*-direction (legend is in MPa)

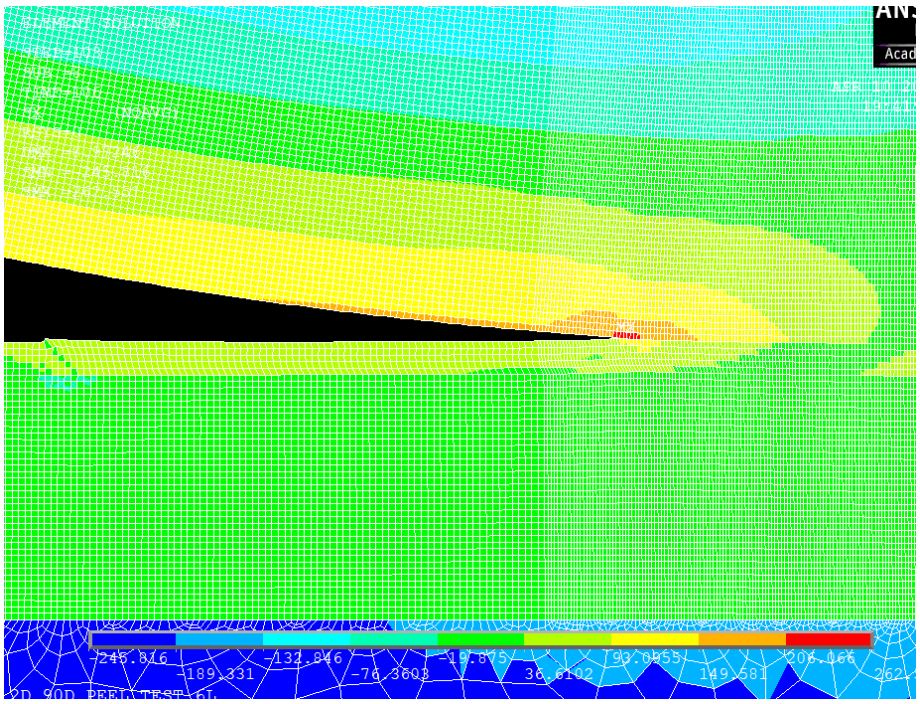

Figure 76: Stress in the *x*-direction (legend is in MPa)

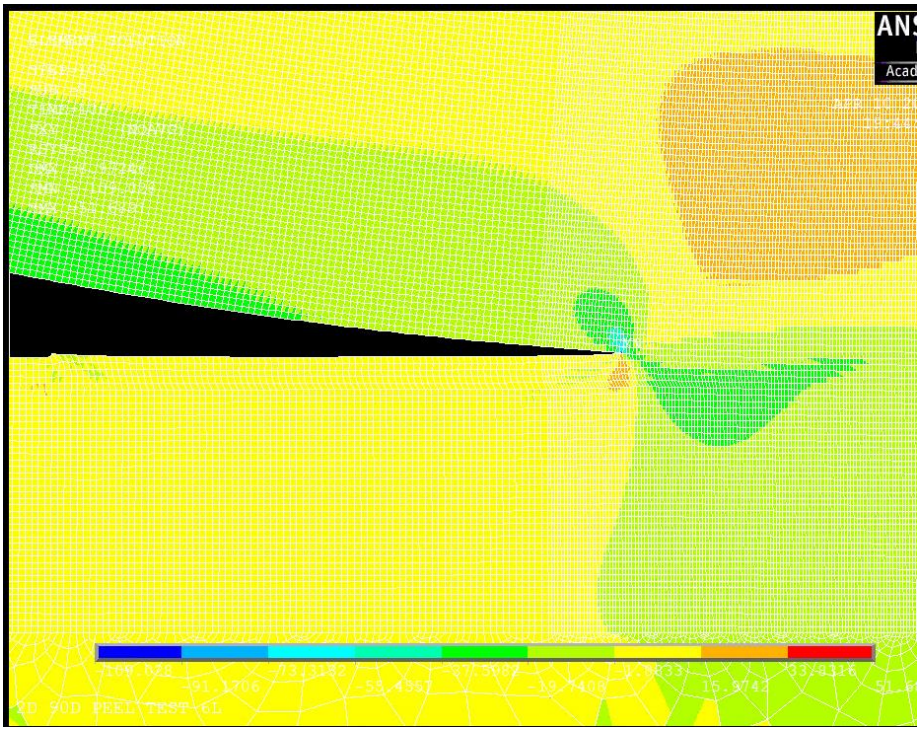

Figure 77: *xy* shear stress (legend is in MPa)

1.19.7 Post-processing: Determination G

Three different mesh sizes were examined (2 μm, 1 μm, and 0.5 μm) in the simulation of a crack length of 160 μm for a total crack length of 480 μm. When the crack passed through from one mesh size to the next, the energy values did show an offshoot for transitioning through one element and stabilized subsequently as shown in Figure 78 and Figure 79. The incremental work per unit area into the system was taken from the experimental steady state force, 0.4 N, and the numerically calculated v displacement for each time step. As seen in Figure 78, the incremental elastic energy per unit area was small, while the incremental plastic work per unit area was about 40 J/ m^2. When incremental elastic energy per unit area and the incremental plastic work per unit area were subtracted from the incremental work into the system, critical energy release rate G_c was computed to be almost 100 J/m^2 using equation (16)

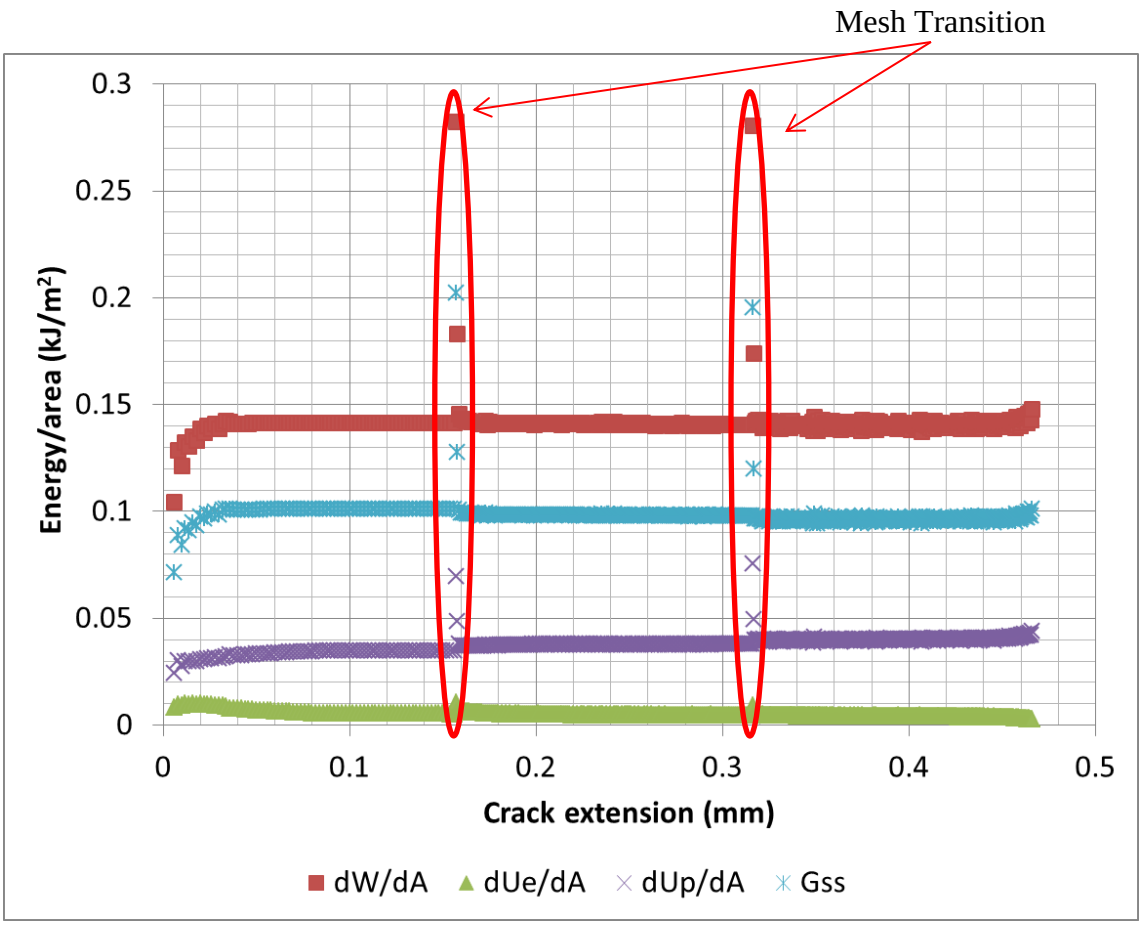

Figure 78: Energy with respect to crack opening

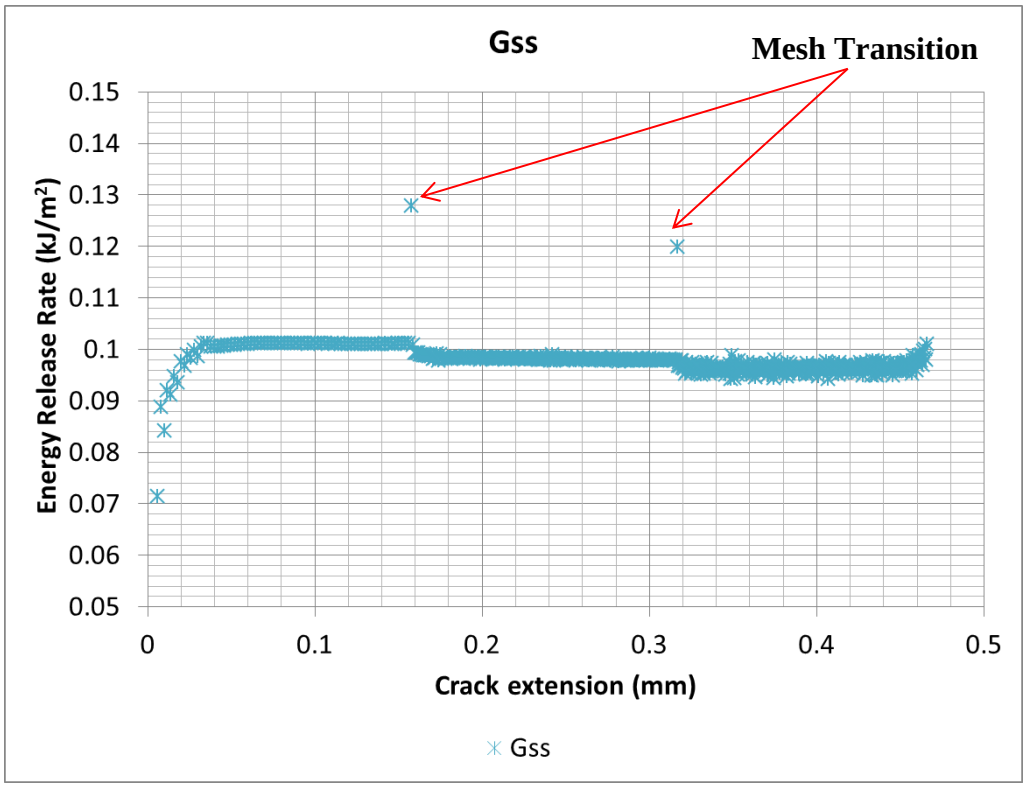

Figure 79: G for better scale understanding

For the modeling Method 2 configuration, the same approach can be used from Method 1. However, the main difference is the geometry cross-section. For the modeling the experiment, the only substitute layer that should be considered for simulation is the FR4 due to the non-consistent results with the Cu foils.

1.20 Conclusions

In this chapter, the sequential crack extension method was used to calculate G_c for Method 1 peel test and was found to be 100 J/m^2. In this work, the ink was assumed to be elastic, perfectly plastic with a yield strength of 43 MPa, and thus, ink exhibited incremental plastic work per unit area of about 40 J/m^2. If one were to determine through experiments that the ink was not perfectly plastic and that the yield strength was higher,

the plastic work would have been small, and thus, G_c would have been closer to 150 J/m^2. Thus, additional mechanical characterization of all materials involved in this study would be necessary to get a closer estimate of G_c.

ASSEMBLY PROCESS DEVELOPMENT AND CHARACTERIZATION

Flexible microsystems are attractive due to their stretchability, twistability and foldability, which allow them to conform to complex surfaces. Current flexible microsystems are utilizing printed electronics in the flexible space, beyond the traditional Cu-clad technology. To achieve better pitch scalability and electrical performance, sintering technologies offer the best fully-additive solution for assembling components onto printed electronics [22].

Ag ink trace assembly and die shear studies have been completed on various substrates, including paper, polyimide, and glass [17][17]. In their work, the authors used either solder, epoxy, or sintered ink for device assembly. Arrese et al. have used sintering process to assemble surface mount devices [17]. In their sintered ink process, they deposit ink after the resistor is placed. Although depositing ink after device placement works for resistors with two pads, this process is not likely to work for flip-chip applications which may have full area-array interconnects. For the full area, connections are also on the inside of the chip, not just on the perimeter. A preferable procedure of assembly is to place the ink on the substrate pads, place the component, and finally sinter the entire assembly in an oven. In this work, the all-sinter process is demonstrated for a two-pad resistor for different test cases. The developed process is not only helpful for a two-interconnect assembly but can also be extended to multi-interconnect assembly, including area-array configurations.

1.21 Development of assembly process steps

The demonstration vehicle was a 50kΩ, 603 resistor case with gold electrodes and dimensions shown in Figure 80. Ag traces printed onto an electro-less nickel immersion gold (ENIG) surface were considered to help isolate the joint. If there is not enough Ag available, voids will form at the Ag/Au interface and weaken the interfacial strength. Additionally, if an ENIG step was added on the printed trace surface, it would create complexity with the chemical bath for the remote user. Theoretically an ENIG finish on the surface mount device has a better metallurgical bond to Ag compared a Cu to Ag electrode. Further literature review revealed that the diffusion from Au to Ag is higher than Ag to Au or Ag to Ag [52]. The ENIG finish also helps prevent oxidation of the resistor's pad surface.

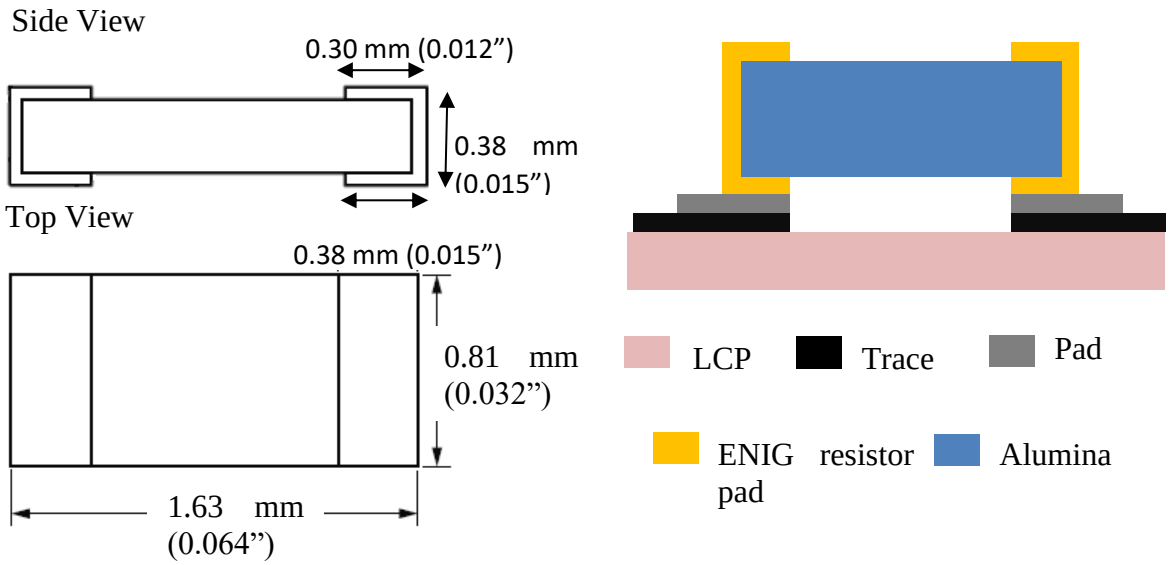

Figure 80: Layout and dimensions of a 603 resistor

A commercial Fujifilm Dimatrix™ DMP 2831 ink jet printer was used to deposit SunChemical® SunTronic™ EMD 5730 Ag ink. First, Ag traces with pad layouts were printed on a flexible substrate and then sintered at 200 ^{0}C for 30 minutes in an oven as shown in Figure 81. In the present study, bare Rogers Ultralam® 3850HT LCP substrates were used for demonstration purposes. Additional Ag ink was then printed on the contact pads on the substrate for assembly purposes. The resistor was then placed on the contact pads using a semi-automatic Finetech® Fineplacer® flip-chip bonder to ensure planarity and pressure control. There were multiple resistors placed on the same substrate. After component placement, the substrate with the resistors was placed in a thermal oven to be sintered at 200 °C for different time durations, and no pressure was applied to the resistors during the sintering. However, due to the various locations of equipment, there was not a strict profile due to transfer times. After assembly, the component was evaluated through die-shear tests. The following process is a fully-additive assembly process as an alternative to conventional solder flip-chip bonding. Although resistor assembly was demonstrated in this work, the long-term aim is to apply the assembly process for quad flat package (QFNQFP), flip-chips, and other packages in the future.

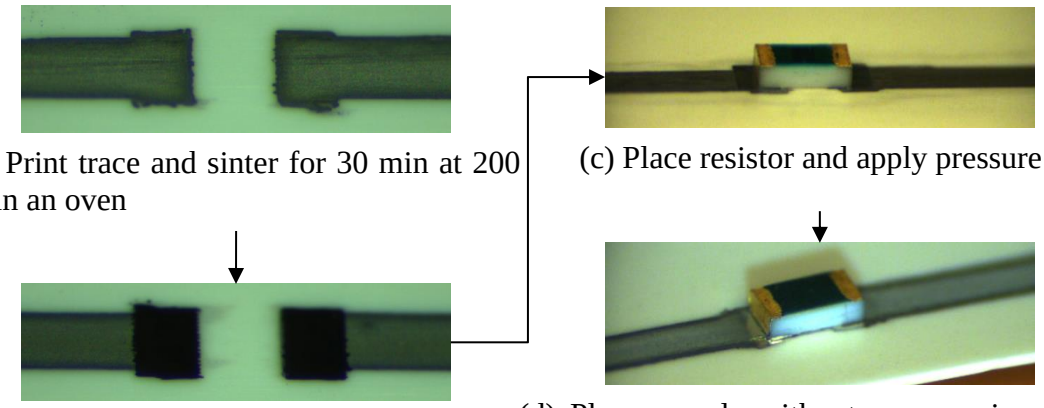

(a) Print trace and sinter for 30 min at 200 °C in an oven

(b) Print additional ink on trace pads

(c) Place resistor and apply pressure

(d) Place sample without pressure in an oven at 200 °C. Picture shows the assembly after sintering.

Figure 81 Full-ink assembly process

1.22 Tool Parameters and Fixturing for Die Shear Testing

XYZTEC™ adhesion test tool was used to perform the die shear test. For die shear testing specifically, the base of the sample sits in the vice configuration. Due to the flexible substrate not being able to remain planer in the vice during the test, a stiffer carrier was needed. either taped and/or glued to the carrier as shown in Figure 82.

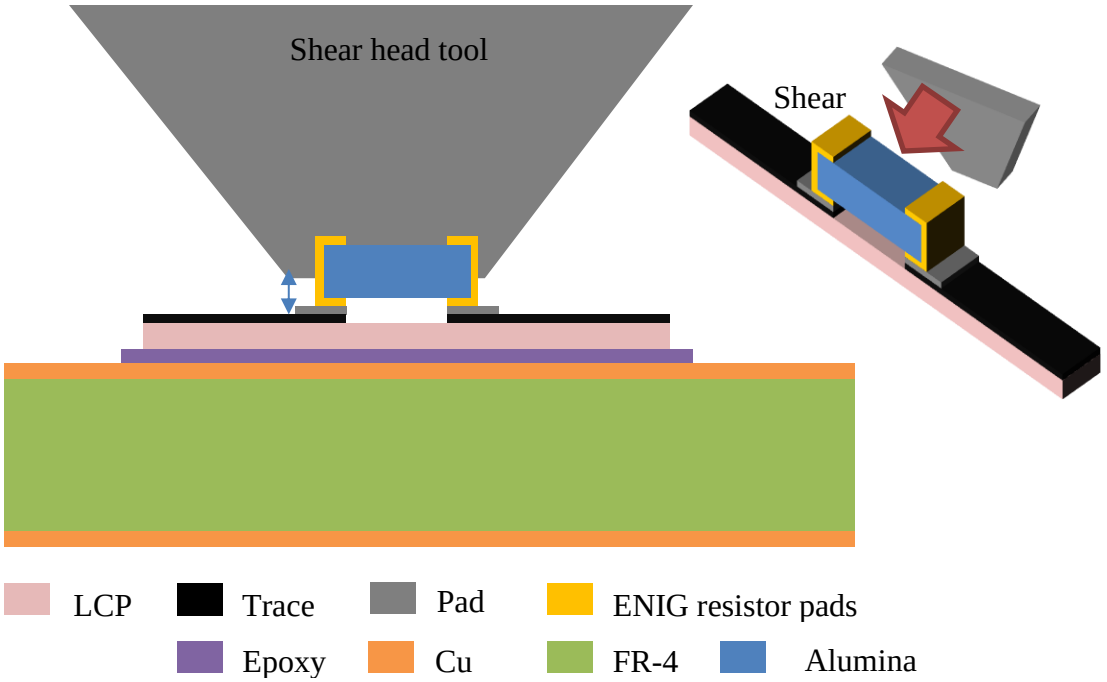

Figure 82: Schematic for the Die Shear testing

For the test, there were two main parameters: the shear height and shear rate. When the shear head does not cover most of the height of the device, the force from the shear head acts as a tipping force, rather than a shear force on the interconnect. The direction of the shear head also needs to remain horizontal, so that the applied force is shear. The shear head should cover at least 80% of the device as illustrated in Figure 82. For the resistors, a more sensitive head is needed to ensure it would capture the peak force. Thus, a rotatable 10 kgf head is used for its sensitivity while also maintaining a parallel position to the device. The force increases after the head hits the device until a critical peak is reached, when the resistors shears off, resulting in a quick drop of force as shown in Figure 83. Literature indicated that faster shear rates give clearer understanding for the fracture failure [34] and is one of the parameters listed in the experimental data.

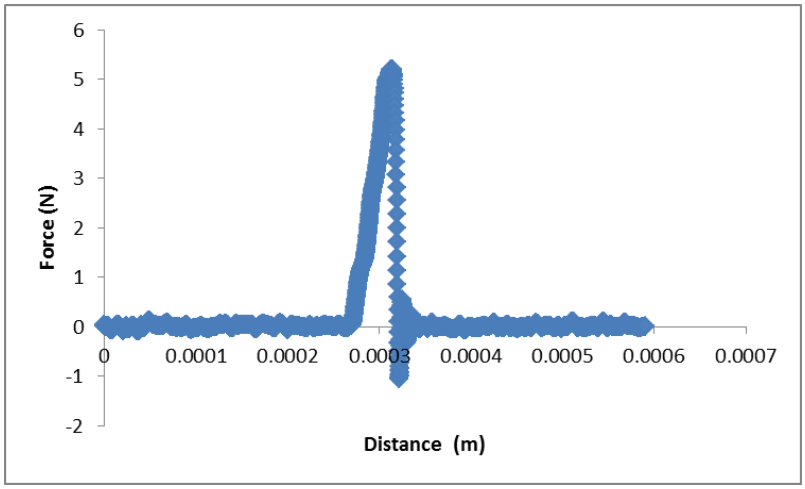

Figure 83: Example force versus displacement data for Die Shear Test

1.23 Experimental Data

Table 14 lists several different case studies with associated parameters: (1) the number of passes the printer used to deposit the ink, (2) applied force, (3) oven time, (4) shear testing rate and (3) fixturing. For the direct write technique, the printer does the entire print, and the time will depend on the number of jets used for the jetting process and the size of the entire print area. The volume of ink available increases with the increased number of passes and jets used. However, due to evaporation the volume of the solvent decreases with increasing print time and there may not be enough active solvent for sintering. With a controlled force, the pressure applied at the interconnect can be determined for approximation onto other devices in the future. Ideally, the oven time is shorter to decrease the processing time. The initial shear rate was 16.7 μm/s to compare to literature for the first test case [53]. Since literature [34] also indicated that faster shear rates would give clearer understanding for the fracture, and the rate was increased to 100 μm/s for the later cases. A fixturing variable checked if transferring the sample between

laboratory locations had any effect, and also kept the flexible substrate flat during device placement of the assembly.

Table 14: Case descriptions

Case	# passes	Placement Force	Oven time	Shear testing rate	Fixturing
1	4	0.2, 0.5, 1.0, 3.0 or 5.0	15, 30, 45 or 60 mins	16.7 μm/s	No tape
2	2, 4, 6 or 8	1, 5 or 10	60 min	100 μm/s	Tape
3	4, 6	1, 3	60 min	100 μm/s	tape
4	6	3	60 min	100 μm/s	Varies

While the assembled products were examined to understand how the joint formed, the sheared products were examined for the resulting fracture profile. Fracture could occur between layers at the interface, through a layer, or a mixture of both as demonstrated in Figure 84. Possible interfacial failures could be between substrate (LCP)/trace, trace/pad, pad/ENIG lead, or pad/alumina resistor. Additionally, fracture through the trace or pad layer is possible. Optical microscopes and scanning electron microscopy (SEM) were used for examination.

For these surface mount devices with sintered ink interconnect, there was not enough ink material to wet up along the vertical sidewall. These did not have the same strength as reported in literature for soldered components with sidewalls. This was a limitation with the ink and the printer choice chosen for this demonstration purpose.

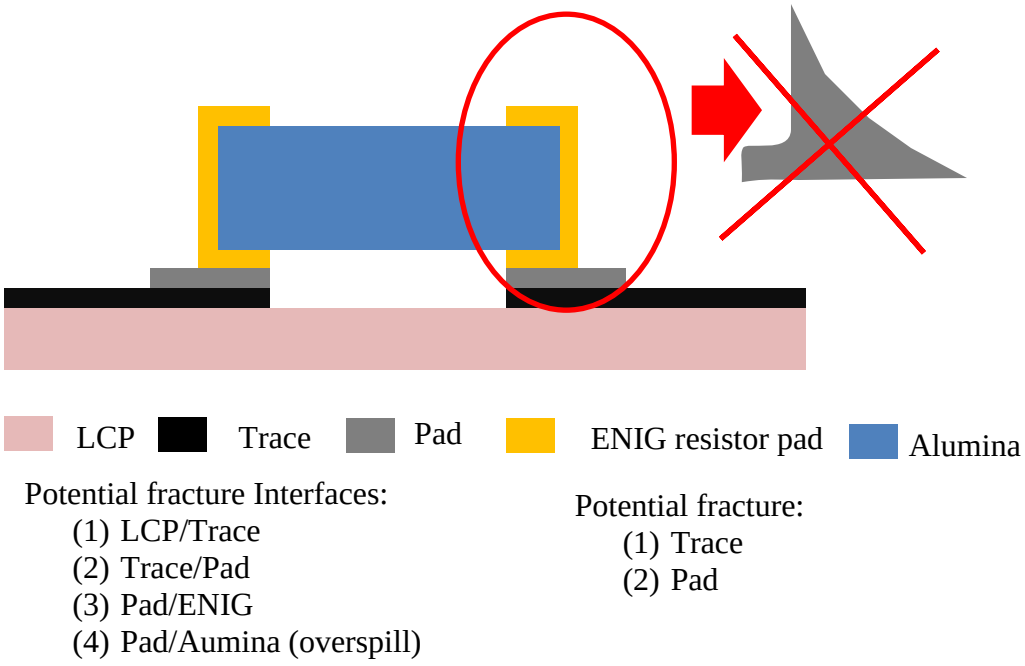

Figure 84: Potential Fracture points

1.23.1 Case 1: Applied force and oven time variable

For case 1 the parameters include the sintering time and the placement force during assembly. Die shear testing allows comparison of the strength of the joints with the XYZTEC™ as shown in Figure 85. The die shear testing was done at a 16.7 μm/s shear rate. In Figure 85, the horizontal axis shows different sintering times, while the vertical axis shows the maximum shearing force as measured in XYZTEC™.

As seen, the higher forces during device placement generally lead to higher shearing forces indicating stronger device-to-substrate joints. However, for a given placement force and for a given sintering time, there were variations in the maximum shear force. This is because multiple resistors were placed and assembled on a coupon of LCP

flexible substrate. Warpage-induced non-coplanarity issues influenced where the resistors were placed on the flexible substrate, and the location affected shear force results. When the placement force was in the range of 3.0 to 5.0 N, the die shear force had a mean value around 4 N, and was higher than when the placement force was in the range of 0.2 N to 1.0 N. Thus, for 4-layer printing, a placement force of 3.0 to 5.0 N is preferred. Also, it is seen from Figure 85 that the preferred sintering time is between 30 - 60 minutes.

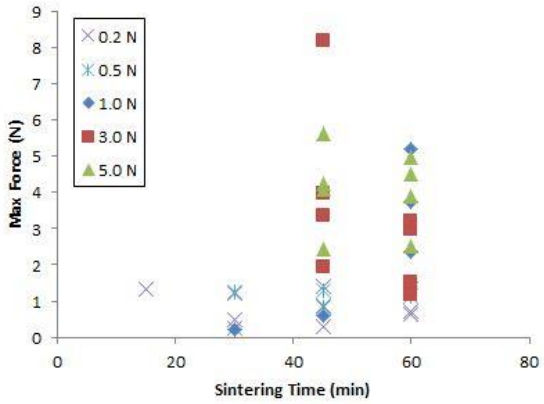

Figure 85: (a) Shear results for different resistors placed with different placement forces (0.2, 0.5, 1.0, 3.0, and 5.0 N) and varying sintering times in an oven set at 200 °C. The image next to the legend shows a resistor about to be sheared.

Figure 86 shows four samples with pad and trace areas on the substrate side after shearing the resistors. The images are from test coupons that had been assembled with 5.0N force and 60 min sintering time at 200 °C. In the images, bare LCP can be seen where the joints were sheared. This indicates that Ag ink got sheared off from the LCP substrate.

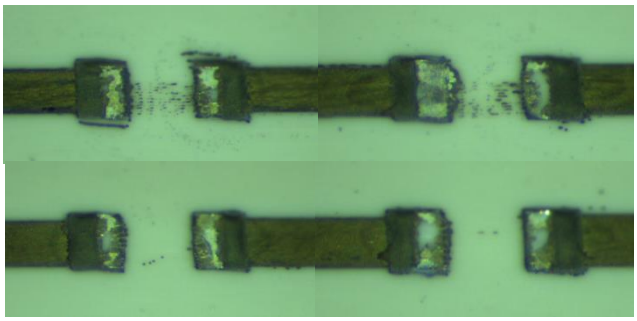

Figure 86: Shearing of assembled resistors (assembly parameters: 5.0 N force and 60 min sintering time) shows bare LCP substrate under the ink pad

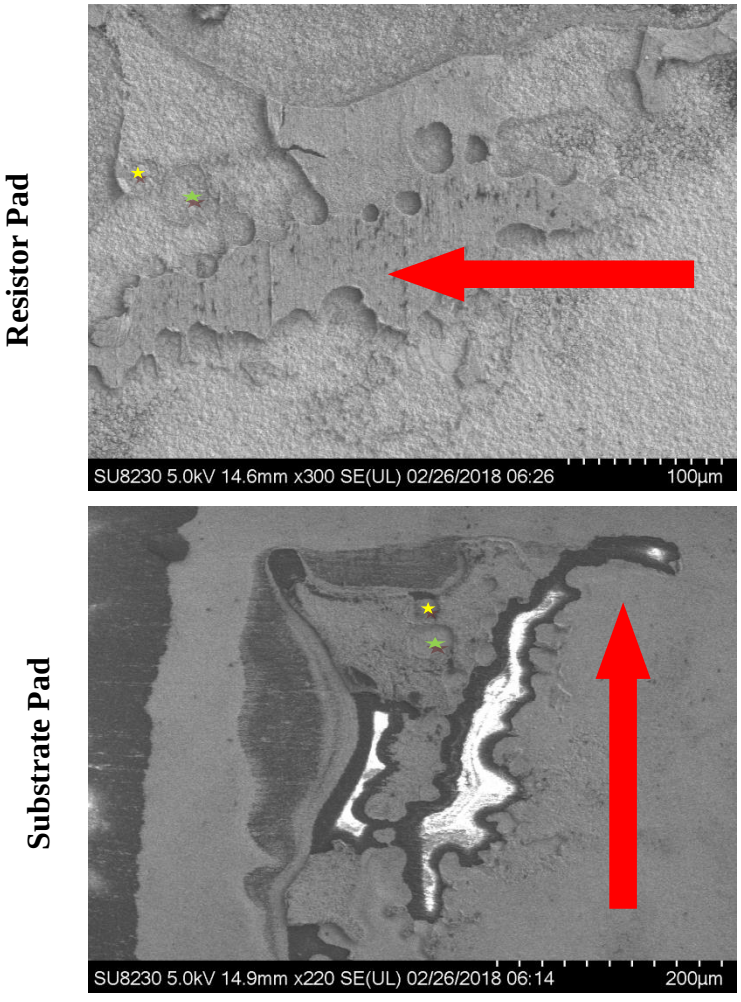

Figure 87: SEM images of resistor pad and substrate pad (a) Resistor pad showing Ag (b) Substrate pad showing LCP. Assembly placement force was 0.2 N. Sintering time was 45 min. EDX was done to ensure the identification of the interfaces; the red arrow corresponds to shear directions and the stars are to help orient how the resistor and substrate sides were sandwiched together.

Figure 87a shows the resistor pad and Figure 87b shows the substrate pad. The images were taken after the shearing was completed. The images pertain to an assembly placement force of 0.2 N and an assembly sinter time of 45 min at 200 °C. As observed, Ag was still adhering to the resistor pad, while bare LCP was visible on the substrate pad indicating all the Ag had been sheared away from that location during the die shear test. This result is somewhat like what is presented in Figure 86, where a larger portion of the bare LCP was seen on the substrate pad side. It should be emphasized that Figure 86 corresponds to a larger placement force of 5.0 N, while Figure 87 corresponds to a lower placement force of 0.2 N. The images in Figure 85 and Figure 86 confirm that with the larger placement force, the joint strength was greater than the adhesion strength of Ag ink to LCP. In the die shear tests, as discussed earlier, the shear head was kept sufficiently low to the substrate to minimize moment effects on the shearing area.

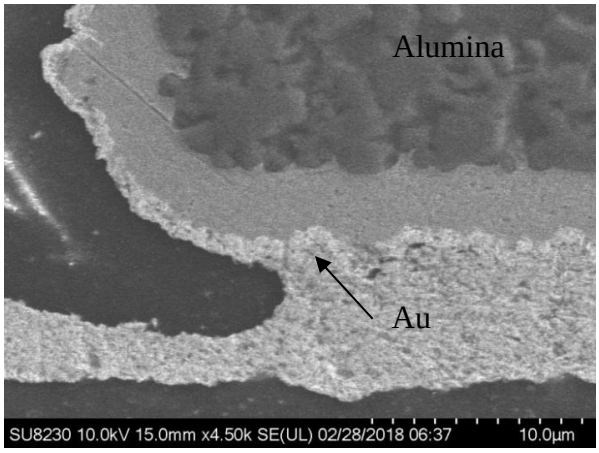

Figure 88: SEM of cross-section of the 1.0 N placement force for 60 minutes

Cross-sectioning checked the quality of joint upon assembly, prior to die shear testing. Figure 88 shows an alumina resistor with Ni/Au pad adhering to Ag in the joint and the trace printed on top of LCP. The total thickness of Ag is about 6 µm with 4 µm for the initial trace with two layers and 2 µm additional ink added for assembly purposes. As seen in the cross-section, the Ag ink did wet the resistor pad.

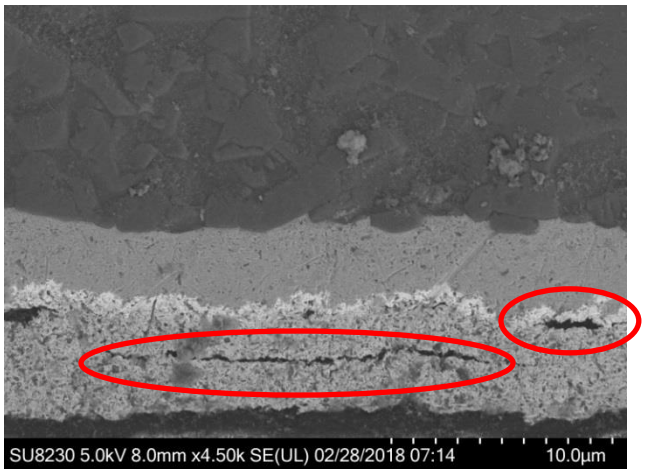

Figure 89: Cross-section of 0.5 N force at 60 min in oven at 200 °C shows that the ink did not always fuse with the Ag trace.

In another assembly, done with 0.5 N placement force with 4 printed layers, the Ag from the initial trace and Ag from the subsequent joint did not fuse together during the assembly sintering process as well as sections of the resistor pad Au to the Ag ink, as shown in Figure 89. It is problems involved in terms of printing stations and assembly stations.

1.23.2 Case 2: Number of passes and placement force variable

For case 2, the study parameters are the number of passes for the printed pads and the placement force during assembly. After assembly, resistance measurements were taken to determine if the joints performed well electrically. Next, die shear testing was done to compare the strength of the joints on XYZTEC^{TM}. The die shear testing was done at a 100 μm/s shear rate.

The resistance was measured after assembly and Figure 90 outlines the results. Whenever the measured resistance was close to 50 kΩ, those assemblies were considered good. Incomplete wetting and bonding of the printed pads to the resistor would result in the open circuit having resistance extremely higher than 50k. Bridging of the printed ink underneath the resistor would result in the closed circuit would have resistance extremely lower than 50k.

Ten samples were assembled with different sets of process and assembly conditions. As seen from rows 1 through 3, the assembly mostly shorted when 8 layers of ink were printed. The shorting was particularly severe when the placement force was high (e.g. 10 N or 5 N). This is to be expected because with the higher bonding force, the ink would squeeze and bridge creating a short circuit.

Although 2 and 4 layers yielded good electrical connections, as seen later, the 2-layer assembly did not have enough shear strength. Also, it was hypothesized that the 6 layers could yield better assembly if the force were to be reduced. Thus, the next sets of assemblies were conducted with 4 and 6 layers.

For the following electrical result layouts, the coloring legends are as follows:

- The yellow "No assembly" means no assembly was attempted.
- The blue "Open" means the component did not stick or bond to the substrate. Even if it was bonded, the circuit showed infinite resistance.
- The red "Short" means that the ink pads merged together under the component.
- The green "good" means that the assembly was electrically good indicating that the measured resistance was close to 50 kΩ. Electrically good connection does not mean the shear strength of the assembled interconnect was good.

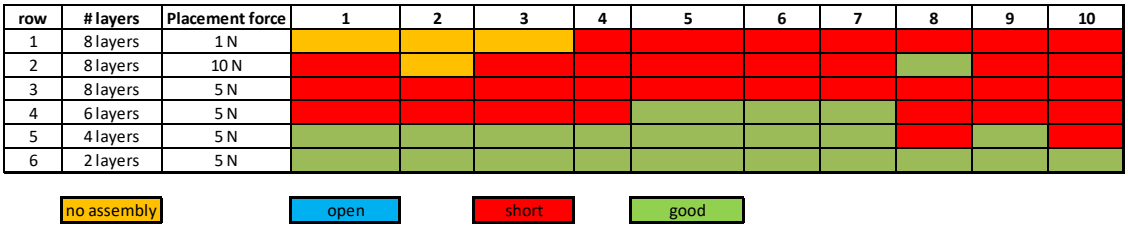

Figure 90: Electrical testing of connection for varying the number of layers on the pad

In Figure 91, the horizontal axis shows the number of layers and the applied placement force, while the vertical axis shows the maximum shearing force as measured in XYZTEC^{TM}. At the first instance, it appears that 8 layers with different placement force will be beneficial for providing high die shear force. However, while considering the electrical test results presented in Figure 90, the 8 layers usually resulted in shorting of the circuitry. This shorting would mean that the ink had squeezed under the bottom of the

device, and ink from both endpads had merged. Also, this ink squeezing touches the bottom of the device along its entire length. In other words, the device is bonded to the substrate all the way from one end to the other end, not just at the pads. Therefore, the measured die shear force is also due to the larger bonding area of the device to the substrate, and thus, the results for the 8 layers samples are not comparable for the shear force results. Looking at the remaining data and in conjunction with the electrical test results, it appeared that 4 layers would be a viable candidate, and examination of 6 layers with a lower placement force was warranted.

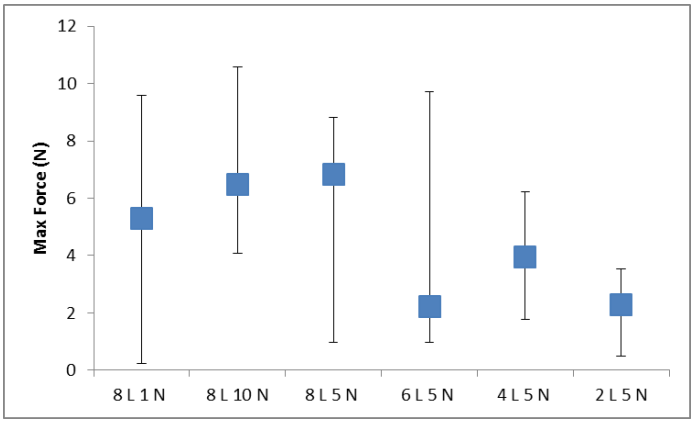

Figure 91: Plot of the average measurement

In the plot of Figure 91, the average for each row is the blue square and the bars indicate the maximum and minimum measured. For the 8 layer samples with different placement force, there is no clear indication of benefit for increasing the force because additional material holds the resistor in place where the electrical shorting occurs. For the 6 layers could potentially be optimized for higher strength compared to the 4 or 2 layers. The shear force for 2 layers appears much lower than the values obtained for other cases.

For case study 2, it is important to note that the pad design changed so that the pads extend beyond the resistor's pad in addition to extending on the inside as shown in Figure 92. This modification is to allow more volume of the liquid to be available, and to have a greater tolerance during alignment in the flipchip bonder. Figure 93 shows the LCP side after the shearing experiment. As seen, the printed pad is present half on the LCP and the other half of the printed pad has been sheared off with the resistor pad.

Figure 92: Pad layout change, traces shorter and pads closer together

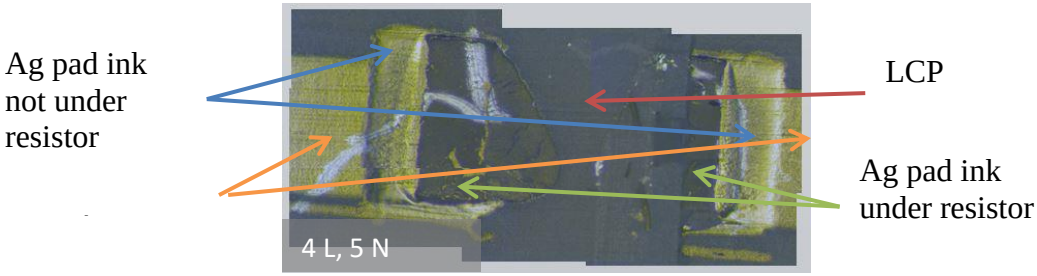

Figure 93: LCP Substrate after shear

SEM imagining was done on both the resistor and the substrate side after the shear testing. The first set of images corresponds to the resistor side after shear testing. During the imaging of the resistors, it is apparent there was ink attached to the alumina as shown in Figure 94. This figure is the bottom center of the resistor with 6 layers and 5 N placement force. As seen, part of the printed silver is at the bottom of the alumina resistors because the ink that squeezed under the resistor and bonded the resistor bottom to the substrate. The

"short" electrical measurement and the very high shear force (9.73 N) also support this conclusion. Another image of the same sample near the resistor edge shows that Ag has transferred to ENIG resistor pad, indicating that the Ag has bonded on the pads as well as along the resistor.

On the ink sections, strands of the LCP might have attached to the resisters with high shear results. The resistor main attachment to the LCP side can be seen on the edges of the resistor pad areas as shown in Figure 95.

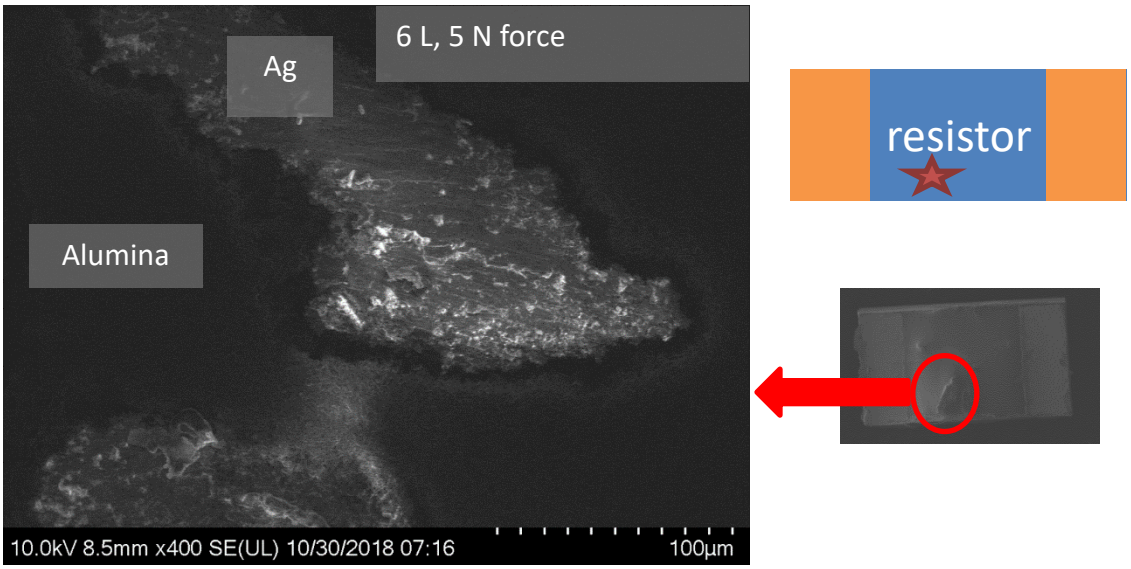

Figure 94: Not as much ink in the center of the resistor, Suspect LCP attached to areas with the ink

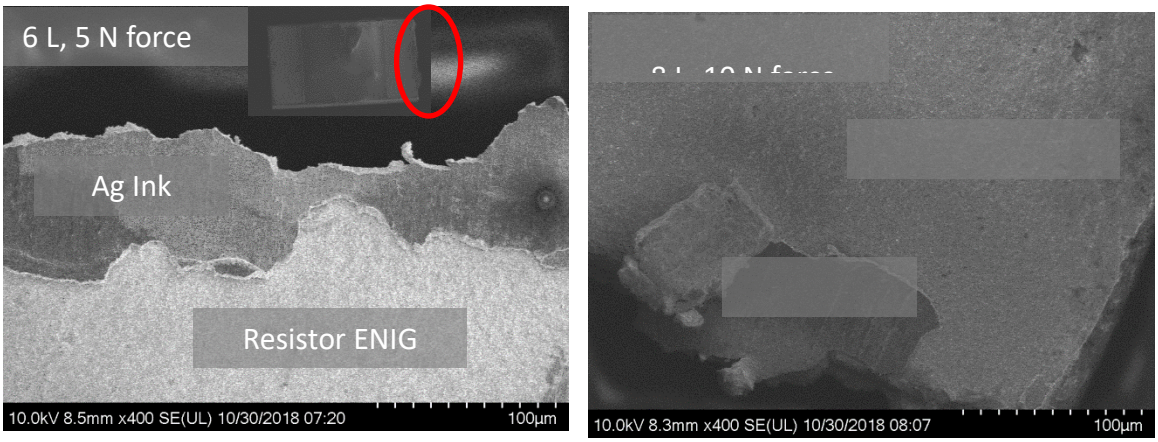

Figure 95: Edges are more distinct areas for the resistor

Most of the fracture occurs in the interface between particles as seen in Figure 96 SEM images. In other words, for inkjet-printed silver inks, the fracture is inter-particle in nature, rather than intra-particle, matching expectations.

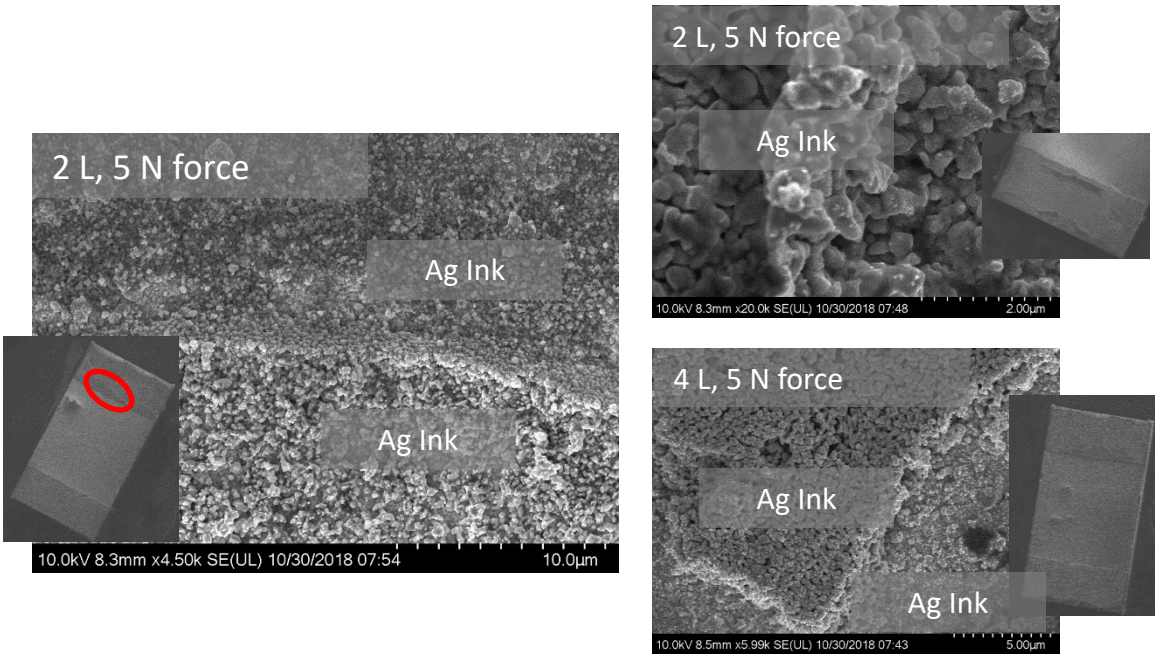

Figure 96: Shearing between particles for printed ink

Trace layers first undergo sintering right after they initially printed and sintered. At the time of assembly, the substrate pads were printed and then the component was placed, and the entire assembly was sintered again. This means that the printed traces go through sintering twice, while the substrate pads go through sintering only once. Upon shear testing and SEM imaging, it is seen that the trace silver ink, twice sintered, showed higher densification, while the pad silver ink, once sintered, showed relatively porous structure, as shown in Figure 97.

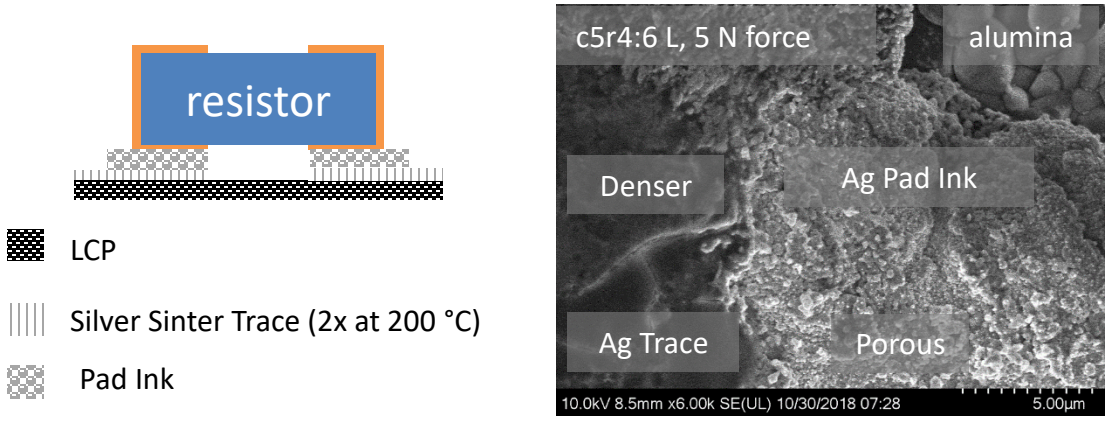

Figure 97: (a) Schematic (b) A few areas on the resistor demonstrated the coarser grain area

The following SEM images show the substrate side with varying number of layers and placement force done. For the substrate side, the spreading ink is more noticeable for the shorted the samples with 8 layers and the 1, 10, and 5 N placement loads (Figure 98, Figure 99 and Figure 100). Sections of LCP are clear in the sections of the resistor edge pads. Also, alarming is the more textured section of the 2 L traces which look to have cracks forming in Figure 98.

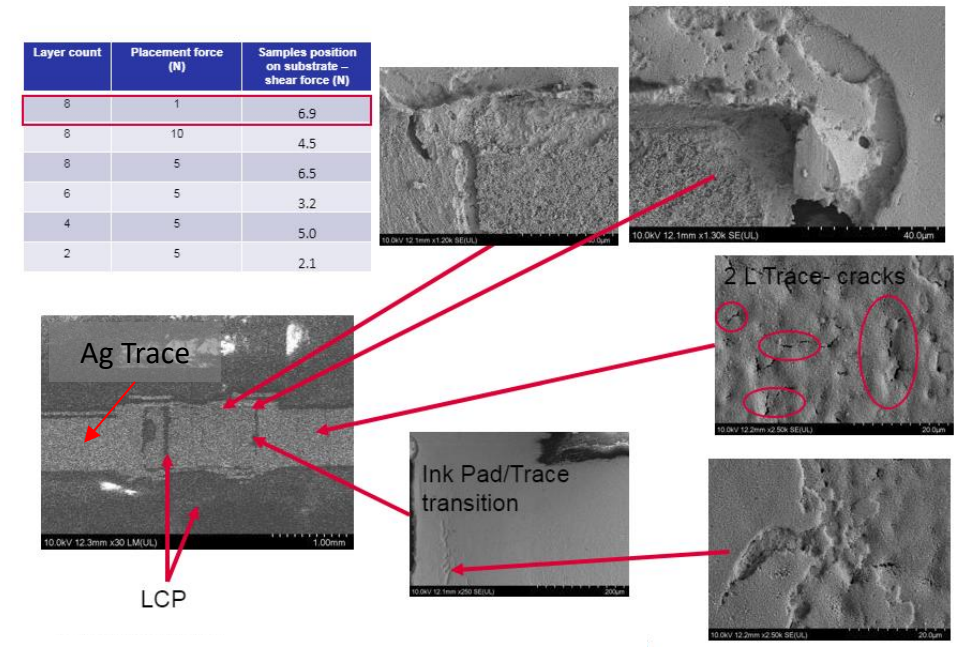

Figure 98: Substrate side for the 8 layers count with 1 N placement force

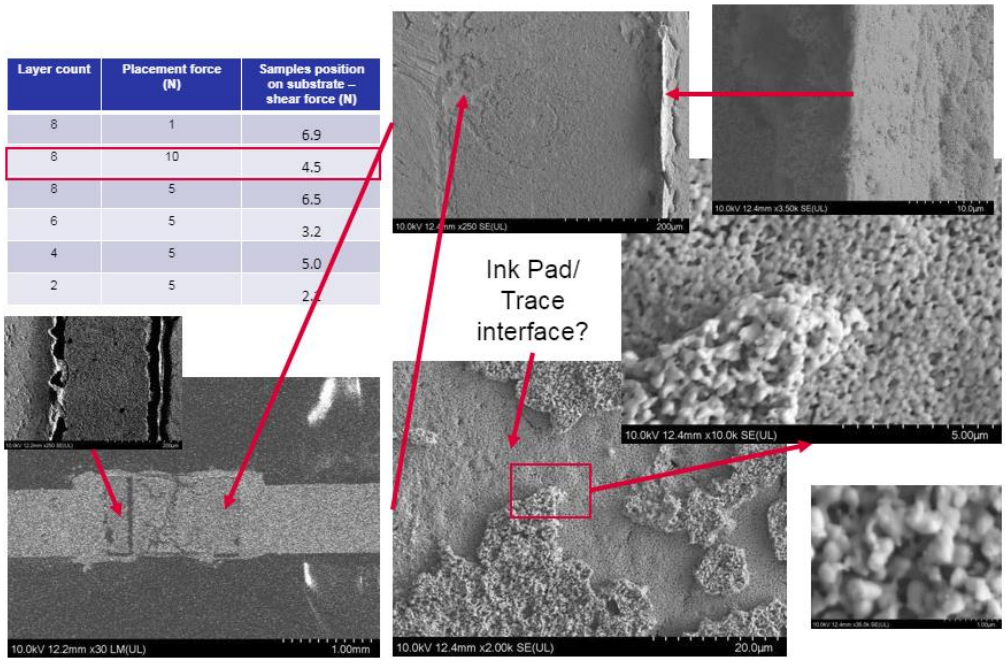

Figure 99: Substrate side for the 8 layers with 10 N placement force

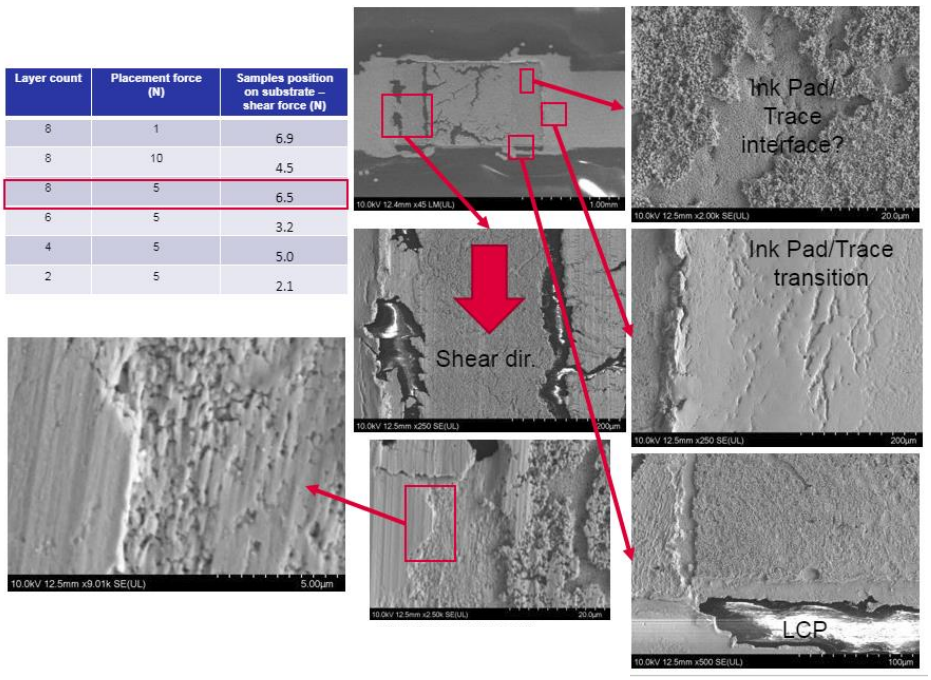

Figure 100: Substrate side for the 8 layers with 5 N placement force

For the 6 Layer, 4 Layer and the 2 Layer substrate sides, the images capture that the ink still spreads with the indicated placement force, but do not connect (Figure 101, Figure 102, and Figure 103). The ink prefers to wick to the edges, and this is where it looks to be where the main contact. Again all the pads on the substrate side have sections of LCP revealed, even with the 2L and 1 N case.

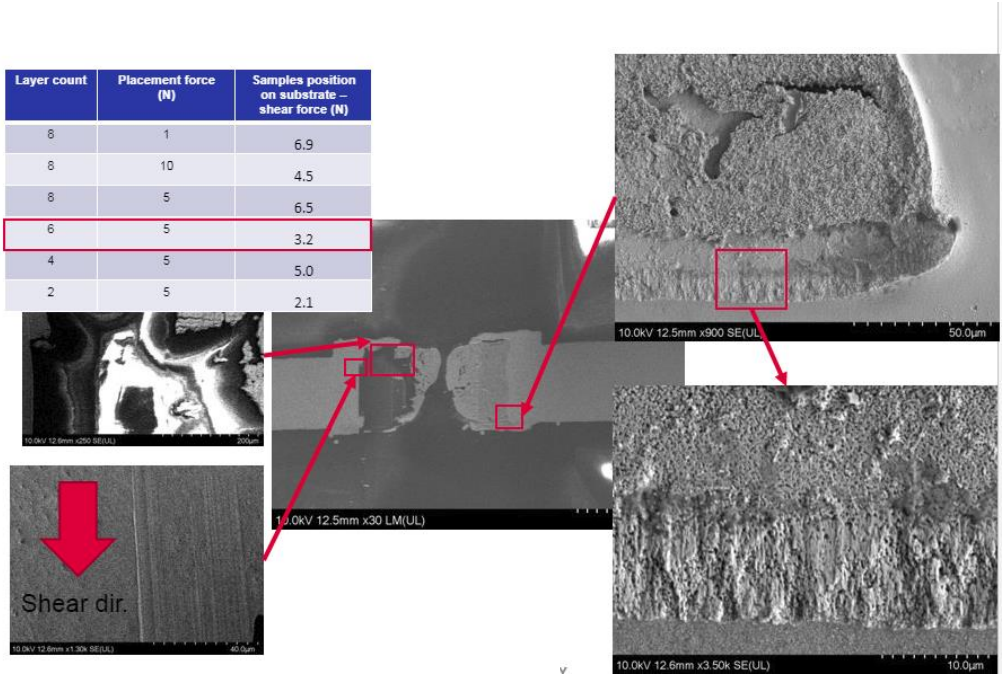

Figure 101: Substrate side for the 6 layers with 5 N placement force

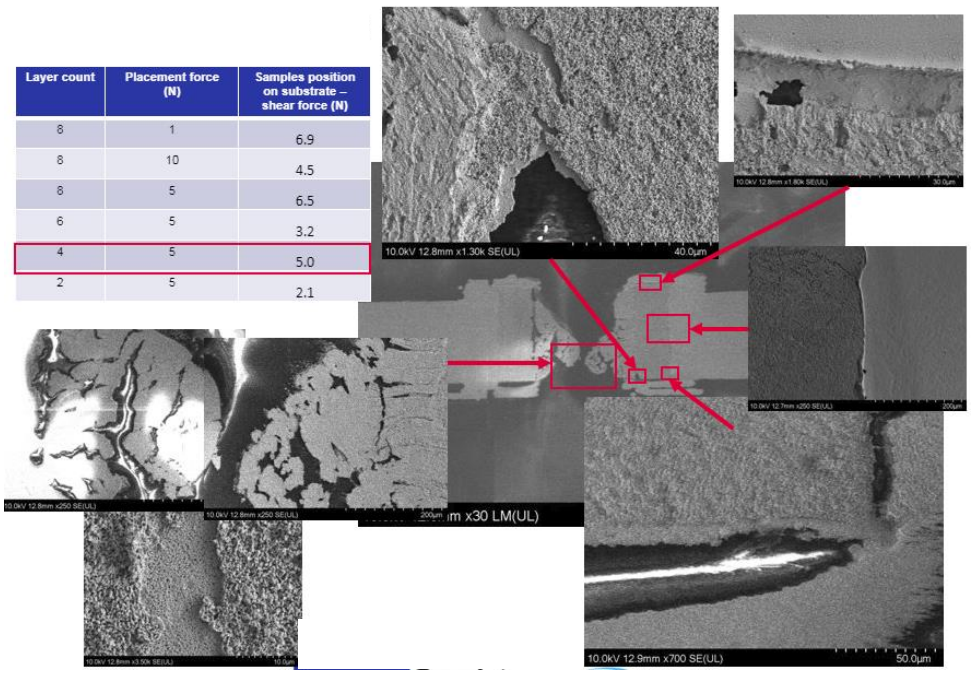

Figure 102: Substrate side for the 4 layers with the 5 N placement force

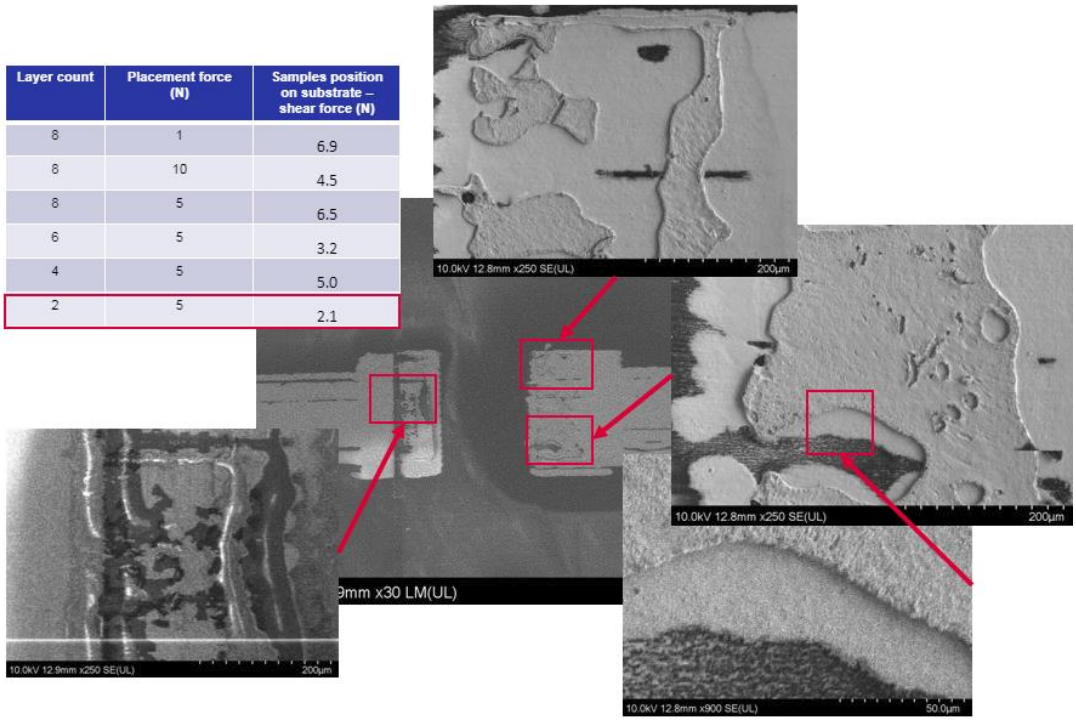

Figure 103: Substrate side for the 2 layers with the lowest shear strength values

The 2 layers obtained adequate wetting; however, the true strength of the joint cannot be determined with the results. As next steps, either a UV ozone clean needs to occur before printing in order to strengthen the adhesion of the ink to the LCP or printing on metal needs to be tested for assembly evaluation. SEM and EDS cross-section images showed how the joints formed; however, the cross-section image did not reveal as clear detail as case 1, due to polishing issues.

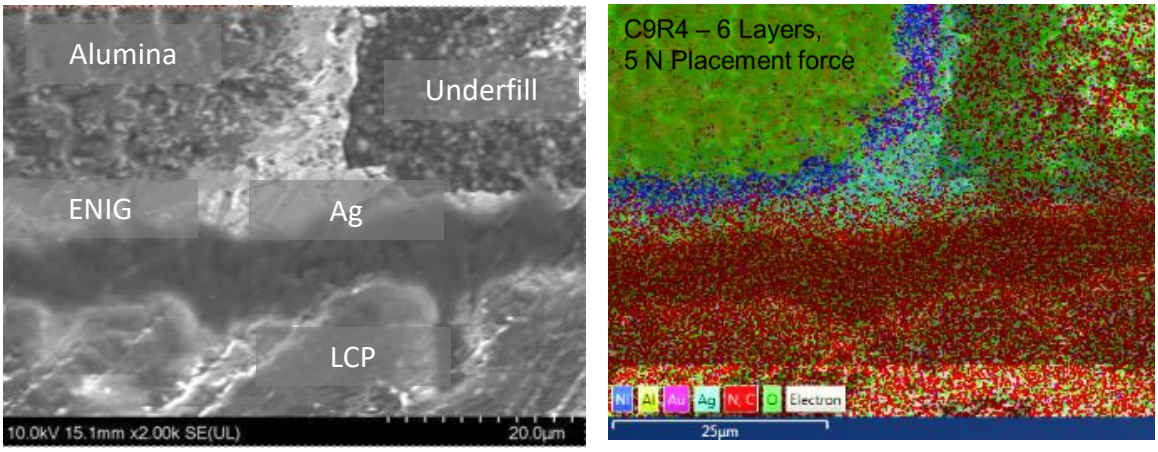

Figure 104: Cross-section sample to examine the Ag ink on the sidewalls with the pad extended (b) EDS to verify the element id

1.23.3 Case 3: Number of layers and applied placement force (1 or 3 N)

For case 3, the number of layers (4-6) and two different placement forces (1 or 3 N) were examined. This case is after printed. There were multiple printing difficulties for this case. Sometimes, the .dxf file had problems converting into a bitmap file. Other times, the ink jets droplets during from the drop watcher were not short.

	# layers	Placement force	1	2	3	4	5
1	4 layers	3 N					
2	4 layers	C1:1N, C2-5:3 N					
3	4 layers	1 N					
4	6 layers	3 N					
5	6 layers	1 N					
6	4 layers	1 N					

no assembly | open | short | good

Figure 105: Electrical testing of the wider spacing between the pads and looking at 4 and 6 layers for the pads

Figure 105 shows the results for 4 and 6 layers. In the placement force column, the designation of C1 is that for row 2, column 1 has a placement force of 1 N, while the C2-5 means that columns 2 through 5 on row 2 have placement force of 3N. As seen, 6 layers produced good electrical connection when the force was reduced from 5 N (row #4, Figure 90) to 3 N and 1 N, as illustrated in rows 4 through 6. Also, 4 layers produced mostly good electrical connection results.

Die shear testing was done to compare the strength of the joints on XYZTEC^{TM} as shown in Figure 106. The die shear testing was done at a 100 μm/s shear rate. For this study, the best results came from the 6 layers with 3 N placement force, but the force values were on the lower side. One possible reason for the low force is that the printing had a poor process control resulting in low dots per inch (dpi). Thus, although the substrate was UV ozone treated, the lack of process control during printed resulted in low shear force values.

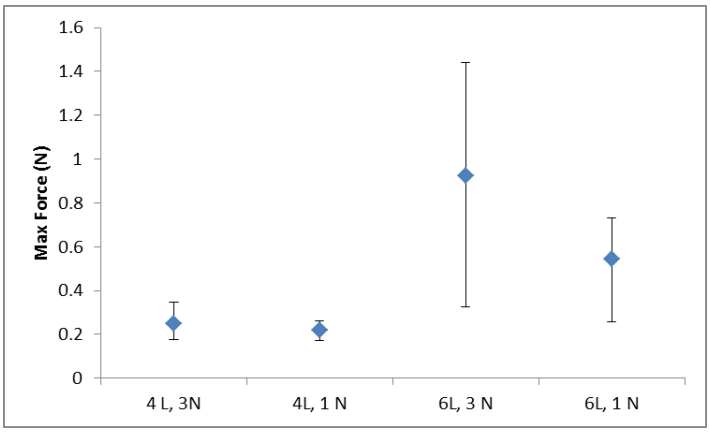

Figure 106: Maximum force for case 3

For case 3, only optical microscope imaging was done to examine the failure are of the shear tests. For all the cases, the shear maximum force was very low and the coverage of the ink on the pad was not good as shown in Figure 107, Figure 108, and Figure 112. As

mentioned earlier, it is in this test case that a better understanding was developed about the printer, and the printing issues were resolved to be able to pursue the next set of experiments with 6 layers and 3 N force.

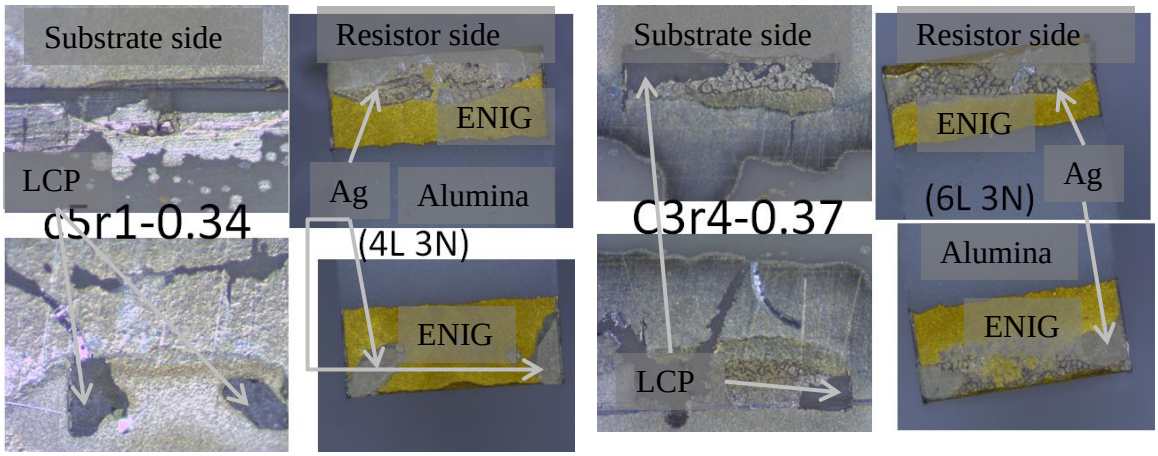

Figure 107: For case 3 4 layers (3N placement) maximum force measured for all the 4 layer pads, 6 layer 3N min

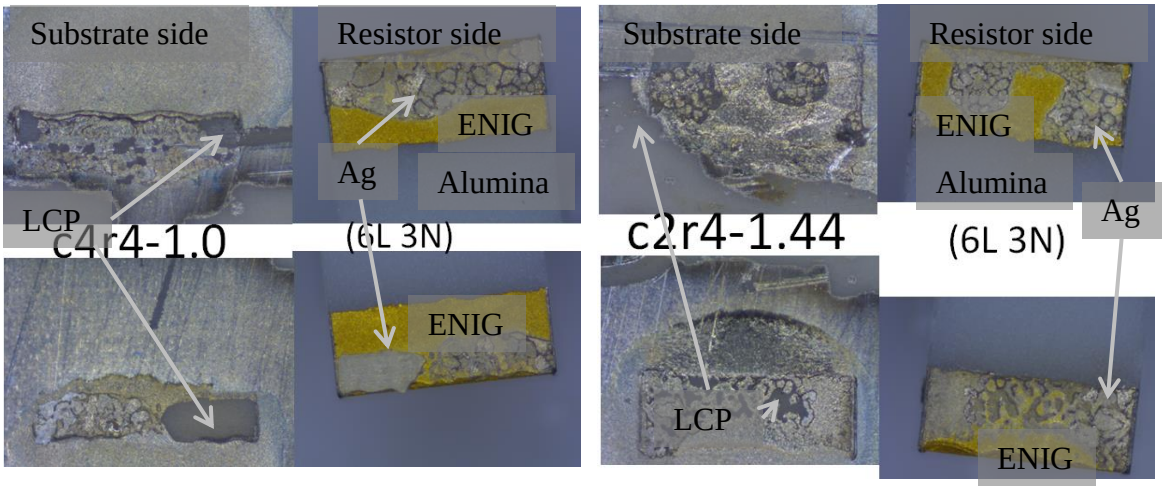

Figure 108: Max force measured for 6 layers and 4 N placement force for test case 3

1.23.4 Case 4: Role of fixturing in shear force measurements

For case 4, fixturing as shown in Figure 109 is explored to see if there was a noticeable difference among samples which were not restrained (no tape) during assembly, taped only during device placement, and taped during placement and sintering. For this case, the pre-clean treatment was acetone, IPA and ozone clean. Care was taken during calibration with the drop watcher to ensure the timing and uniform size for neighboring jets.

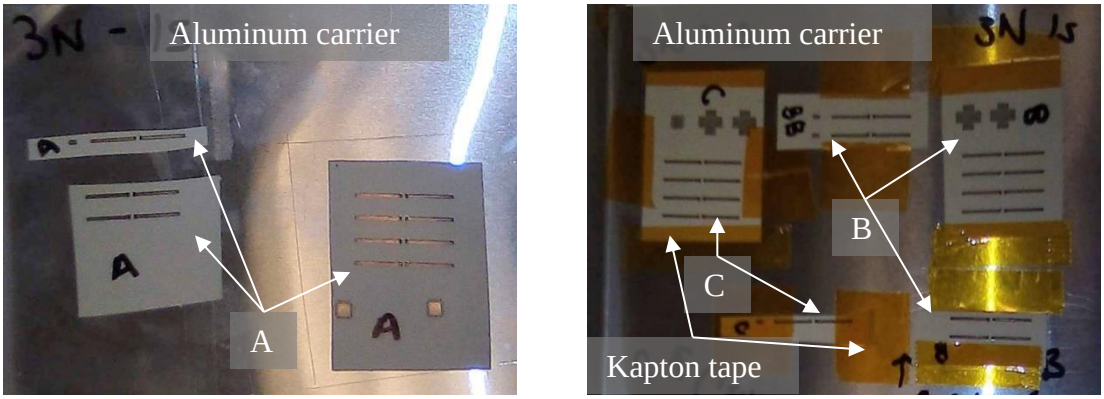

Figure 109: Fixture samples (a) no tape, (b) tape only placement and (c) tape during placement and sintering

When the substrate is placed with a placement force and the subsequent assembly is carried out at a high temperature without a bonding force, the planarity of the substrate plays a role in the quality of the assembly. Therefore, for the next set of experiments, the substrate was adhered to the platform with a tape for some of the cases, and the results are shown in Figure 110.

	# layers	Placement force	Fixturing	1	2	3	4
A1	6 layers	3 N	No Tape				
A2	6 layers	3 N	No Tape				
A3	6 layers	3 N	No Tape				
B1	6 layers	3 N	Tape (Placement Only)				
B2	6 layers	3 N	Tape (Placement Only)				
B3	6 layers	3 N	Tape (Placement Only)				
C1	6 layers	3 N	Tape (Placement&Sintering)				
C2	6 layers	3 N	Tape (Placement&Sintering)				

no assembly | open | short | good

Figure 110: Electrical Testing of the different timings of tape to fixture the sample

Die shear testing was done to compare the strength of the joints on XYZTEC™ as shown in Figure 111. The die shear testing was done at a 100 μm/s shear rate. In Figure 111, the horizontal axis shows the fixturing type, while the vertical axis shows the maximum shearing force as measured in XYZTEC™ assembly and sintering. As seen, the number of layers and the placement force controlled the shear force, rather than whether the substrate was taped or not during the assembly process.

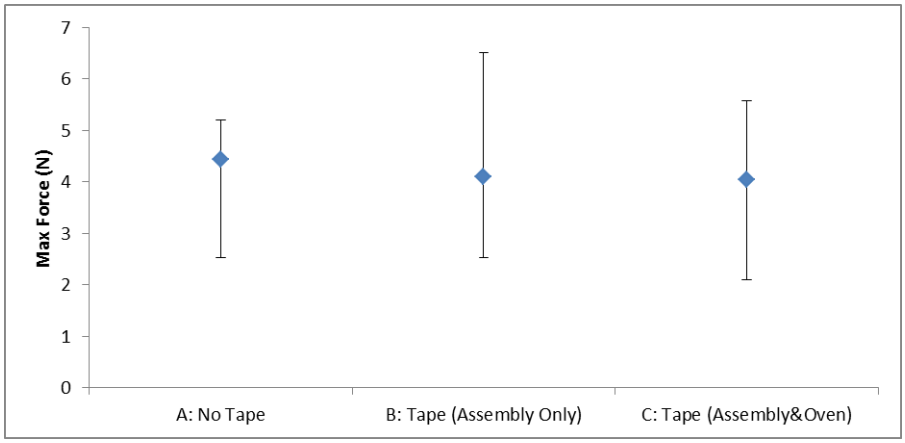

Figure 111: Case 4 plot of average, max and min max force

For case 4, microscope images were taken of the whole area pad of the substrate and the resistor pads to examine the ink coverage. For each case only the maximum and minimum force measurements are shown in Figure 112, Figure 113, and Figure 114. In almost all the substrate side images, LCP sections can be seen in the pad section. All the samples exhibited spreading in the section under pressure; however, there was no apparent spread of the pad ink in the section not under the resistor. A greater section of LCP was revealed for the higher loads measured. This lead to the conclusion that, in order to achieve higher numbers, preparation of the LCP substrate before ink printing ought to be prioritized over the studying the type of fixturing in assembly and in the oven of the substrate [26]. Often, for organic to metal interface, the mechanical interlocking is more dominate, and so roughening the surface could help. Based on this detailed study, it appears that 6 layers with 3 N will be a viable method for the assembly.

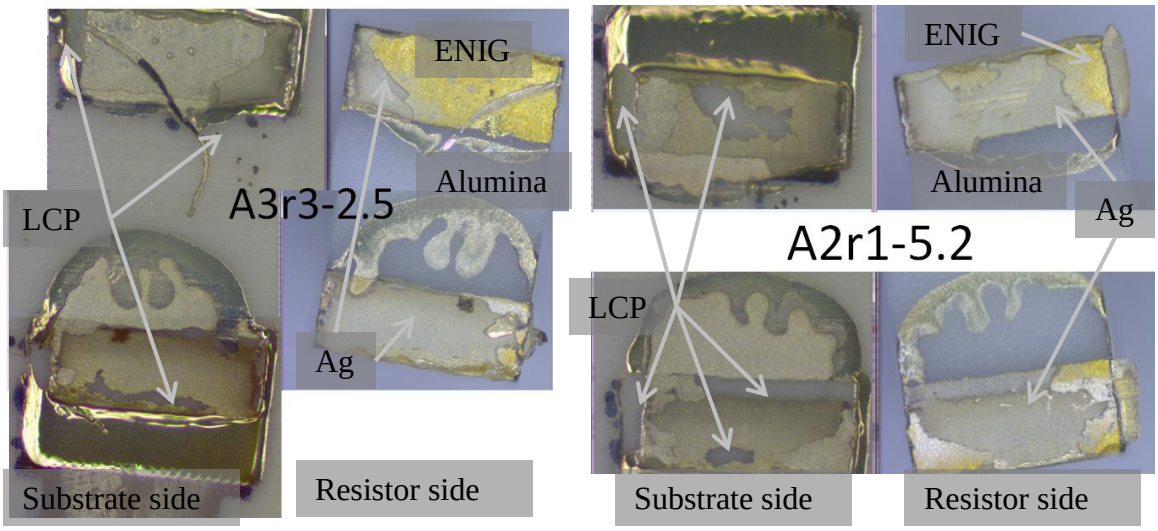

Figure 112: Dark-field microscope images of the substrate and resistors for Type A: No fixturing during placement or sintering in the oven (a) min (b) max

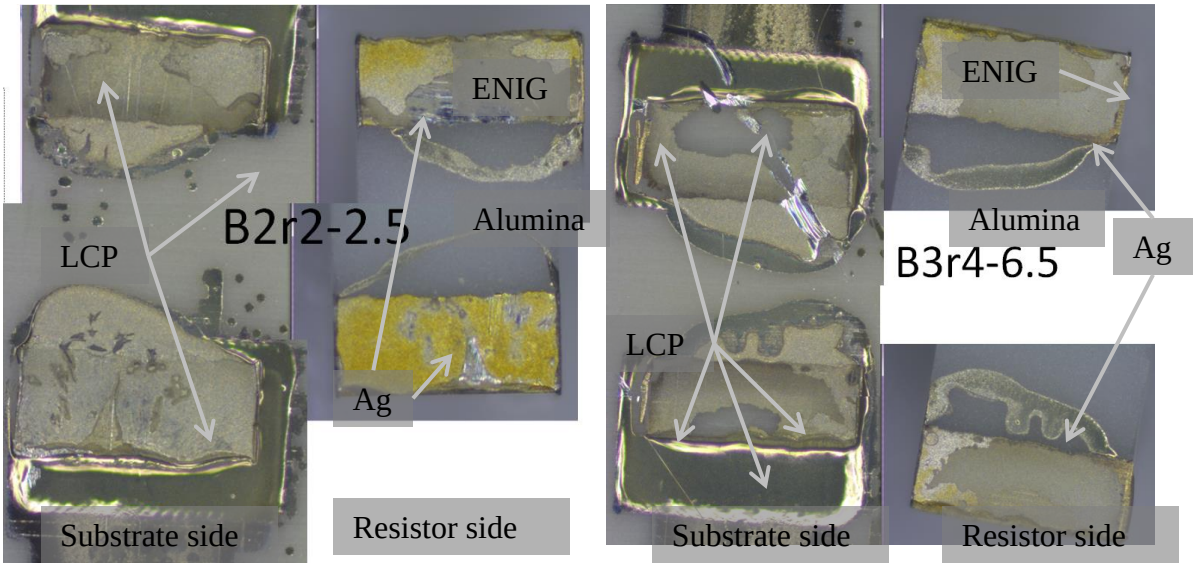

Figure 113: Dark-field microscope images of the substrate and resistors for Type B: Tape only during placement (a) min (b) max

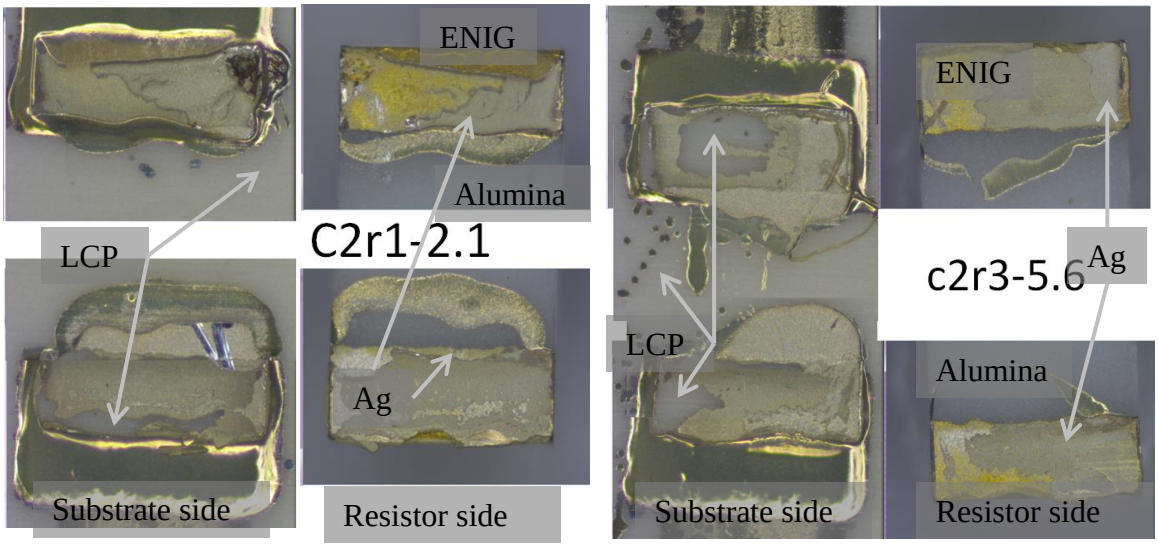

Figure 114: Dark-field microscope images of the substrate and resistors for Type C: substrate taped during placement and sintering in oven(a) min (b) max

Die shear testing was done to compare the strength of the joints on XYZTEC™ as shown in Figure 120. The die shear testing was done at a 100 μm/s shear rate. The

horizontal axis shows the applied placement force, while the vertical axis shows the maximum shearing force as measured in XYZTEC^{TM}.

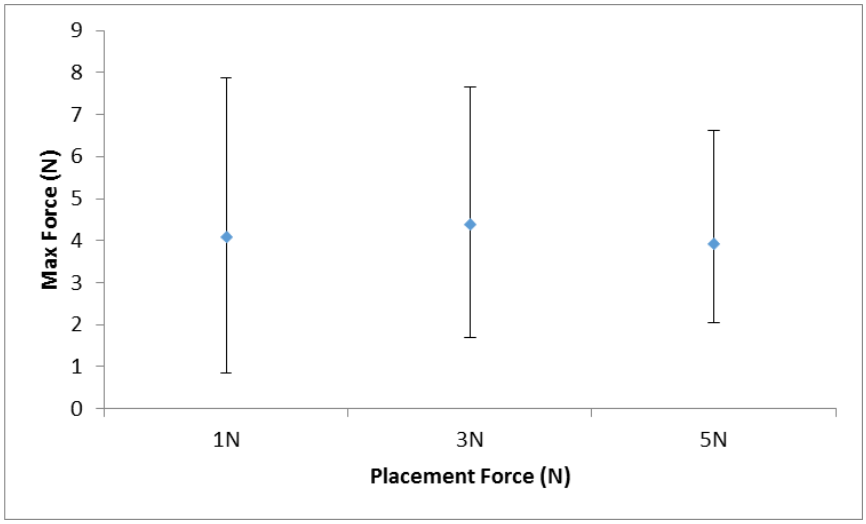

Figure 115: Force measurements

This shear force data set was also higher than the forces seen for cases 1, 2, 3, and 5. All of these indicate that the processing control of the ink during printing is a major factor on the joint shear strength. Figure 116 shows how the values of shear strength when using the entire pad areas for the calculations.

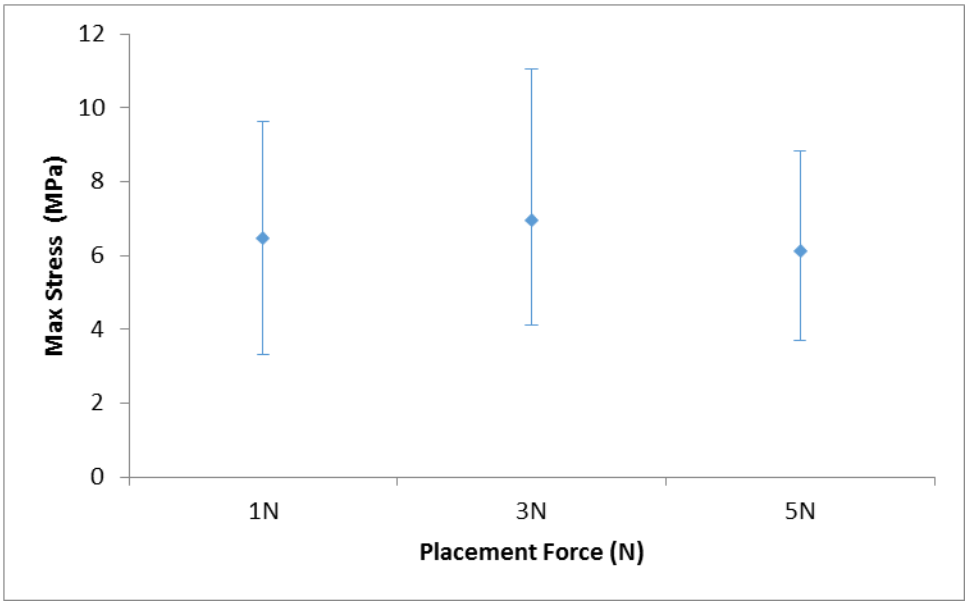

Figure 116: Max stress calculated from the max force divided by the area of the pads

1.24 ENIG studies to isolate joint measurements

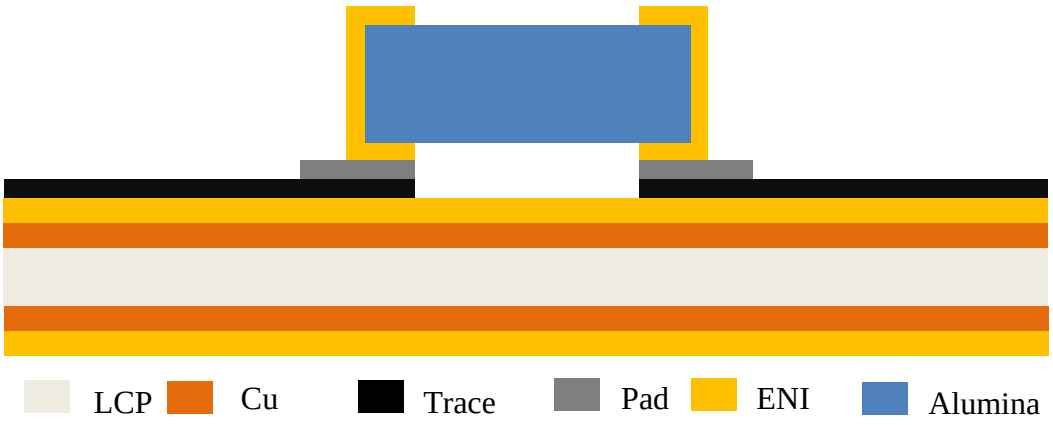

Figure 117: Substrate with ENIG processing

To help isolate the joint, a couple of the samples' Ag traces were printed onto an ENIG surface as shown in the new cross-section of Figure 117. The ENIG was pursued for the substrate level as well due to the before mentioned adhesion strength of a metallurgical bond. Initially, the substrate was a Cu clad LCP and is blanket coated by ENIG processing. The ENIG was processed in-house, and the details of the procedure mentioned in APPENDIX B.

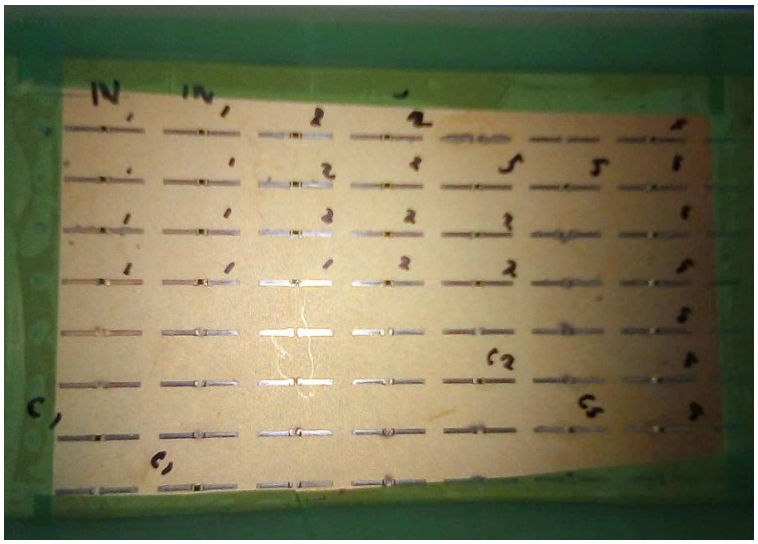

ENIG Cu clad LCP

5 min Ozone clean

2 Layers traces printed

Oven for 30 mins at 200 °C

Print Pads (# layers 2, ~~4~~, ~~6~~)

Place Resistor (Placement force: 1,2,5 N)

Oven for 30 mins at 200 °C

Figure 118: ENIG process flow and the final assembled result

After the additional layers from ENIG processing, the same process flow was followed: (1) deposition of the traces, (2) sintering the traces at 200 °C for 30 mins, (3) printing the pads, (4) transfer the substrate to assembly lab, (5) assembling the resistor, and (6) sinter in oven at 200 °C. However, since the ENIG was a blanket coat, there was no a masking layer, which made electrical measurements mute.

Table 15: Case descriptions

Case	# passes	Placement Force	Oven time	Shear testing rate	Fixturing
5	2	1, 3, 5	30 min	100 μm/s	ENIG tape
6	6	1,3,5	60 min	100 μm/s	ENIG No tape

For the initial ENIG board, traces with 2 passes were printed onto the ENIG with 5 min ozone clean. After sintering in the oven at 200 °C for 30 mins, the pad layers were printed. However, for the intended 4 and 6 layers pad passes, shorting occurred while waiting for the print to dry. For the original direction, the ENIG were thought to wet too well, but later it was determined that the printer settings needed better calibration to provide the better resolution precision. Therefore, the initial study was conducted with only 2 passes for the pad layer, not the 4 or 6 layers initially planned due to shorting issues. Placement forces of 1 N, 2 N, and 5 N were used for the 2 layers. Due to location differences of the printer and the assembly lab, ink dry time was not a controllable factor. After device placement, the joints were sintered in an oven at 200 °C for 30 mins. This process flow is recapped in Figure 118.

1.24.1 Case 5: Applied force on ENIG substrate on 2L

For case 5, the traces were printed onto an ENIG substrate that was pre-cleaned with acetone and IPA followed by a 5-minute UV ozone clean. Three different placement forces were applied on the resistor during assembly: 1 N, 2N, and 5N. Die shear testing was done to compare the strength of the joints on XYZTEC^{TM} as shown in Figure 119. The die shear testing was done at a 100 μm/s shear rate. In Figure 119, the horizontal axis shows the applied placement force, while the vertical axis shows the maximum shearing force as measured in XYZTEC^{TM}. As seen, the die shear forces were generally below 2 N, which

was on the lower side from the previous studies. This went against the idea that the ENIG surface would produce a stronger ink connection. Further literature review revealed the diffusion from Au to Ag is higher than from Ag to Au as well as Ag to Ag [52]. If there was not enough Ag available, voids will form at the Ag/Au interface. This will weaken the interfacial strength. Therefore, in the next set of experiments (case 6), more Ag layers were deposited onto the substrate pad making sure that there will not be any shorting upon device placement with force.

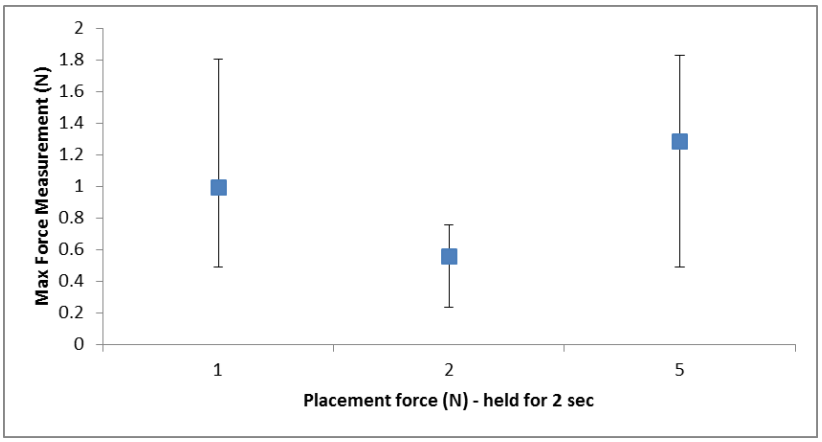

Figure 119: ENIG results with 2 Layer passes

1.24.2 Case 6: Applied force on ENIG substrate

For case 6, three different placement forces (1, 3 and 5 N) were examined on traces printed on ENIG substrate with 6 layers printed on the pad. For this case, particular care was taken during calibration with the drop watcher. This time, it was determined that 6 layers could be printed in the pad by ensuring only 2 jets with good jetting shape.

Die shear testing was done to compare the strength of the joints on XYZTEC™ as shown in Figure 120 and Figure 121. The die shear testing was done at a 100 μm/s shear

rate. In Figure 120, the horizontal axis shows the applied placement force, while the vertical axis shows the maximum shearing force as measured in XYZTEC™.

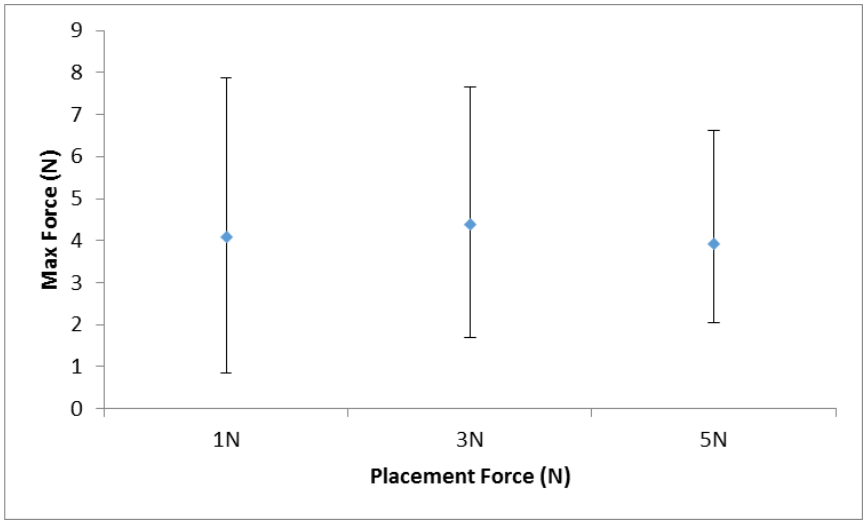

Figure 120: Force measurements

As a whole, this shear force data set is also higher than the forces seen for cases 1, 2, 3, and 5, and the average shear force value was similar to the values in case 4. All of these indicate that the processing control of the ink during printing is a major factor on the joint shear strength.

	# layers	Placement force	1	2	3	4	5	6
1	6	C1-2:1N,C3-4:3 N,C5-6: 5N	0.84	4.45	5.73	1.70	3.11	4.92
2	6	C1-2:1N,C3-4:3 N,C5-6: 5N	7.87	2.06	5.94	2.71	2.05	3.98
3	6	C1-2:1N,C3-4:3 N,C5-6: 5N	2.31	3.40	3.86	2.58	5.46	2.29
4	6	C1-2:1N,C3-4:3 N,C5-6: 5N	3.57	5.96	6.85	7.67	2.98	
5	6	C1-2:1N,C3-4:3 N,C5-6: 5N	4.40		4.34		3.85	
6	6	C1-2:1N,C3-4:3 N,C5-6: 5N	5.91		2.54		6.62	

no assembly cross-section fell off

Figure 121: Measured shear force for case 6

1.24.3 ENIG substrate discussion (applied force on ENIG substrate)

When examining the 2 layers on ENIG shear results with dark-field microscopy, the poor wetting of material was again observed as shown for the different placement forces in Figure 122. In Figure 122, it was also noticeable that the ENIG does not appear in the pad area of the trace, and indicated that the ENIG to the Ag trace was stronger than the LCP adhesion to the Ag trace. It was important to understand the mechanisms for the spread of the pad printed layer occurs. The current volume of 2 passes was not enough for assembly purposes, which was the conclusion from the first case study. The 2 passes was only pursued for case 5 due to printing issues of the ink spreading

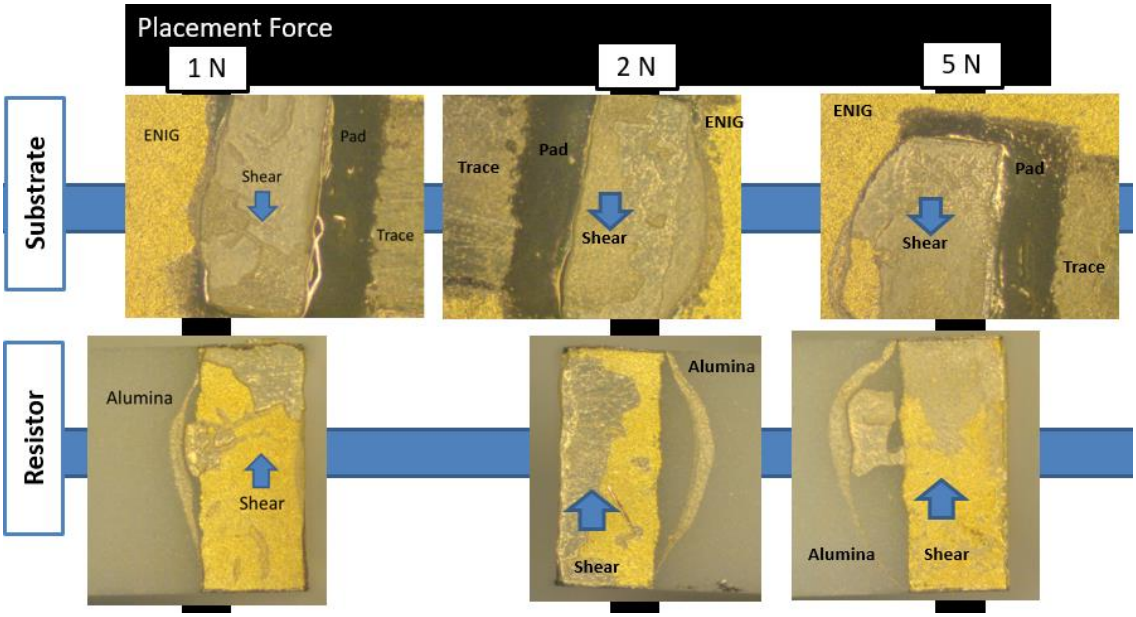

Figure 122: Dark-field images of the substrate and the corresponding resistor side

For case 6, the 6 layers printed on the pad did not appear to spread like the initial case 5 ENIG printing. Figure 123 shows how the values of shear strength if using the entire pad areas for the calculations.

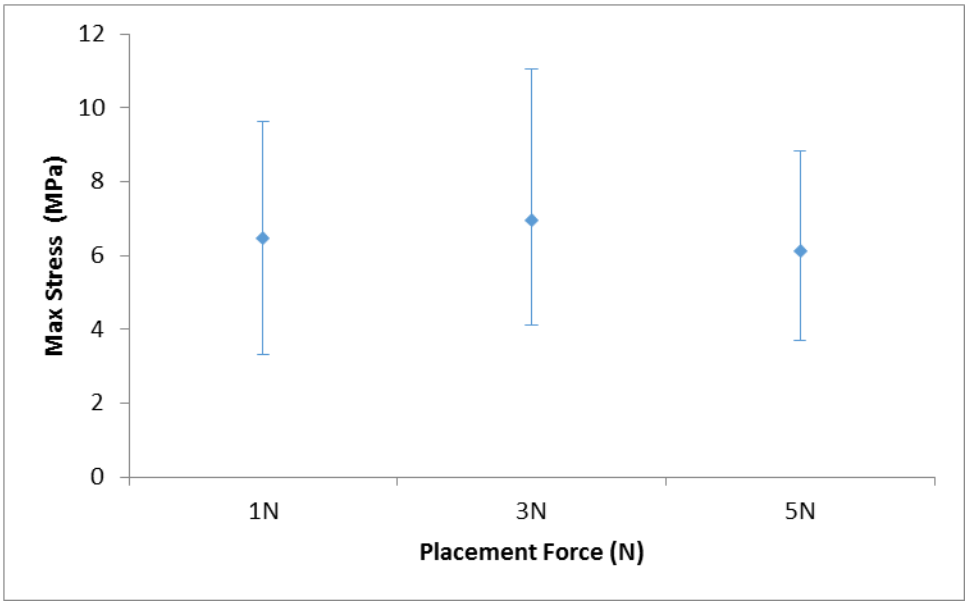

Figure 123: Max stress calculated from the max force divided by the area of the pads

1.25 Assembly Conclusions

For this chapter assembly of 603 resistors using a fully-ink process was examined and demonstrated with 603 resistors. It was determined that process control of the printer is extremely important since the dominate factor is the adhesion of the trace to the LCP, and not the joint strength between the ink layer and the ink trace. Also, 6 layers appear to be favourable for increasing the joint shear strength, with or without ENIG finish on the substrate. Also, there appears to be a different evolution of the trace and the joint ink, due to the trace undergoing the 200 °C in an oven twice and the joint ink only once. This does not bode well for long term thermal exposure. Overall, careful process control, layer count, and placement force seem to affect the overall joint shear strength. The developed process

is not only helpful for a two-interconnect assembly but can be extended to multi-interconnect assembly like area-array configurations.

RESEARCH CONTRIBUTIONS, CONCLUSIONS, AND FUTURE WORK

1.26 Research Contributions

This work has made important contributions to the field of flexible electronics with a particular focus on the adhesive strength of printed ink as well as the assembly process and interfacial shear strength of surface mount devices on flexible substrates. Specifically,

- Two different modified peel test methods have been developed for printed ink. The developed methods have been demonstrated on two material systems. Thus, these methods are generic and can be applied to a wide range of material systems.
- A comprehensive fully-additive process has been developed for assembling surface mount components on flexible substrates. By focusing on the number of layers printed, the placement force, and the type of fixturing, this work has contributed to understanding various parameters that influence the successful assembly of devices on flexible substrates.
    - By performing a combination of electrical test, die shear test, and failure analysis, this work has provided important insight into the failure mechanisms of device-to-substrate interconnects under shear loading.
    - By creating an ENIG platform with printed layers, this work has isolated the sintered ink interconnect and has provided insight into the failures of the sintered ink interconnect.

- Through numerical modeling and material characterization, this work has provided quantitative assessment of interfacial fracture energy for printed inks.

1.27 Conclusions

Based on this work, the following conclusions can be drawn:

- Peel Test Method 1 which uses the host flexible substrate to peel the flexible substrate from the printed ink can be successfully employed to determine the printed ink adhesion strength. The measured adhesion strength for Suntronic™ EMD 5730 and Rogers Corporation ULTRALAM® 3850HT substrate material system for the different prints ranged from 100-200 N/m and for NovaCentrix® Metalon ® JS-B25P Ag ink and Novele ™ IJ-220 PET substrate material system is 100 N/m.
- Peel Test Method 2 which uses a substitute material for peeling the printed ink from the flexible substrate is demonstrated to determine the printed ink adhesion strength. For one set, the measured adhesion strength with flexible FR4 substrate substitution layer for Suntronic™ EMD 5730 and Rogers Corporation ULTRALAM® 3850HT material system is 150 N/m.
- Numerical analysis of peel test method reveals that the interfacial fracture energy 100 J/m2 through sequential crack extension technique and J-imtegral.
- In a fully-additive assembly process, the number of layers on substrate pad and the placement force play an important role in the assembly. The process control of inkjet printing process has a more dominant role in the quality of the assembly.

- Through careful selection of assembly process parameters, a die shear strength of about 4 N can be achieved, and this roughly corresponds to about 6.5 MPa shear strength for the interconnects.

1.28 Future Work

There are several topics that can be pursued or extended beyond what has been studied in this work. These include:

- Most of the peel tests conducted in this work have 90° peel angles. In other words, the peel arm remains perpendicular to flexible substrate. This test can be modified to include other peel angles so that the interfacial fracture energy can be determined as a function of peel angle, and thus, the mode-mixity of the interface.
- The data extraction in the models has used linear-elastic-plastic behavior. Future models need to include viscoelastic or hyperelastic behavior for the flexible substrate.
- Most of the tests in this work have been done using inkjet-printed conductors. The developed tests can be applied to screen-printed inks, aerosol-printed, and other printed inks as well. In all of those situations, the failure modes will be different. For example, screen-printed ink is a composite of polymer matrix with silver flakes or particles.
- The fully additive assembly process has been demonstrated for a two-pad device. It can be extended to other devices that have peripheral-row or area-array pads such as quad-flat pack or flip-chip assemblies.

- The integrity of the interconnects has been evaluated through electrical test and die shear test in this work. However, in practical applications, the assembly goes through fatigue and other thermal and humidity excursions. Also, the flexible assemblies undergo stretching, bending, twisting, and other mechanical loads. The assembled components should be evaluated under such fatigue, thermal/humidity, and mechanical loading condition.

APPENDIX A. PROCEDURES FOR SAMPLE IMAGING INPARTICULAR SCANNING ELECTRON MICROSCOPE

Scanning electron microscopes (SEMs) help with characterization of films: grain size, texture, element identification (coupled with EDS), and much more. Not only knowing what type of detector is available, but knowledge of the layout of the SEM's detectors is needed to correctly analyze the images as well as make achieving the image faster. A deeper understanding can also help with troubleshoot for a better image. In general there are two main types of sample configurations discussed in the following work: as-is samples which lie flat on an SEM sample stage or a cross-section which is a sample grounded down to a point of interest.

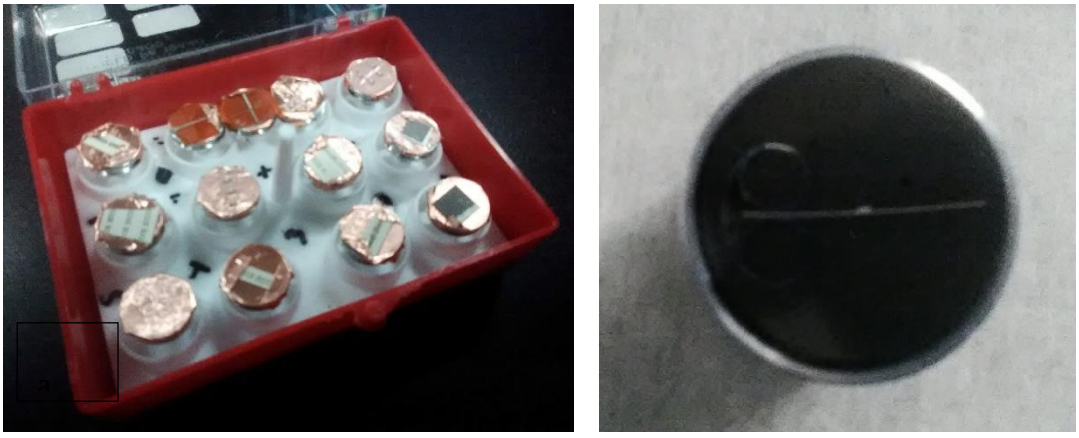

Figure 124: (a) Flat Samples vs (b) cross-section

A.1 Flat Samples Preparation

For flat samples it is important to have a way to identify a specific area on the sample if trying to compare the same location in multiple stages of the experiment that has

steps conducted outside the SEM. If features on the sample are not distinct enough, markers can be created on the sample either with SEM specific marker which typical have a carbon ink or purposely damaging the surface using a tool like a scribe or nano-indentor. By having a visible marker, it allows for the better alignment of the pictures for further image processing techniques like digital image correlation (DIC). There may also be markers on the holder itself to help the user orient themselves while trying to position the sample in the chamber. For quicker placement, it is often good to take an image with camera phone of the stage holder to have an idea of how the samples are oriented with respect to the markers.

Figure 125: Distinct features, marker scratched in (red circle to point out), and marker on the carousal sem holder

Cleaning the surface is also important; however, care must be taken depending on the intension of the SEM. Ultraviolet light ozone cleaners are very good for cleaning surface; however, they may remove the intended carbon surface. This same cleaner could potentially be used before fabrication to help with adhesion of the film/ink due to changing the surface energy as well as exposing the true surface of the substrate. The energy of the SEM beam may also be high enough to also change the surface of the structure which is what happened during imaging of the far right image of Figure 125. Also note, if the sample is non-conductive, there must be measures taken so that the electrons hitting the surface

have a way to ground like by a sputtered thin conductive coating. If not considered, super charging can occur, and it is noticeable due to the charged surface creating a mirror surface and the image reflects the chamber as shown in Figure 126.

. 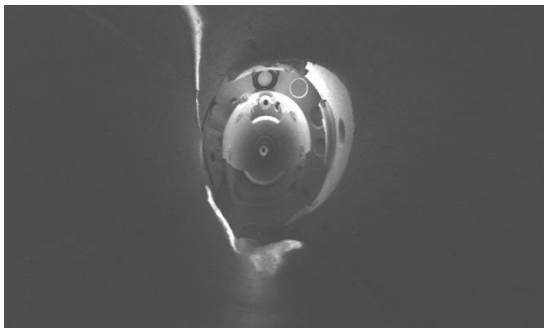

Figure 126: Super charging mirror surface

A. 2 Cross-section Sample Preparation

To examine the joint as well as adhesive thickness in scanning electron microscope (SEM), cross-sectioning was done. First the sample was underfilled and placed on a hotplate. The underfill was stiff enough to protect the joint during sample handling and cross-sectioning. Next, sample was trimmed to be able to fit in the 1.25 inch EPDM Round mounting cup. With the EPDM material for the cup, a release layer material is not needed. Other options include use of a release layer sprayed/coated the inside of the rigid plastic cups or use of a single use disposable cup. Oriented with the intended cross-section plane laying on the cup's bottom surface, the sample is held upright and in place with stainless steel SamplKlip clip at the bottom of the mounting cup. The reusable flexible rubber mounting cup allowed for easier extraction from the cup after an hour room temperature cure. Labeling of the sample was associated with the mounting cup label to ensure no confusion with multiple samples being prepped at the same time. Due to issues with

charging while imaging, a Buehler conductive filler, nickel-base, is added to the Samplkwick powder (1:1 weight ratio) before addition of the Samplkwick liquid (2:1 volume). For this analysis the additional nickel based particles would not interfere with the study, since the goal of the assembly cross-section is to look at the silver ink's interaction with the pre-sintered traces and the ENIG electrodes on the resistor/QFN or the gold bumps on the flipchip. Please note that if a filler is not used, often an additional layer of conductive material, e.g. gold or carbon, will need to be sputtered on top to help with imaging. After mixing the ingredients together, the mixture is poured into the mounting cup, completely covering the sample and high enough to account for shrinkage of the acrylic while curing. After room temperature cure and removal of the mold from the cup, the label is scratched into the mold on side.

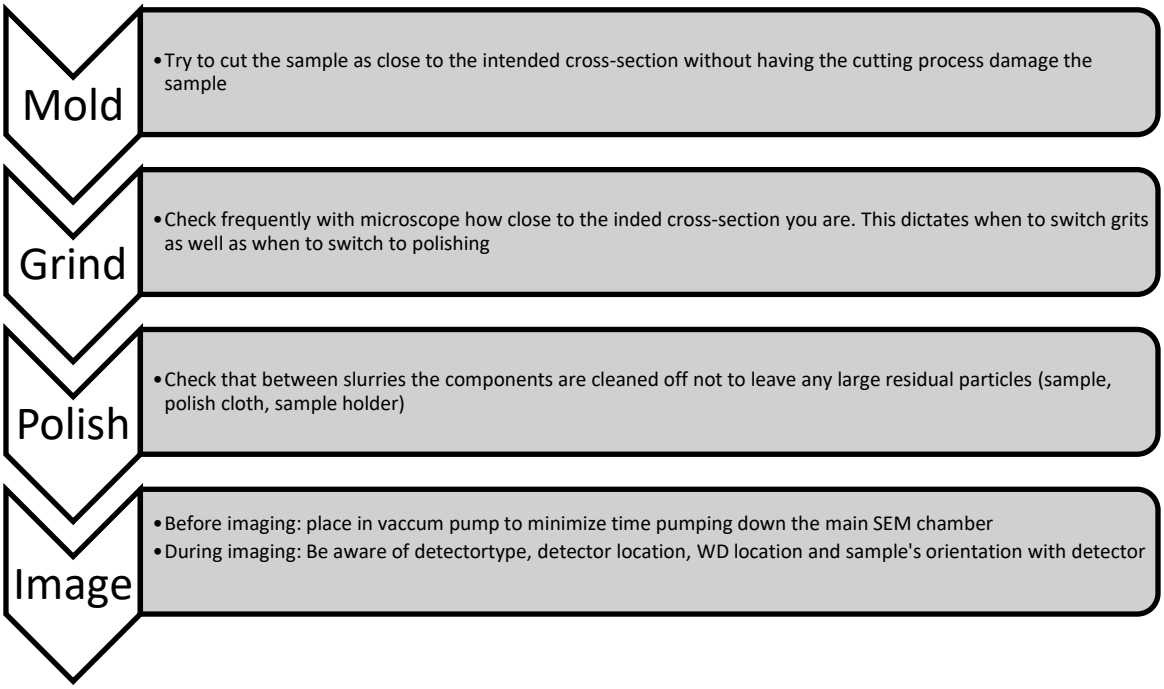

Figure 127: Recap of Grinding and polishing process flow

An Allied MetPrep 3TM Grinder/Polisher with Power head was used to grind down the cross-section. At intervals of 3 minutes, the grinder placed a force of 3N, at a rotation rate of 150 rpm with constant water flow. A microscope was used to examine the cross-section to determine if the intended interface was reached. For mechanical grinding, the grit size was stepped up from 120, 200, 400, 600, 800 and 1200. After grinding, the tool is cleaned before polishing and adding the magnetic polishing cloth. Polishing was done with alumina particle and a DI water slurry. For polishing settings, a 1 N force was used with no water running so as not to wash away the slurry with the intended particles. With each transition to smaller particles (5 micron to 1 micron), the tool and sample is cleaned with water, so that the larger particles do not scratch the surface.

After grinding and polishing, the samples were cleaned off with water and then placed in a vacuum chamber to degas. The acrylic does not keep out the water and has air pockets unlike epoxy type mold. If the pre-degassing is not done, then it will take longer for the SEM chamber to pump down to a working pressure. A recap of the steps is shown in Figure 127.

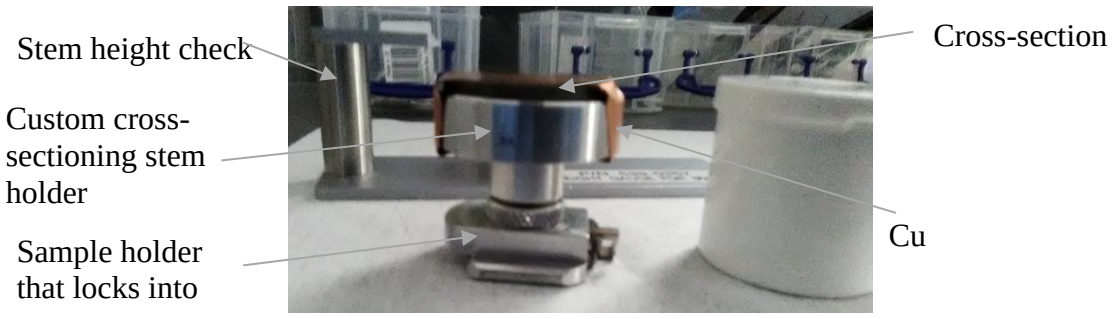

Figure 128: STEM holder

Afterwards the cross-section was placed in a custom STEM holder that fit the cross-section mold as shown in Figure 128. The piece could be held in place with either carbon tape or with Cu tape. The carbon tape or Cu can lay inside the cup of the STEM holder or running across the top. If on the top, copper tape can be scratched with an easily identifiable marker to indicate the sample as well as the intended location region for imaging. By having the tape across the sample, it made for easier rotation orientation of the sample after loading the sample into SEM as well as the larger markers to determine a good focus point. However, some charging may occur or bad tape placement may cause difficulties with the imaging. With the sample preparation, less time is taken to find the sample.

A.3 SEM Choices- What's in the source/detector?

Depending on the experiment running, the SEM can make a difference in the sample preparation as well as determining if it is possible to examine. Factors which impact the image from the material prep side include material examining, what is the sample's arrangement with other materials, and intention of the picture (angle, cross-section, crystallography data, element identification and etc.) On the tool side, images depend on the detector, focal length (WD), source, current and voltage setting as well as the alignment of the beam. In terms of source, often cold-field emission and schottlky have smaller probe diameters (finer resolution) at lower currents compared to Tungsten Thermionic [54].

For imaging, the Hitachi 8230 and 8210 are utilized in this work due to their easily comparable images for system similarity as show in Table 16. Also, the holder was conveniently about the same standard loading height for the Hitachi, which lets the full

WD range be in play. Since the Hitachi 8230 is a cold-field emission type SEM, it allows for a much lower detection range and in turn does not require the sample to have a separate conductive coating to be applied on top of the of the sample.

Table 16: SEM comparison chart

	Hitachi SU8230	Hitachi SU8210	Zeiss Ultra
Load Lock	Y	Y	Y
Source Type	Cold field emission	Field Emission Gun	Schottky Field Emission Gun
Detectors	SE (L), SE (U), LA-BSE, HA-BSE, EDS	SE (L), SE (U), LA-BSE, HA-BSE	InLENS, SE (L)

In the Hitachi system there are two types of detectors at both a higher angle as well as a low angle. Figure 129 shows the importance of detector placement when comparing positions *a* and *b*, as well as the importance of understanding how the sample is oriented with respect to the detector, especially the lower detectors (position a and c). For the lower detectors, it is better for a larger working distance (8-15 mm) range, and the images typically seem to have more depth. While the top detectors are better with a shorter working distance and top down view. In addition the detector types are secondary electron detectors (SE) and back-scatter electrons (BSE). Typically the former is used for imaging purposes while the latter is used to obtain more information about confirming the crystallography and confirming different elements by their brightness “Z”. For element identification, energy dispersive x-ray spectroscopy (EDS) detector is needed. Additional images can be created by mixing the signal between two of the detectors.

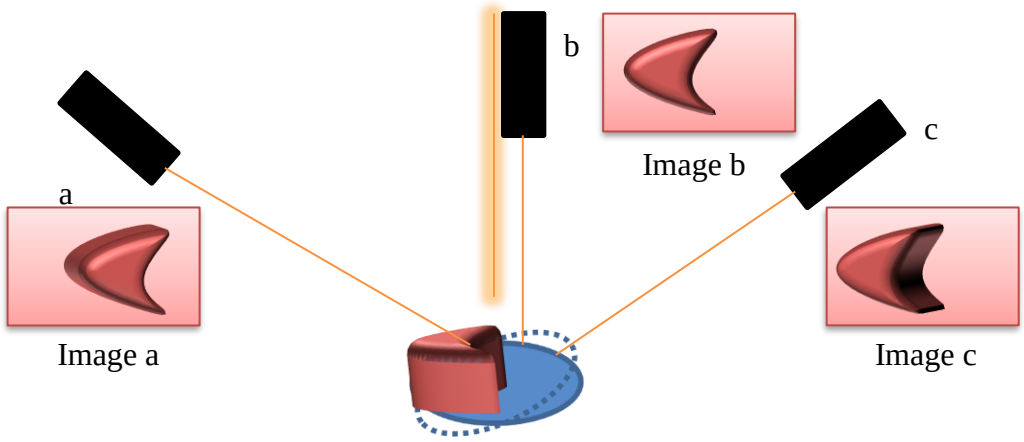

Figure 129: Simplified Schematic to demonstrate importance of detector placement

In the Hitachi 8230, it has a mode to take multiple images from different detectors at the same time as shown in Figure 131: SE (U), Figure 132: SE (L), and Figure 133:HA-BSE. The images are of a cross-sectioned silver ink assembly of alumina resistor with (ENIG) finish on the electrodes as shown in Figure 130.

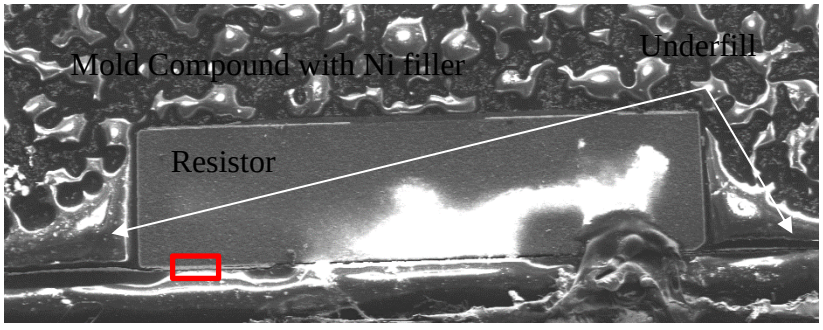

Figure 130: Assembly Cross-section

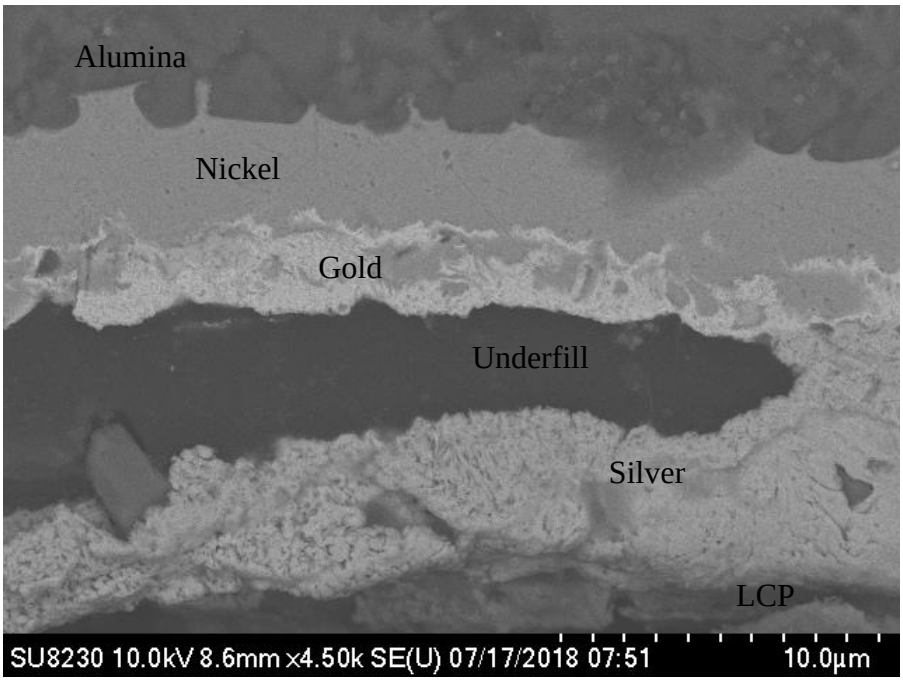

Figure 131: Secondary electron detector in the upper location

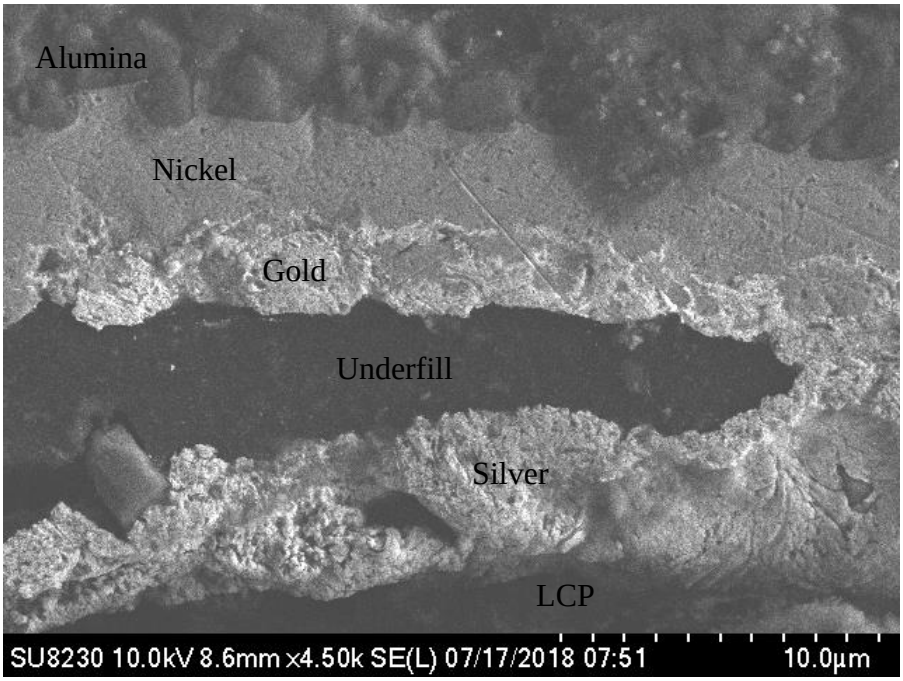

Figure 132: Secondary electron image in the lower position

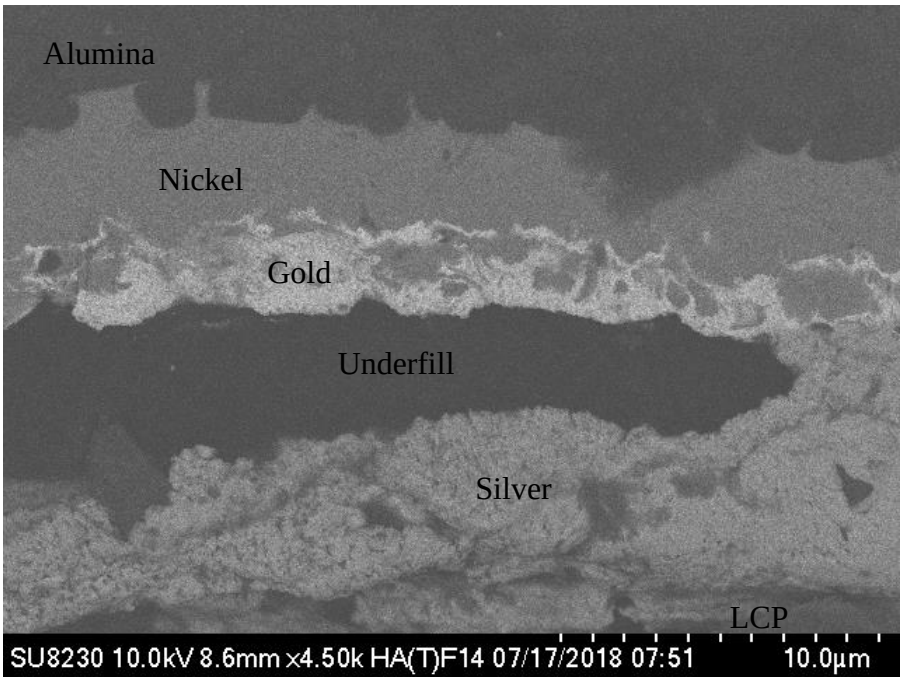

Figure 133: High angle back-scatter electron detector

As another point of reference about image discussion, a fracture surface of an epoxy mold compound and copper lead frame double cantilever beam test sample is shown in Figure 134. Since the purpose of this examination was to identify how the EMC fractured off the Cu lead frame, the voltage was purposely set much lower as well as intentionally using a cold-field emission tip SEM it can often be used even at voltages below 1 kV. The Figure 131-Figure 133 with the assembly needed to have a high voltage input due to the need to distinguish between the different metals. Also to get more detail of the textured surface, a mixed signal of the upper and lower SE detectors was utilized. Due to this higher voltage input, the imaging had more distortion in some areas due to a high degree of charging on the sample since a high fraction of the sample was a form of polymer.

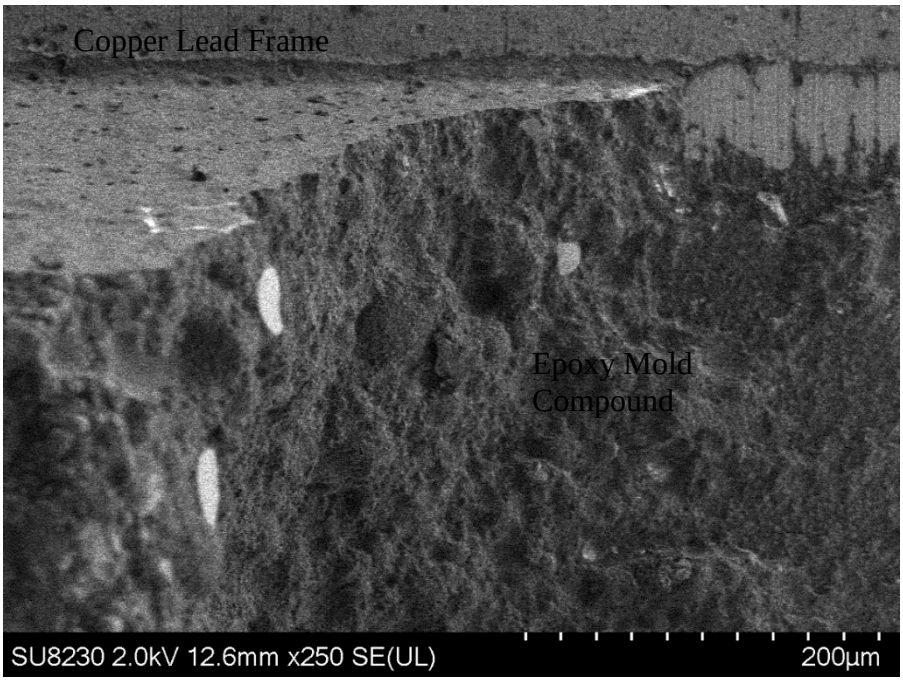

Figure 134: Mixed Signal

A. 4 Surface Analysis Basics and Impact on Image/EDS

For the EDS detector, typically a WD of 15+- 2 mm is optimal for the Hitachi 8230 tool. It is also important to ensure the detector is only receiving the signals from the sample, and so the chamber camera's light needs to be turned off to ensure a deadtime of around 10-30%. Please note that the 10% is on the lower side for deadtime, and that a high deadtime like 50% may result in artifact sum peaks [54]. The amount of energy available will limit what elements are visible during the test. This energy will also affect how deep into the surface the information comes from and is dependent on the material's structure and basic binding energy. It is suggested to take a surface analysis or read further in depth to have a better understanding about the limits for what the information is capturing; however, the programs associated with the EDS detector are good at identifying potential elements with the association of what is anticipated in the sample. In general, it is suggested

for nearer to the surface and lighter elements to use beam energy of 5-10 keV and to use beam energy above 15 keV for heavier elements or more distinction. [54] For samples which need higher percentage accuracy, it is suggested to look at (XPS).

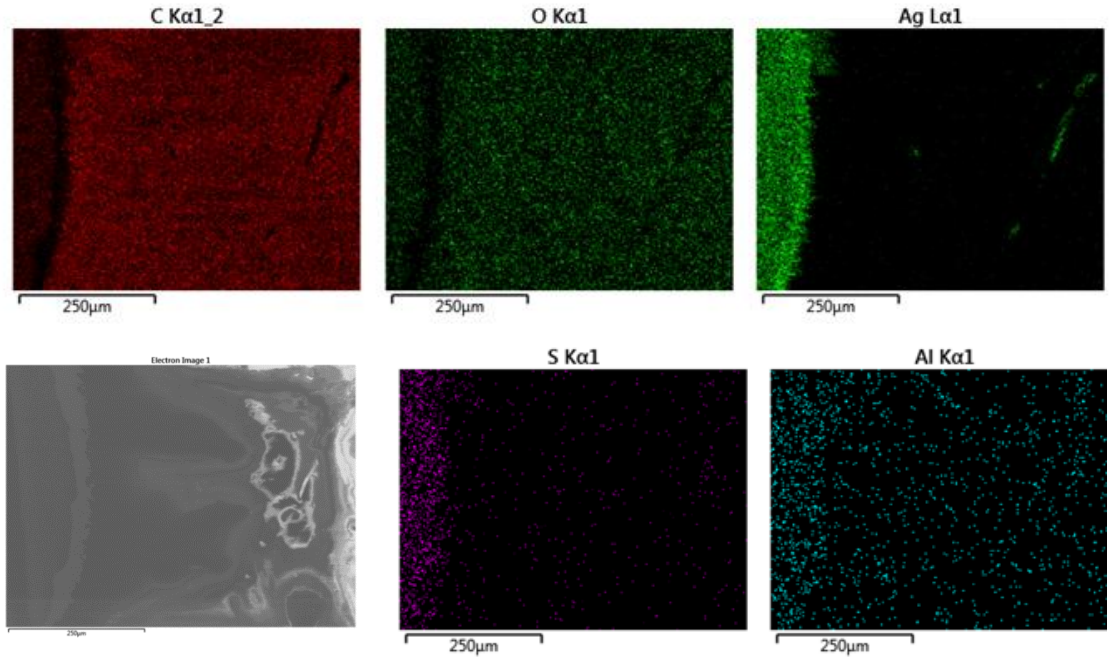

Figure 135: EDS on the LCP substrate with Ag mostly removed during peel test

Depending on the sample in the SEM, a conductive layer may need to be sputtered on top so as not to let the high energy from the beam damage the substrate. As mentioned before, it is important to know what the intention of the EDS is. If it is to examine a Au joint, it would be better to use a carbon coating so that the sputtered Au does not affect the conclusions drawn. In general some of the features may be hidden as well by the film visually in the SEM, as shown with the resist with Au sputtered coating in Figure 136.

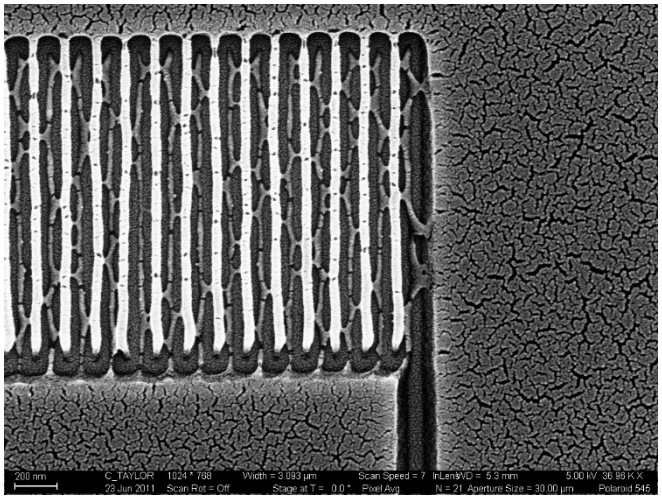

Figure 136: Image to show resist which had Au sputtered on top. This was part of a test to help determine the dosage for e-beam lithography

APPENDIX B: ENIG Processing

For the ENIG processing, a small-scale configuration is used with various beakers filled with chemicals produced by Atotech in a fume hood like the one in Figure 137. The sample is immursed into the various beakers in the fumehood as shown in the layout of Figure 138 and in the order outlined in Table 17. A few of the beakers are heated to activate the desired reaction. The hoteplates, which are used to activate the electroless Ni plating and the immersion Au plating, have a countius temperature feedback to ensure the solutions are at the desired temperatures. For the electroless plating, chemical reactions are used to add an additional material with out use of an external power and a source material, like in the more common electroplating. In the immersion process, the metal surface has metal ions which are displaced by the desired metal coating.

Figure 137: Beaker in fumehood

For flexible substrates, a Cu-less FR-4 back plate is needed. It is important to note that the bare FR-4 board is used so that the solution is not depleted with unnecessary plating of the Ni carrier during the electoless plating as well as the follow up of the immersion Au plating. To attach the flexible substrate to the board, a chemical resistant tape is utilized so that the adhesion of the tape can withstand the acids used in the elecroless plating process. A clip and crossbar system is used to hold the board while in the beaker solutions for the various required time. A check of how the carrier is held in the clips with being in the solution is needed to ensure that the magnetic spinners do not knock the sample off the clips during the processing. Also a check is needed to ensure that the solution heights are high enough as well as at the desired pH level: Aurotech Cnn a pH of 4.8.

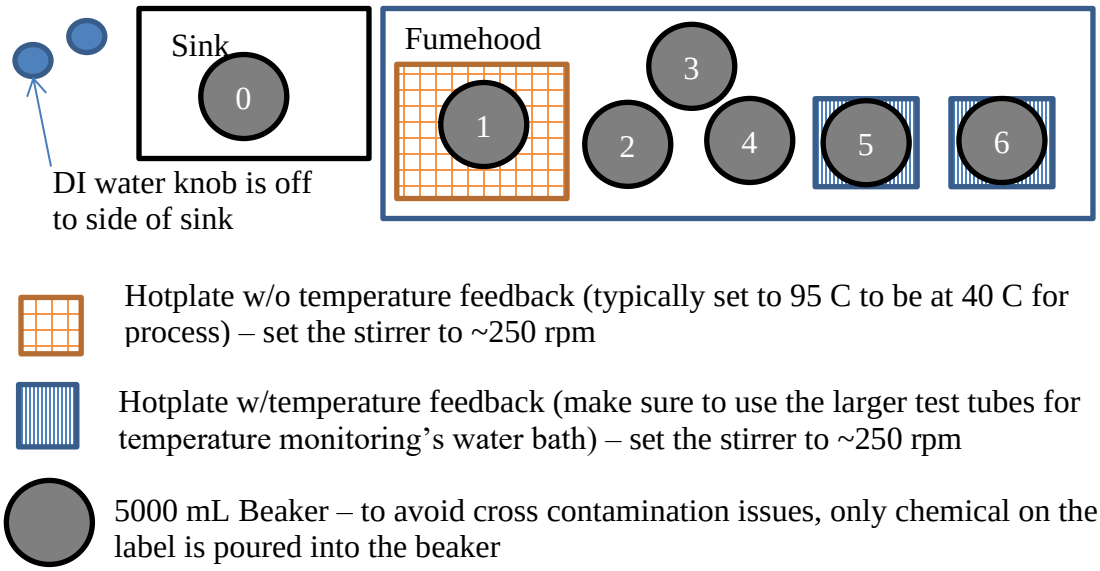

Figure 138: Layout of the beakers in the fumehood

Table 17: Steps for the ENIG Processing

Step	Beaker #	Process	Temperature (°C)	Time	
				(s)	(min)
1	1	Pro Select SF	40	300	5
2	0	DI Water Rinse	-	120	2
3	2	Microetch SF	R.T.	120*	2*
4	0	DI Water Rinse	-	120	2
5	3	Aurotech Predip	R.T.	180	3
6	4	Aurotech Activator	R.T.	180	3
7	0	DI Water Rinse	-	120	2
8	5	Aurotech CNN (Ni)	85	TBD	22*
9	0	DI Water Rinse	-	120	2
10	6	Aurotech SF plus	85	TBD	12
11	0	DI Water Rinse	-	120	2
12	-	Dry (can use air gun)	-	-	-

For the processing, there are steps included to help activate the surface for the ENIG finish as shown in Table 17. Initially the sample is immersed in Atotech's Pro select surface finisher, which is an acidic solution that helps prepare the cu board. It is followed by a DI water rinse. Next an acidic solution, microetch surface finish, etches to clean the Cu surface. This step is also followed with a DI water rinse. Subsequently, the sample is dipped into an Aurotech Pre-dip, which is used in coordination with the Aurotech activator that is specifically meant to prep the sample for the electroless nickel platting. The sample is then dipped into DI water rinse. Aurotech CNN solution is used to deposit the Ni layer. It deposition rate is approximately 165 nm/min and so for a 5-8 mins dip the deposited thickens is about for 1 micro. This step is also followed by a DI water rinse before the Au immersion plating. Aurotech SF plus solution is estimated to have about a 10 nm/min deposition rate, and so the desired 100 nm should be at least 10 min immersion. Afterwards, a final DI water rinse is pursued.

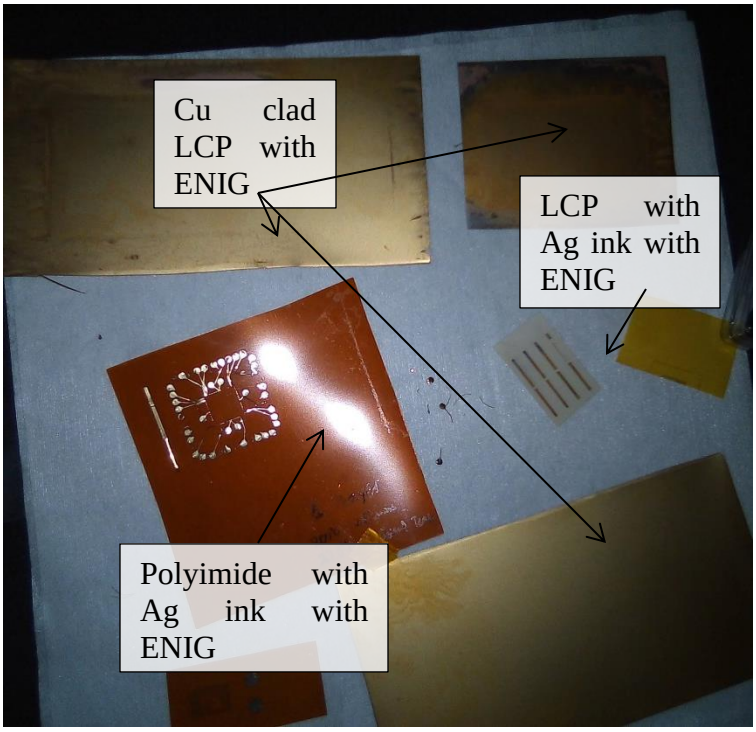

Figure 139: Samples after ENIG processing

It is important to note that this process does not require the under lying substrate to be Cu. Cu-clad LCP is chosen due to its commercial availability. This same ENIG process is used to see how well the printed ink surfaces handle the process. As Figure 139 demonstrates, the Suntronic™ EMD 5730 ink pairing with polyimide is not recommended since delamination occurred due to the plating stresses. Since the LCP sample pairings did not delaminate, there is potential for future soldering demonstrations onto Ag ink ENIG coated samples.

APPENDIX C: Stress and strain detection tools

Different types of levels of measuring stress are available and the choice of technique to use is based on the intended application. The types of measurements include active measurement with sensors (commercially available strain gages or fabrication of sensors), and non-contact techniques which either use measurements based on surface analysis/structure or monitoring displacement.

For commercial strain gages, the footprint is on the mm scale and need to be attached to a smooth surface at a specific orientation. In terms of product, the area of interest may need to be destroyed to provide the smooth surface. In optimizing packaging design, approaches based on quantitative knowledge as well as qualitative pass/fail tests are used. These approaches rely heavily on past knowledge and experimentation in the lab with the pre made sensors.

The test dummy chips often utilize serpentine pattern gages and are found in pairs such that there are two distinct gage factors to separate out the mechanical strains and thermal strains which may occur [55-62]. Typically any electrical signal sensor will also be sensitive to heat due to the physics which couple the two together. As mentioned earlier in the sensor fabrication comparison of cleanroom processing and direct write, gage factor is used to distinguish sensitivity. The sensors with the best factors are doped sensors; however, the doping process is costly as well as possibly damaging to the surrounding surface [57, 59, 63-65]. There are other teams developing sensors with other novel

materials like graphene and CNT [62, 66, 67]. The main concerns for sensors include 1) drift of the sensors, 2) cross-talk with sensors/any additional metallization, 3) stresses induced within the additional metallization/processing and 4) correct signal processing of the sensors based on the sensitivity. Interestingly, transistor current drift is another way in which to back calculate the stress build up.

Compared to sensors, the other main area of stress/strain measurements are non-contact methods. These can be separated into concepts based on either surface analysis/structure or monitoring displacement. Both are often utilized with FEA techniques to predict the localized stresses since the measurements given typically are a general average.

Surface methods depends on if the detection type is available. Often comparing the signal of an ideal "unstressed" crystal/polycrystalline structure to the stressed signal to infer the stress; limited in that many of the surface techniques have limited depth (*e.g*. chips located in a fully assembled package are often not possible for measurements). Each of the techniques also have limitations based on the spot size, shift resolution is large enough, as well as the before mentioned depth of penetration. From photons in Raman Spectroscopy to x-rays in x-ray diffraction (XRD) to wide range of x-ray sources (μ- xrd) and even light (photoelasticity) there are a wide range of options which tool limitations will dictate what assumptions can be made from the measurements as well as the applicability of the material.

In x-ray diffraction, how the x-ray's reflect/refract off the surface follow's Bragg's law. The thin film technique is based on the same concept of powder diffraction, and so for the limited source the film has a polycrystalline structure. To determine the thin film

orientation, a sweep changing the incoming x-rays and monitoring how the intensity of that directed spot. The final comparison of intensities with the angle sweep are compared with known index cards to determine the dominate orientations. To do a stress measurement with a single source XRD, the same type sweeps are made multiple times, but with the sample's orientation changed by rotation. The smallest spot size tends to be on the 1x1 cm so the stress measurement is an average of the area. In micro-XRD, often the source is a synchrotron tool that gives a wider range of energies to act as a source as well as a smaller spot size (*e.g.* 5x5 microns), but with this higher energy range the penetration depth of the beam is deeper. This is why this technique is coupled with FEM to back out the local strains from the 2D stress map that was the average of stresses through the depth. [68-70]. This allows a wider range of materials to be utilized; however, one must have to have access to a tool which is hard to guarantee, since the tools are costly or with limited availability. At national labs, researchers can submit proposals for 1-2 day access.

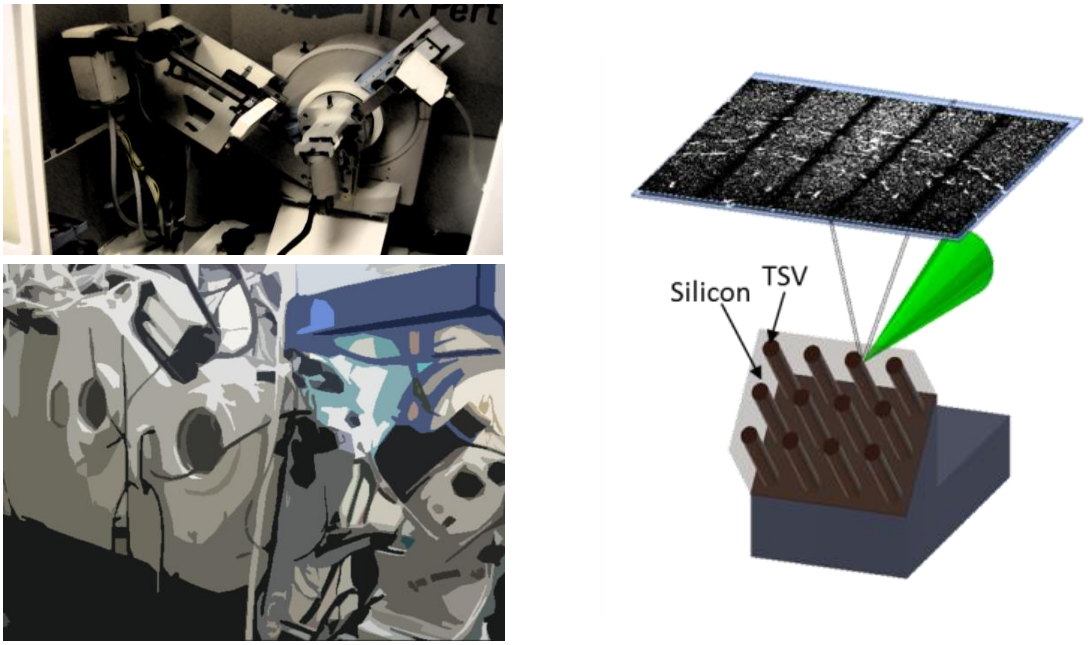

Figure 140: TSV and synchrotron set-up to determine local strains

For integrated circuit applications, ramen spectroscopy examines the stresses in the Si as well as thin films which have monitor-able photons. Similar to XRD, there is a laser source to excite the photons, and the detectors determine the intensity amounts of the "scattered" light as shown in Figure 141. In literature, many demonstrate TSV stresses through Ramen spectroscopy by examining how much of a shift in the peak is from the unstressed area [71-77]. Often these configurations have additional polarizers and wave plates in the path of the laser source, so that stresses can be backed out by changing the angle of how the laser hits the surface with knowledge of the material structure. One such configuration is in Figure 141.

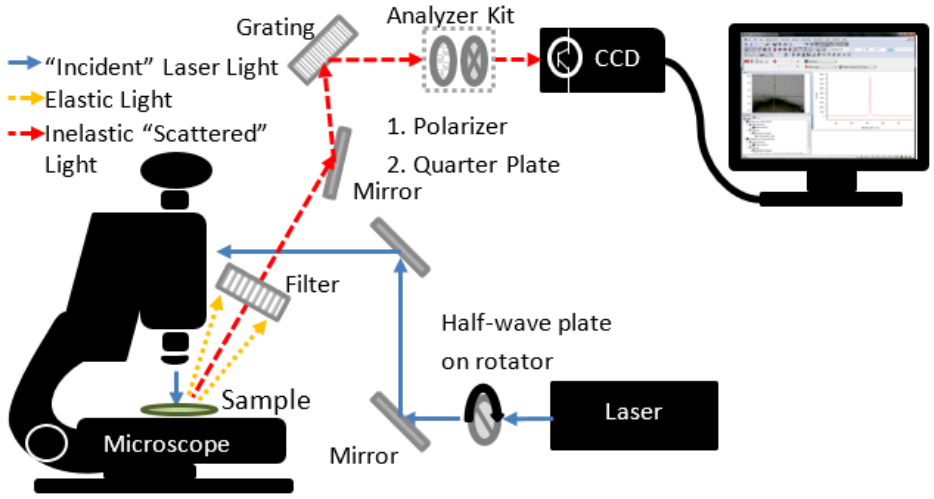

Figure 141: Raman Spectroscopy schematic for examining the stresses in Si

Digital photoelasticity is mentioned as a promising area for measurement of residual stresses for flexible technology [4]. Digital photoelastity utilizes digital algorithms to determine the principal stress difference and directions of planer stress. Initial photoelasticty concepts were used on pure crystalline materials, because they have inherently two different light reflections. Often IR is used as the light source for Si, due to silicon being transparent to IR waves. For semi-crystalline materials, like polymers polyimide, liquid crystalline polymers (LPC) and polyethylene terephthalate (PET), when light passes through a stressed sample then a bi-fringance is created. The paths correspond to the primary and secondary in plane stress. Through automatized phase-shifting, photoelastic measurements are accurate and simplified to obtain the principal information while still having the advantage of being non-contact, whole field, low cost measurements

[78].

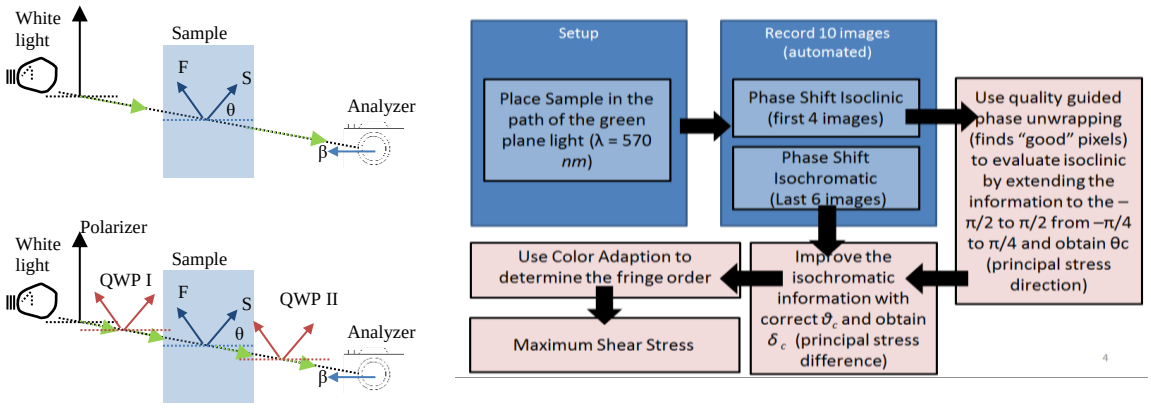

Figure 142: Polarization set up (1) Plane polariscope set up to initially determine the isocline fringe information (2) Circular polarization

A phase-shifting technique, which was developed by Raman, Ramji and Prasath, uses a 10-step imaging process to determine the stress direction by using four isoclinic images from crossed polarized light and principal stress difference by using 6 isochormatic images from circular polarizer set-up [78]. For the isoclinic images, the white light travels through a polarizer, sample with the analyzer near the camera. An algorithm is run after the image is taken to determine the good pixels and unwraps the principal stress direction from the information. Unwrapping refers to the mathematical changing of the phase range from [–π/4, π/4] to [-π/2, π/2], which occurs due to the inverse tangent in the formula $\theta_c = \frac{1}{4}\tan^{-1}\left(\frac{I_4-I_2}{I_3-I_1}\right)$[79]. This information is used to improve the isochromatic information. For the isochromatic images, the white light travels though polarizer, QWP, sample, another QWP and then the analyzer near the camera. The isochromatic information is used to obtain the principal stress difference, and then the maximum shear stress can be determined with

color adaption theory to determine the fringe order [80]. In Figure 143 an example of a digital photo elasticity system is set up around a universal test system which could apply a tensile loading to take the measurement with a white light source. The filters for the analyzers and the quarter wave plates are tuned for the green wavelength. This is one of the more visible wavelengths across all the different polarizations, and means the outside ambient light will not affect the measurements. With the digital photoelasticy set-up, the program finds the stress using the phase-shifting algorithm, quality pixel detection and the tri-color adaptive theory to determine the principal stress difference and directions.

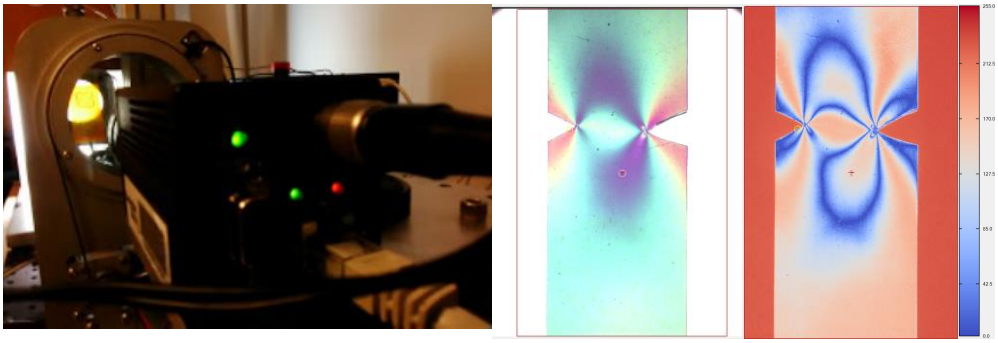

Figure 143: (a) Camera viewthrough anaylzer and QWPII, (b) Camea Image PET with notches placed on the side (c) associated fringe picture

Lastly, displacement tracking methods are used to determine strains and then the stresses on the sample with either stack-up of additional material or with an external loading that typically is mechanical or thermal in nature. For manufacturing in the cleanroom, the first reference is the Stoney's equation which relates how each stack-up layer's radius of curvature changes to the stress induced with the new deposited layer. Often a profilometer is used to measure the profile in-between each step. There are other techniques which require additional materials to be added on the intended surface typically in either a grid pattern or a random speckle pattern. Laser Moire use the interferometer

techniques to see how the grid pattern changes with respect to applied loading and a photograph of a tool is shown in Figure 144. In digital image correlation (DIC), the speckle pattern points or grid pattern points are monitored with the applied loading in subsequent images. By knowing the relative camera position with respect to the sample by calibration with an image grid, the distances between can be determined with respect to the pixel distance.

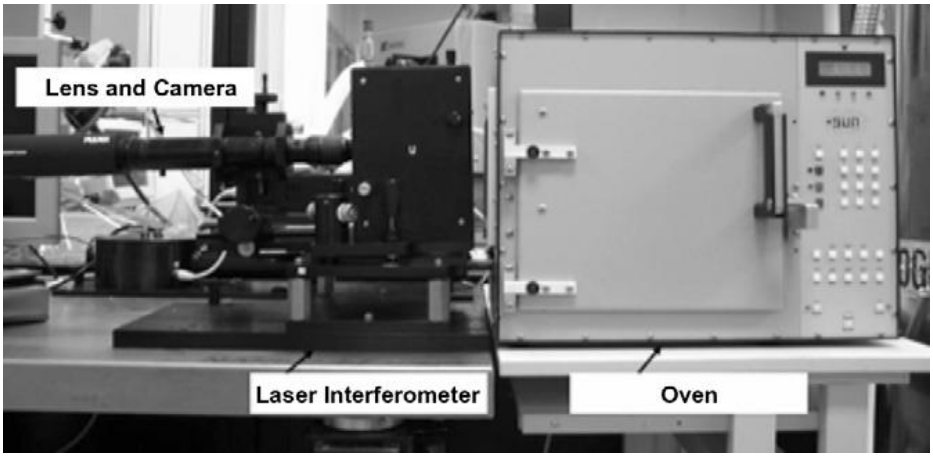

Tunga, K. and Sitaraman, S. K., "Laser Moire Interferometry for Fatigue Life Prediction of Lead-free Solders," Microelectronics Reliability, Vol. 50, No. 12, pp 2026-2036, Dec. 2010

Figure 144: Laser Moire

REFERENCES

[1] D. Strumpf. (2018). *Smartphone Makers Seek Foldable Phones With Flex Appeal*.

[2] M. Sawh. (2018). *The best smart clothing: From biometric shirts to contactless payment jackets (April 16,2018 ed.)*. Available: https://www.wareable.com/smart-clothing/best-smart-clothing

[3] (2016, 11/7/2019). *Flexible Hybrid Electronics*. Available: http://www.designhmi.com/2016/07/26/flexible-hybrid-electronics/

[4] M. Gunda, P. Kumar, and M. Katiyar, "Review of Mechanical Characterization Techniques for Thin Films Used in Flexible Electronics," *Critical Reviews in Solid State and Materials Sciences,* vol. 42, no. 2, pp. 129-152, 2017/03/04 2017.

[5] G. T. Ostrowicki, "Magnetically Acutated Peel Test for Thin Film Interfacial Fracture and Fatigue Characterization," George W. Woodruff School of Mechanical Engineering, Georgia Institute of Technology, 2012.

[6] M. B. Modi and S. K. Sitaraman, "Single-sample decohesion test: mechanics and implementation," *International Journal of Fracture,* vol. 129, no. 1, pp. 1-20, 2004/09/01 2004.

[7] R. Lacombe, *Adhesion measurement methods theory and practice*. Boca Raton, FL: Boca Raton, FL : CRC/Taylor & Francis, 2006.

[8] P. Janghoon, L. Jongsu, S. Ki-Hak, S. Kee-Hyun, and K. Hyunkyoo, "Quantitative analysis of peel-off degree for printed electronics," *Japanese Journal of Applied Physics,* vol. 57, no. 2, p. 020304, 2018.

[9] M. Zhou *et al.*, "The Extended Peel Zone Model: Effect of Peeling Velocity," *The Journal of Adhesion,* vol. 87, no. 11, pp. 1045-1058, 2011/11/01 2011.

[10] S. C. Joo and D. F. Baldwin, "Analysis of Adhesion and Fracture Energy of Nano-Particle Silver in Electronics Packaging Applications," *IEEE Transactions on Advanced Packaging,* vol. 33, no. 1, pp. 48-57, 2010.

[11] E. Halonen, T. Viiru, K. Ostman, A. L. Cabezas, and M. Mantysalo, "Oven Sintering Process Optimization for Inkjet-Printed Ag Nanoparticle Ink," *IEEE Transactions on Components, Packaging and Manufacturing Technology,* vol. 3, no. 2, pp. 350-6, 02/ 2013.

[12] H. C. Jung, S.-H. Cho, J. W. Joung, and Y.-S. Oh, "Studies on Inkjet-Printed Conducting Lines for Electronic Devices," *Journal of Electronic Materials,* vol. 36, no. 9, pp. 1211-1218, 2007/09/01 2007.

[13] K. Inyoung, L. Taik-Min, and K. Jongryoul, "A study on the electrical and mechanical properties of printed Ag thin films for flexible device application," *Journal of Alloys and Compounds,* vol. 596, pp. 158-63, 05/25 2014.

[14] H. Felix, H. L. Hauke, and L. Rolf, "On the identification of cohesive parameters for printed metal-polymer interfaces," *Smart Materials and Structures,* vol. 26, no. 5, p. 055025, 2017.

[15] S. McCann *et al.*, "Determination of Energy Release Rate Through Sequential Crack Extension," *Journal of Electronic Packaging,* vol. 139, no. 4, pp. 041003-041003-9, 2017.

[16] B. N. An, M. Kempf, B. Leyrer, T. Blank, J. Kolb, and M. Weber, "Evaluation of Ag-sinter pastes for the die attachment in power electronic modules using design of experiments," in *2016 18th European Conference on Power Electronics and Applications (EPE'16 ECCE Europe)*, 2016, pp. 1-10.

[17] J. Arrese, G. Vescio, E. Xuriguera, B. Medina-Rodriguez, A. Cornet, and A. Cirera, "Flexible hybrid circuit fully inkjet-printed: Surface mount devices assembled by silver nanoparticles-based inkjet ink," *Journal of Applied Physics,* vol. 121, no. 10, p. 104904, 2017/03/14 2017.

[18] M. J. Yim, Y. Li, K.-s. Moon, K. W. Paik, and C. P. Wong, "Review of Recent Advances in Electrically Conductive Adhesive Materials and Technologies in Electronic Packaging," *Journal of Adhesion Science and Technology,* vol. 22, no. 14, pp. 1593-1630, 2008/01/01 2008.

[19] R. Cauchois *et al.*, "Wire-bonding on inkjet-printed silver pads reinforced by electroless plating for chip on flexible board packages," in *3rd Electronics System Integration Technology Conference ESTC*, 2010, pp. 1-6.

[20] B. K. Tehrani, B. S. Cook, and M. M. Tentzeris, "Inkjet-printed 3D interconnects for millimeter-wave system-on-package solutions," in *2016 IEEE MTT-S International Microwave Symposium (IMS)*, 2016, pp. 1-4.

[21] J. Putaala *et al.*, "Capability Assessment of Inkjet Printing for Reliable RFID Applications," *IEEE Transactions on Device and Materials Reliability,* vol. 17, no. 2, pp. 281-290, 2017.

[22] J. Zürcher *et al.*, "Nanoparticle assembly and sintering towards all-copper flip chip interconnects," in *2015 IEEE 65th Electronic Components and Technology Conference (ECTC)*, 2015, pp. 1115-1121.

[23] Z. Yin, Y. Huang, N. Bu, X. Wang, and Y. Xiong, "Inkjet printing for flexible electronics: Materials, processes and equipments," *Chinese Science Bulletin,* journal article vol. 55, no. 30, pp. 3383-3407, 2010.

[24] K. S. Siow, "Are Sintered Silver Joints Ready for Use as Interconnect Material in Microelectronic Packaging?," *Journal of Electronic Materials*, vol. 43, no. 4, pp. 947-961, 2014/04/01 2014.

[25] K. S. Siow, "Mechanical properties of nano-silver joints as die attach materials," *Journal of Alloys and Compounds*, vol. 514, pp. 6-19, 2/15/ 2012.

[26] J. Kahler, N. Heuck, A. Stranz, A. Waag, and E. Peiner, "Pick-and-Place Silver Sintering Die Attach of Small-Area Chips," *IEEE Transactions on Components, Packaging and Manufacturing Technology*, vol. 2, no. 2, pp. 199-207, 2012.

[27] J. Yan *et al.*, "Pressureless bonding process using Ag nanoparticle paste for flexible electronics packaging," *Scripta Materialia*, vol. 66, no. 8, pp. 582-585, 2012/04/01/ 2012.

[28] K. S. Siow and Y. T. Lin, "Identifying the Development State of Sintered Silver (Ag) as a Bonding Material in the Microelectronic Packaging Via a Patent Landscape Study," *Journal of Electronic Packaging*, vol. 138, no. 2, pp. 020804-020804-13, 2016.

[29] B. E. Kahn, "Patterning Processes for Flexible Electronics," *Proceedings of the IEEE*, vol. 103, no. 4, pp. 497-517, 2015.

[30] D. Numakura, "Advanced Screen Printing "Practical Approaches for Printable & Flexible Electronics"," in *2008 3rd International Microsystems, Packaging, Assembly & Circuits Technology Conference*, 2008, pp. 205-208.

[31] K.-S. Moon *et al.*, "Thermal behavior of silver nanoparticles for low-temperature interconnect applications," *Journal of Electronic Materials*, vol. 34, no. 2, pp. 168-175, 2005/02/01 2005.

[32] Novacentrix. (2011). *Novele IJ-220 Sheet*.

[33] S. Egelkraut, L. Frey, M. Knoerr, and A. Schletz, "Evolution of shear strength and microstructure of die bonding technologies for high temperature applications during thermal aging," in *2010 12th Electronics Packaging Technology Conference*, 2010, pp. 660-667.

[34] J. Y. H. Chia, B. Cotterell, and T. C. Chai, "The mechanics of the solder ball shear test and the effect of shear rate," *Materials Science and Engineering: A*, vol. 417, no. 1, pp. 259-274, 2006/02/15/ 2006.

[35] T. L. Anderson, *Fracture Mechanics Fundamentals and Applications*, 3rd ed. New York: Taylor and Francis, 2005.

[36] L. Banks-Sills, "Fundamentals of Interface Fracture Mechanics," in *Interface Fracture and Delamination in Composite Materials*(SpringerBriefs in Strucutral Mechanics, 2018, pp. 9-17.

[37] J. Auersperg, R. Dudek, and B. Michel, "VCCT and integral concepts of bi-material interface fracture in low-k structures — Going to understand relation," in *2010 12th Electronics Packaging Technology Conference*, 2010, pp. 632-636.

[38] K. B. Narayana, B. Dattaguru, T. S. Ramamurthy, and K. Vijayakumar, "A general procedure for modified crack closure integral in 3D problems with cracks," *Engineering Fracture Mechanics*, vol. 48, no. 2, pp. 167-176, 1994/05/01/ 1994.

[39] L. De Lorenzis and G. Zavarise, "Modeling of mixed-mode debonding in the peel test applied to superficial reinforcements," *International Journal of Solids and Structures*, vol. 45, no. 20, pp. 5419-5436, 2008/10/01/ 2008.

[40] R. Dudek *et al.*, "Determination of interface fracture parameters by shear testing using different theoretical approaches," in *2012 13th International Thermal, Mechanical and Multi-Physics Simulation and Experiments in Microelectronics and Microsystems*, 2012, pp. 1/10-10/10.

[41] L. Durix, M. Dreßler, D. Coutellier, and B. Wunderle, "On the development of a modified button shear specimen to characterize the mixed mode delamination toughness," *Engineering Fracture Mechanics*, vol. 84, pp. 25-40, 2012/04/01/ 2012.

[42] H. Noori, M. Jain, K. Nielsen, and F. Brandys, "Significance of Peel Test Speed on Interface Strength in Cohesive Zone Modeling," *The Journal of Adhesion*, vol. 92, no. 1, pp. 39-51, 2016/01/02 2016.

[43] D. M. Parks, "The virtual crack extension method for nonlinear material behavior," *Computer Methods in Applied Mechanics and Engineering*, vol. 12, no. 3, pp. 353-364, 1977/12/01/ 1977.

[44] C. Arslan. (2018). *Porosity Calculator for SEM Images*.

[45] I. Bower, "Mechanical and Electrical Characterization of Printed Flexible Electronics Deformed Over Complex Surfaces," Masters, Mechanical Engineering, Georgia Institute of Technology, 2018.

[46] P. Rajaguru, H. Lu, and C. Bailey, "Sintered silver finite element modelling and reliability based design optimisation in power electronic module," *Microelectronics Reliability*, vol. 55, no. 6, pp. 919-930, 2015/05/01/ 2015.

[47] "Ultralam 3850HT Liquid Crystalline Polymer Circuit Material Double-Clad Laminates," in *Rogers Corporation*, ed, 2016.

[48] R. Chen, J. Chow, C. Taylor, J. Meth, and S. Sitaraman, "Adaptive Curvature Flexure Test to Assess Flexible Electronic Systems," in *2018 IEEE 68th Electronic Components and Technology Conference (ECTC)*, 2018, pp. 236-242.

[49] N. J. Ginga, "On-Chip Dielectric Cohesive Fracture Characterization and Mitigation Investigaion through Off-Chip Carbon Nanotube Interconnects," 2014.

[50] K. R. Tunga, *Experimental and theoretical assessment of PBGA reliability in conjunction with field-use conditions*. 2004.

[51] E. Technology. (2012). *Tech Tip 19: Understanding Mechanical Properties of Epoxies for Modeling, Finite Element Analysis (FEA)*.

[52] X. Wang, Y. Mei, X. Li, M. Wang, Z. Cui, and G.-Q. Lu, "Pressureless sintering of nanosilver paste as die attachment on substrates with ENIG finish for semiconductor applications," *Journal of Alloys and Compounds*, vol. 777, pp. 578-585, 2019/03/10/ 2019.

[53] M. Knoerr and A. Schletz, "Power semiconductor joining through sintering of silver nanoparticles: Evaluation of influence of parameters time, temperature and pressure on density, strength and reliability," in *2010 6th International Conference on Integrated Power Electronics Systems*, 2010, pp. 1-6.

[54] J. N. Goldstein, Dale; Joy, David; Lyman, Charles; Echlin, Patrick; Lifshin, Eric; Sawyer, Linda; Michael, Joseph, *Scanning Electron Microscopy and X-Ray Microanalysis*, Third ed. New York: Kluwer Academic/Plenum Publishers, 2003.

[55] A. A. Barlian, W. T. Park, J. R. Mallon, A. J. Rastegar, and B. L. Pruitt, "Review: Semiconductor Piezoresistance for Microsystems," *Proceedings of the IEEE*, vol. 97, no. 3, pp. 513-552, 2009.

[56] T. T. Chiang *et al.*, "On-chip self-calibrated process-temperature sensor for TSV 3D integration," in *SOC Conference (SOCC), 2012 IEEE International*, 2012, pp. 370-375.

[57] D. S. Copeland *et al.*, "Reliability and die stress measurements in flip chip assemblies with carbon fiber core laminate substrates," in *Thermal and Thermomechanical Proceedings 10th Intersociety Conference on Phenomena in Electronics Systems, 2006. ITHERM 2006.*, 2006, pp. 997-1010.

[58] K. A. Ewuame *et al.*, "CMOS stress sensor for 3D integrated circuits: Thermo-mechanical effects of Through Silicon Via (TSV) on surrounding silicon," in *Thermal, mechanical and multi-physics simulation and experiments in microelectronics and microsystems (eurosime), 2014 15th international conference on*, 2014, pp. 1-8.

[59] S. Hussain, R. C. Jaeger, J. C. Suhling, J. C. Roberts, M. A. Motalab, and C. H. Cho, "Error analysis for piezoresistive stress sensors used in flip chip packaging," in *Thermal and Thermomechanical Phenomena in Electronic Systems (ITherm), 2010 12th IEEE Intersociety Conference on*, 2010, pp. 1-12.

[60] B. Vianne *et al.*, "Thermo-mechanical study of a 2.5D passive silicon interposer technology: Experimental, numerical and In-Situ stress sensors developments," in *3D Systems Integration Conference (3DIC), 2013 IEEE International*, 2013, pp. 1-7.

[61] C. J. Zhan *et al.*, "Assembly process and reliability assessment of TSV/RDL/IPD interposer with multi-chip-stacking for 3D IC integration SiP," in *2012 IEEE 62nd Electronic Components and Technology Conference*, 2012, pp. 548-554.

[62] D. J. Lichtenwalner, A. E. Hydrick, and A. I. Kingon, "Flexible thin film temperature and strain sensor array utilizing a novel sensing concept," *Sensors and Actuators A: Physical*, vol. 135, no. 2, pp. 593-597, 4/15/ 2007.

[63] J. Roberts *et al.*, "Measurement of die stress distributions in flip chip CBGA packaging," in *Thermal and Thermomechanical Phenomena in Electronic Systems (ITherm), 2010 12th IEEE Intersociety Conference on*, 2010, pp. 1-13.

[64] J. C. Suhling and R. C. Jaeger, "Silicon piezoresistive stress sensors and their application in electronic packaging," *IEEE Sensors Journal*, vol. 1, no. 1, pp. 14-30, 2001.

[65] Y. Zou, J. C. Suhling, R. W. Johnson, R. C. Jaeger, and A. K. M. Mian, "In-situ stress state measurements during chip-on-board assembly," *IEEE Transactions on Electronics Packaging Manufacturing*, vol. 22, no. 1, pp. 38-52, 1999.

[66] S.-H. Bae, Y. Lee, B. K. Sharma, H.-J. Lee, J.-H. Kim, and J.-H. Ahn, "Graphene-based transparent strain sensor," *Carbon*, vol. 51, pp. 236-242, 1// 2013.

[67] R. Kilaru *et al.*, "NiCr MEMS Tactile Sensors Embedded in Polyimide Toward Smart Skin," *Journal of Microelectromechanical Systems*, vol. 22, no. 2, pp. 349-355, 2013.

[68] X. Liu *et al.*, "Thermomechanical strain measurements by synchrotron x-ray diffraction and data interpretation for through-silicon vias," *Applied Physics Letters*, vol. 103, no. 2, p. 022107, 2013/07/08 2013.

[69] X. Liu *et al.*, "Dimension and liner dependent thermomechanical strain characterization of through-silicon vias using synchrotron x-ray diffraction," *Journal of Applied Physics*, vol. 114, no. 6, p. 064908, 2013/08/14 2013.

[70] T. Tian *et al.*, "On the Mechanical Stresses of Cu Through-Silicon Via (TSV) Samples Fabricated by SK Hynix vs. SEMATECH – Enabling Robust and Reliable 3-D Interconnect/Integrated Circuit (IC) Technology," *Procedia Engineering*, vol. 139, pp. 101-111, 2016/01/01 2016.

[71] K. Croes *et al.*, "Reliability concerns in copper TSV's: Methods and results," in *Physical and Failure Analysis of Integrated Circuits (IPFA), 2012 19th IEEE International Symposium on the*, 2012, pp. 1-5.

[72] I. De Wolf and E. Anastassakis, "Addendum: “Stress measurements in silicon devices through Raman spectroscopy: Bridging the gap between theory and experiment” [J. Appl. Phys. 79, 7148 (1996)]," *Journal of Applied Physics,* vol. 85, no. 10, pp. 7484-7485, 1999.

[73] I. De Wolf, H. E. Maes, and S. K. Jones, "Stress measurements in silicon devices through Raman spectroscopy: Bridging the gap between theory and experiment," *Journal of Applied Physics,* vol. 79, no. 9, pp. 7148-7156, 1996.

[74] W. Ingrid De, "Micro-Raman spectroscopy to study local mechanical stress in silicon integrated circuits," *Semiconductor Science and Technology,* vol. 11, no. 2, p. 139, 1996.

[75] C. Okoro *et al.*, "Extraction of the Appropriate Material Property for Realistic Modeling of Through-Silicon-Vias using μ-Raman Spectroscopy," in *2008 International Interconnect Technology Conference*, 2008, pp. 16-18.

[76] C. J. Wilson *et al.*, "Comparison of x-ray diffraction, wafer curvature and Raman spectroscopy to evaluate the stress evolution in Copper TSV's," in *2012 IEEE International Interconnect Technology Conference*, 2012, pp. 1-3.

[77] I. D. Wolf, V. Simons, V. Cherman, R. Labie, B. Vandevelde, and E. Beyne, "In-depth Raman spectroscopy analysis of various parameters affecting the mechanical stress near the surface and bulk of Cu-TSVs," in *2012 IEEE 62nd Electronic Components and Technology Conference*, 2012, pp. 331-337.

[78] R. G. R. Prasath, K. Skenes, and S. Danyluk, "Comparison of Phase Shifting Techniques for Measuring In-Plane Residual Stress in Thin, Flat Silicon Wafers," *Journal of Electronic Materials,* vol. 42, no. 8, pp. 2478-2485, 2013/08/01 2013.

[79] M. Ramji and R. G. R. Prasath, "Sensitivity of isoclinic data using various phase shifting techniques in digital photoelasticity towards generalized error sources," *Optics and Lasers in Engineering,* vol. 49, no. 9, pp. 1153-1167, 2011/09/01/ 2011.

[80] K. R. Madhu, R. G. R. Prasath, and K. Ramesh, "Colour Adaptation in Three Fringe Photoelasticity," *Experimental Mechanics,* vol. 47, no. 2, p. 271, 2007/01/23 2007.